JACOBS
UNIVERSITY

Investigation of ice formation and water mass modification in eastern Laptev Sea polynyas by means of satellites and models

by

Thomas Krumpen

A thesis submitted in fulfillment of the
requirements for the degree of

Doctor of Philosophy in Geosciences
School of Engineering and Science

Date of defense: October 4, 2010

Thesis Committee

Prof. Dr. Rüdiger Gerdes
Jacobs University Bremen

Prof. Dr. Laurenz Thomson
Jacobs University Bremen

Prof. Dr. Christian Haas
University of Alberta, Canada

Dr. Jens. A. Hölemann
Alfred Wegener Institute for Polar and Marine Research, Bremerhaven

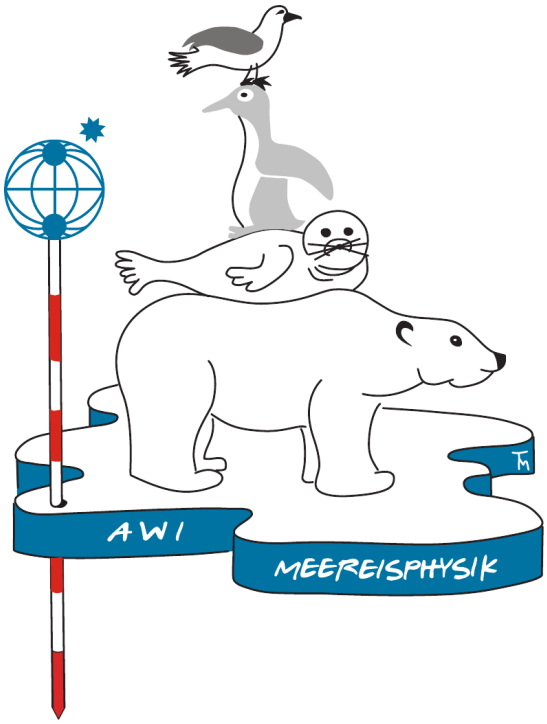
AWI
MEEREISPHYSIK

Abstract

Salt expelled during the formation of ice in polynyas leads to a downward precipitation of brine that causes thermohaline convection and erodes the density stratification of the water column. In this thesis we investigate by means of flux models and satellite data the ability of the Western New Siberian (WNS) flaw polynya to modify the stratification of the water column and to form saline bottom water. The accuracy of existent microwave satellite-based polynya monitoring methods is assessed by a comparison of derived estimates with airborne electromagnetic ice thickness measurements and aerial photographs taken across the polynya. The cross-validation indicates that in the narrow flaw polynyas of the Laptev Sea the coarse resolution of commonly used microwave channel combinations provokes errors through mixed signals at the fast and pack ice edges. Likewise, the accuracy of flux models is tested by comparing model results to ice thickness and ice production estimates derived from high-resolution thermal infrared satellite observations. We find that if a realistic fast ice boundary and parameterization of the collection depth H is used and if the movement of the pack ice edge is prescribed correctly, the model is an appropriate tool for studying polynya dynamics and estimating associated fluxes. Hence, a flux model is used to examine the effect of ice production on the stratification of the water column. The ability of the polynya to form dense shelf bottom water is investigated by adding the brine released during an exceptionally strong WNS polynya event in 2004 to the average winter density stratification of the water body. Owing to the strong density stratification and the apparent lack of extreme polynya events in the eastern Laptev Sea, we find the likelihood of convective mixing down to the bottom to be extremely low. We conclude that the recently observed breakdown of the stratification during polynya events is therefore predominantly related to wind- and tidally-driven turbulent mixing.

Contents

1

Introduction

1.1 The Arctic Ocean

The Arctic Ocean is divided into two basins, the Eurasian and the Canadian Basins, separated by a narrow ridge (Lomonosov Ridge) that crosses the whole Arctic straight from Siberia to Greenland. The marginal seas cover the shallow continental shelves surrounding the Arctic Ocean. Three connections to the worldwide ocean system exist, where water flows in and out of the basins (Fig. 1.1). The Fram Strait between Greenland and Scandinavia as the deepest and widest one. Much narrower, the Bering Strait between Alaska and Siberia allows the entry of Pacific Water into the Arctic Ocean. The third gateway for water masses consists of a system of narrow channels between the islands of the Canadian Archipelago. In terms of water mass exchange the Fram Strait is the most important one (Brandon and others, 2010).

The Arctic Ocean is usually described as consisting of three layers, characterized by different water masses: the Arctic Surface Water, the Atlantic Water, and the Deep Water.

The Arctic Surface Water is subdivided into the upper Polar Mixed layer (upper 30 - 50 m) and the Cold Halocline layer beneath (50 - 200 m, Barrie and others, 1998). The surface waters are influenced by freezing and melting of sea ice, precipitation and input of freshwater from the shelves and are consequently far less salty than the waters below (Brandon and others, 2010). The layer is characterized by two main circulation systems: the clockwise Beaufort Gyre extending over the entire Canadian Basin and the Transpolar Drift running lengthwise across the Eurasian Arctic from the Siberian Coast out through the western Fram Strait (Fig. 1.1)

The Cold Halocline layer is maintained by lateral transport of water from the shelves and is markedly stratified in density and salinity, while the temperature is at the freezing point (Melling and Lewis, 1982; Melling and Moore, 1995; Schlosser and others, 1994). Its stratifica-

tion prevents deepening of the Arctic Surface layer and insulates the much warmer (temperatures above 0°C) Atlantic layer below from surface processes. Any deepening of the mixed layer is without consequence for the sea ice, because the surface water remains at the freezing point.

The Atlantic Water enters the Arctic Ocean through the eastern side of Fram Strait (West Spitzbergen Current) and the Barents Sea. North of Fram Strait, the Atlantic Water encounters sea ice which is melted such that the Atlantic Water submerges below the fresh surface layer. Without further contact with the atmosphere, the Fram Strait Branch of the Atlantic Water follows the continental slope eastward at intermediate depth between 200 and 900 m (Barrie and others, 1998). On its path around the basin, diffusion and mixing processes with other water masses lead to a decrease of salinity and temperature. East of the St. Anna Trough, the Fram Strait Branch is joint by the Barents Sea Branch of the Atlantic Water, which is much colder due to intense cooling in the well-mixed Barents Sea. The Atlantic Water is transformed into cold and relatively saline Intermediate Water and cold and fresh Polar Water which exit the Arctic Ocean through the Fram Strait. The Arctic shelf seas are essential for the transformation of two separate water masses.

The cold and saline Arctic Deep Water is situated below the Atlantic Water. Both inflow and outflow of deep waters can only occur through the Fram Strait because of the shallow sill depths of the Bering Strait, the Canadian Archipelago, and the Barents Sea (Brandon and others, 2010). The deep Arctic Ocean is mainly renewed from the adjacent shelves (Aagaard and others, 1981) which results in a net conversion of surface to deeper water. Sea ice formation is an important process in the conversion.

1.2 Dynamics and importance of sea ice

Arctic sea ice plays a crucial role in Northern Hemisphere climate and ocean circulation (e.g. Serreze and others, 2009; Budikova, 2009). Sea ice in the Arctic Ocean forms when the surface temperature falls below the freezing point of sea water. The extent and thickness of the sea ice cover is governed by thermodynamic (e.g. heat content of ocean and air) and dynamic processes (e.g. windfields and ocean currents) in the ocean, atmosphere and the ice itself (Petrich and Eicken, 2010). Likewise, the influence of sea ice on ocean and atmosphere is manifold. For example, sea ice directly affects the vertical and/or horizontal redistribution of salt and is a driver of the global thermohaline circulation by providing cold and dense water during the freeze-up period and fresh water during the melt season (Barry and others, 1993; Zakharov,

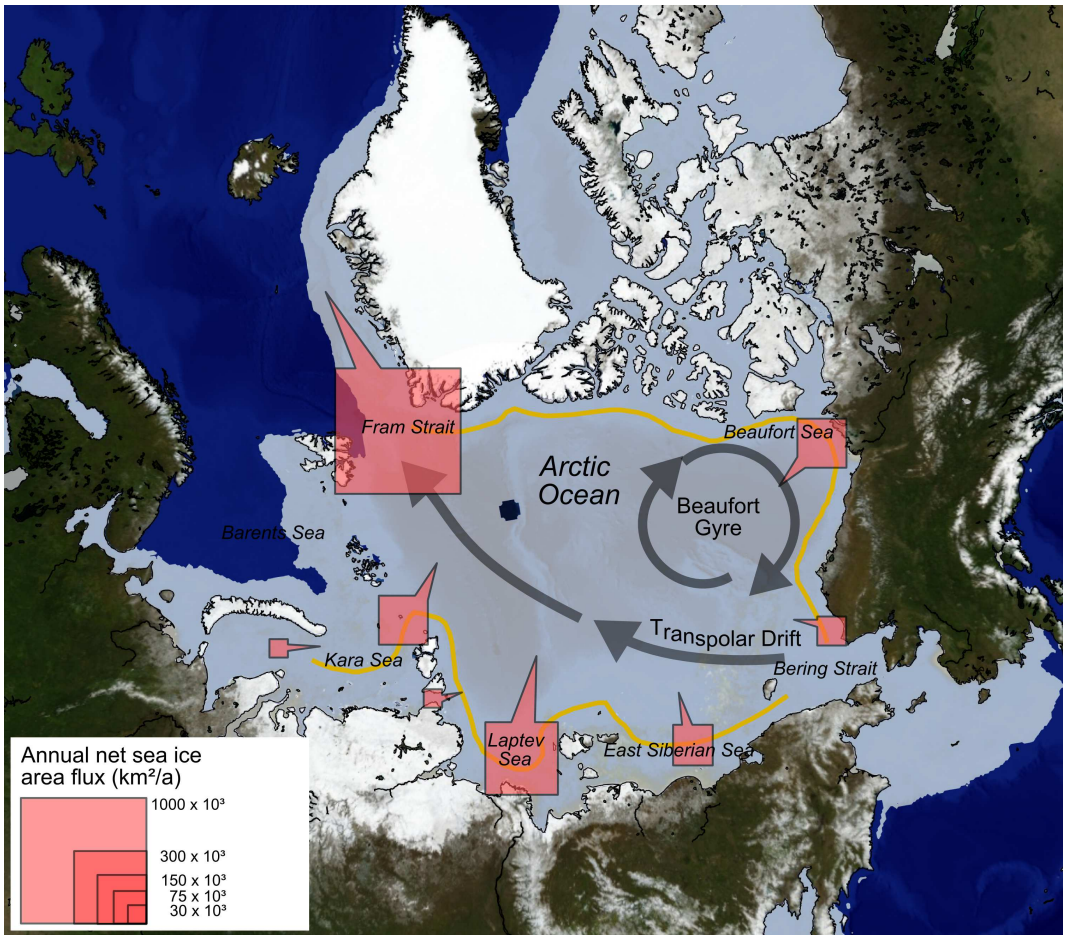

Figure 1.1: Main surface circulation pattern (arrows) in the Arctic Ocean and annual net sea ice flux in km^2 (boxes) of the Fram Strait and marginal seas (redrawn from Barrie and others (1998)). The sea ice extent (light blue shading) is equivalent to the sea ice situation as observed by passive microwave satellites in March, 2010. The yellow line represents the mean fast ice extent in winter (see section 1.3 and Buzov, 1991). Source of ice flux data: (Zakharov, 1976; Vinje, 1987; Aagaard and Carmack, 1989; Kvambekk and Vinje, 1993; Kotchetov and others, 1994; Alexandrov and others, 2000)).

1997; McBean and others, 2005). Moreover, sea ice reflects much of the solar radiation back into space, whereas dark ice free ocean absorbs more of the solar energy. Hence, the presence of an insulating ice layer prevents the ocean from heating by limiting the flow of heat between ocean and atmosphere. This results in a positive feedback loop called ice albedo feedback, which causes the loss of the sea ice to be self-compounding.

The long-term average extent of sea ice in the Arctic Ocean varies seasonally from 15.5×10^6 km^2 in March to 7.5×10^6 km^2 in September (Comiso, 2003). The motion patterns of ice and surface water are about the same, as a long-term average, and largely wind-driven (Wadhams, 2000). The Beaufort Gyre primarily recirculates ice formed in the Beaufort, Chukchi, and East Siberian Seas and is responsible for the formation of thicker and older perennial sea ice zones

north of Greenland and north of the Canadian Islands. Depending on the dominant atmospheric circulation over a year the Beaufort Gyre can be expanded or limited to a small region. The Transpolar Drift acts as a gigantic conveyor belt by transporting ice from the Kara, Laptev, and East Siberian seas, toward the Fram Strait, where it exits the central Arctic Basin (Colony and Thorndike, 1985). Following Vinje (2001) and Koeberle and Gerdes (2003), between 600 - 1200 $\times$ 10^3 km^2 of the polar pack ice is exported annually from the Arctic Basin to the North Atlantic. This is equivalent to an volume flux of 2.0 - 4.2 $\times$ 10^3 km^3 per year. The approximate annual net sea ice area flux out of Fram Strait and the marginal seas of the Arctic Ocean is shown in Figure (1.1).

At longer time scales, the variability in the sea ice drift pattern is mainly controlled by changes in the large-scale atmospheric circulation. The Arctic atmosphere alternates between two regimes of a weakened or strengthened anticyclonic circulation (Beaufort Gyre) and an intensified or suppressed cyclonic circulation in the eastern Arctic (Bareiss and Goergen, 2005). The changes between the atmospheric circulation regimes can be described by the Arctic Oscillation (AO) index, which is defined as the leading principal component of Northern Hemisphere sea level pressure (SLP, Zhao and Liu, 2007). The AO governs the decadal and multidecadal variability of the atmospheric and oceanic circulation in the Arctic (Bareiss and Goergen, 2005). In this context, Proshutinsky and Johnson (1997) define the two arctic-wide observed wind-driven oceanic circulation patterns as the anticyclonic and cyclonic circulation regime, each of which is persisting from 5 to 7 years.

In recent years, the summer Arctic sea ice extent and thickness have undergone dramatic changes. The sea ice extent has been declining at an annual average rate of approximately 3 % per decade over the satellite record, and the summer decline seems to be accelerating (Comiso, 2010; Kwok and others, 2009; Kwok and Rothrock, 2009). In September 2007, an unusually low summer ice extent of 4.2 $\times$ 10^6 km^2 was revealed by satellite observation, which was 1.6 $\times$ 10^6 km^2 or 23 % less than the previous record set in September 2005 (Stroeve and others, 2008).

Climate models agree that the sea ice extent will further decline through the 21st century in response to atmospheric greenhouse gas loading (Zhang and Walsh, 2006). The rapid reduction in Arctic summer ice extent is thought to be a consequence of anomalously high surface air temperatures (Stroeve and others, 2005). Meier and others (2007) suggest that both the AO-induced circulation changes and increased temperatures have contributed to the decline. An increased advection of thick multi-year ice out of the Arctic through Fram Strait, replaced by thinner ice, might further precondition for rapid sea ice retreat in summer (Rigor and Wallace,

2004).

So far, feedback mechanisms, and the consequences of a significantly reduced summer ice cover, on the climate of the Northern Hemisphere are still speculative. Nevertheless, the trend in sea ice decline, the lack of winter recovery (Kwok and Rothrock, 2009), early onsets of spring melting, and warmer-than-average temperatures suggest a system that is trapped in a loop of positive feedbacks, in which responses to inputs into the system cause it to shift even further away from normal (Scott, 2008).

1.3 The Laptev Sea

Among the marginal seas of the Arctic Ocean the Laptev Sea is considered as one of the most significant regions of net ice production and export (Fig. 1.1, Zakharov, 1966; Dethleff and others, 1998) giving it a key role in the future fate of the Arctic sea ice and the ocean water mass distribution and larger scale circulation. Following Rigor and Colony (1997) as much as 20 % of the ice transported through the Fram Strait is produced in the Laptev Sea, which is located between the coast of Siberia, Severnaya Zemlya and the New Siberian Islands (Fig. 1.2). It is a very shallow shelf sea with water depths between 15 and 200 m (Timokhov, 1994) and comprises an area of approximately 500×10^3 km^2 (Dmitrenko and others, 2009). 5 major river systems (Khatanga, Anabar, Olenek, Lena and Yana river) drain into the Laptev Sea, the Lena River being the biggest one (Fig. 1.2). The Laptev Sea is ice covered from October to June, while during summer most of the sea becomes ice free. The sea ice cover of the Laptev Sea can be divided into three regimes: the fast ice, the pack ice, and flaw polynyas (Eicken and others, 2005).

The fast ice consists of bottomfast and landfast ice. Bottomfast ice is sea ice that has frozen to the sea floor over shallow parts of less than 2 m water depth. It extends 10 - 30 km offshore the coast and is important maintaining the submarine permafrost in near-shore areas (Reimnitz and others, 1995; Eicken and others, 2005).

The floating landfast ice is sea ice that has fastened along coasts. It covers more than 50 % of the shallow eastern Laptev Sea and up to 25 % of the western Laptev Sea. The mean fast ice thickness is around 2 m (Kotchetov and others, 1994). The lateral extent of the landfast ice roughly coincides with the position of the 20 m to 25 m isobaths and is controlled by the presence of small islands and shoals (Reimnitz and others, 1994). According to Dmitrenko and others (1999), small scale changes in the extent of the fast ice edge are related to the interannunal variability in the entrainment of river discharge onto the shelf from the Khatanga, Anabar, Olenek, Lena and Yana rivers. Figure (1.2) shows the mean position of the fast ice edge at the end of

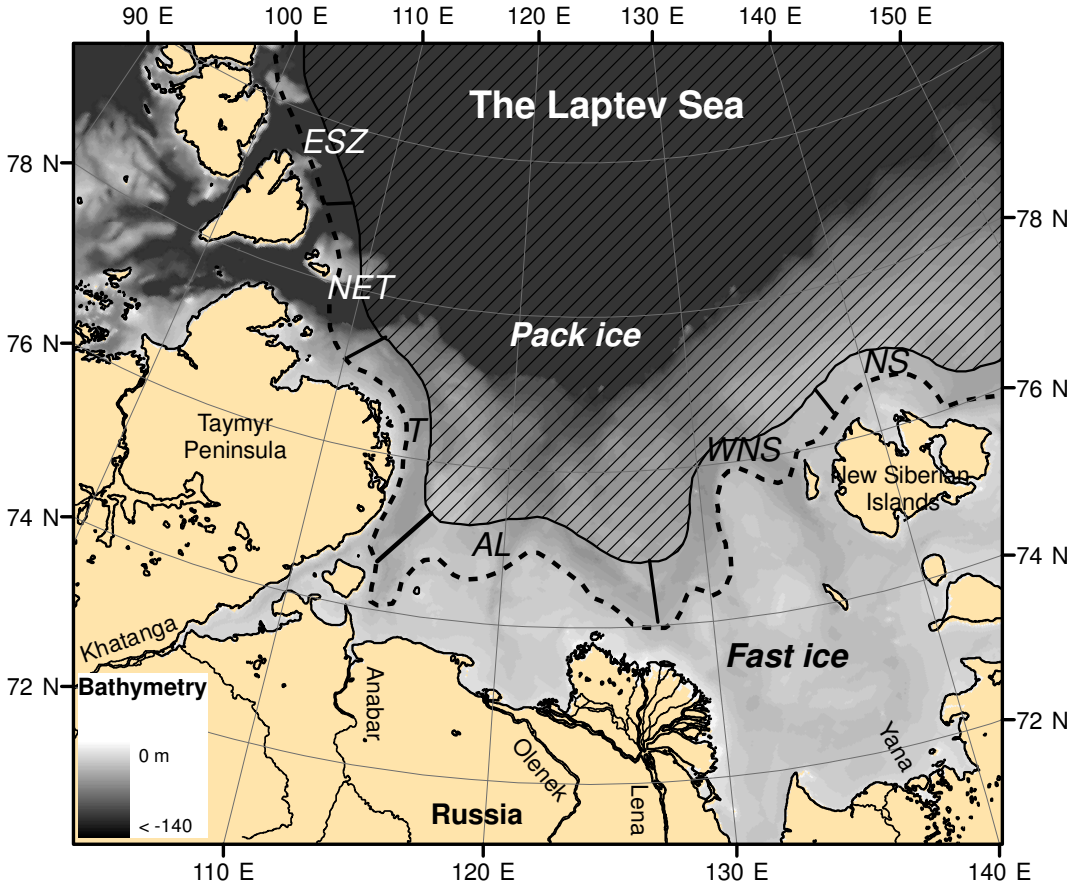

Figure 1.2: Map of the Laptev Sea showing the three distinct sea ice components: the fast ice zone, the pack ice zone, and the location of the flaw polynyas. The mean lateral extent of the fast ice at the end of the winter is indicated by the black dashed line. The grey shaded area north of the fast ice represents the pack ice zone. Between pack ice and fast ice edge, flaw polynyas are formed. The New Siberian polynya (NS), the Western New Siberian polynya (WNS), the Anabar-Lena polynya (AL), the Taymyr polynya, the North-Eastern Taymyr polynya (NET) and the Eastern Severnaya Zemlya (ESZ) polynya. Color coding corresponds to the bathymetry (water depth in m, source: Smith and Sandwell, 1997).

the winter, as derived by Bareiss and Goergen (2005) from Advanced Very High Resolution Radiometer (AVHRR) satellite images.

The freely floating ice pack offshore the fast ice edge consists mostly of ice formed during the freeze up in autumn. According to systematic observations carried out by the Soviet Union since the 1930s, pack ice in the Laptev Sea grows up to a mean thickness of 1.57 m ± 0.25 m (Romanov, 1996). The pack ice drift in the Laptev Sea during autumn, winter and spring is dominated by persistent offshore winds pushing the pack ice away from the fast ice edge (Timokhov, 1994; Rigor and Colony, 1997). Satellite based estimates made by Alexandrov and others (2000) have shown that the annual areal ice exchange with the Arctic Ocean through the northern and

northeastern boundaries of the Laptev Sea amounts to roughly 300 × 10^3 km^2 y^{-1} (Fig. 1.1). Following Proshutinsky and Johnson (1997) an increased advection away from the coast can be observed during years with an anticyclonic circulation regime. In contrast, during years of cyclonic atmospheric circulation, the average winter pack ice export is lower.

As the pack ice drifts away from the fast ice edge, polynyas are formed. Open water with a temperature close to the freezing point of sea water is exposed to the cold polar air and heat loss from the open ocean to the atmosphere results in the formation of frazil ice in the water column that is transported by wind and currents towards the downwind pack ice edge. The frazil ice arriving at the downwind edge forms a thin layer of ice and water slurry called grease ice that thickens by thermodynamic and dynamic processes as it drifts further offshore (Smith and others, 1990; Winsor and Bjoerk, 2000; Willmott and others, 2007). If the polynya is limited on one side by landfast ice it is referred to as a flaw polynya and if the coast defines its onshore extent, it is called coastal polynya. According to its geophysical mechanism and shallow bottom topography, the recurrent flaw polynyas in the Laptev Sea are classified as shelf water latent heat polynyas. Different to latent heat polynyas, sensible heat polynyas are thermally driven. They appear as a result of oceanic sensible heat entering the area of polynya formation in amounts large enough to melt any preexisting ice and prevent the growth of new ice (Morales Maqueda and others, 2004). The physical processes taking place inside a latent heat flaw polynya are illustrated in Figure 1.3.

The waters on the shelves have a tendency towards a two-layered structure (Aagaard and others, 1985) due to sea ice melt in summer, large freshwater inputs from rivers and precipitation. However, when ice is formed in polynyas, salt is expelled, leading to a downward precipitation of brine that causes thermoholine convection and temporarily erodes the density stratification of the water column (Ivanov and Golovin, 2007). Other processes that contribute to a destratification of the water body in areas of open water are turbulent mixing processes induced by currents and winds. In polynyas, where ice production is exceptionally strong compared to its areal size, the thermohaline convection together with wind- and current-induced mixing processes may indeed lead to total water homogenization, in which case dense bottom water is formed (Backhaus and others, 1997). These cold saline waters may be transported by large-scale currents downslope and have considerable impact far away from their source. For instance, the Cold Halocline is maintained by advection of cold saline water formed as a result of sea ice growth over the continental shelves of the Arctic Ocean and the Bering Sea (Aagaard and others, 1981; Cavalieri and Martin, 1994; Winsor and Bjoerk, 2000). Moreover, polynyas are important for a number of other environmental processes: If mixing cells are deep enough, nutrients are

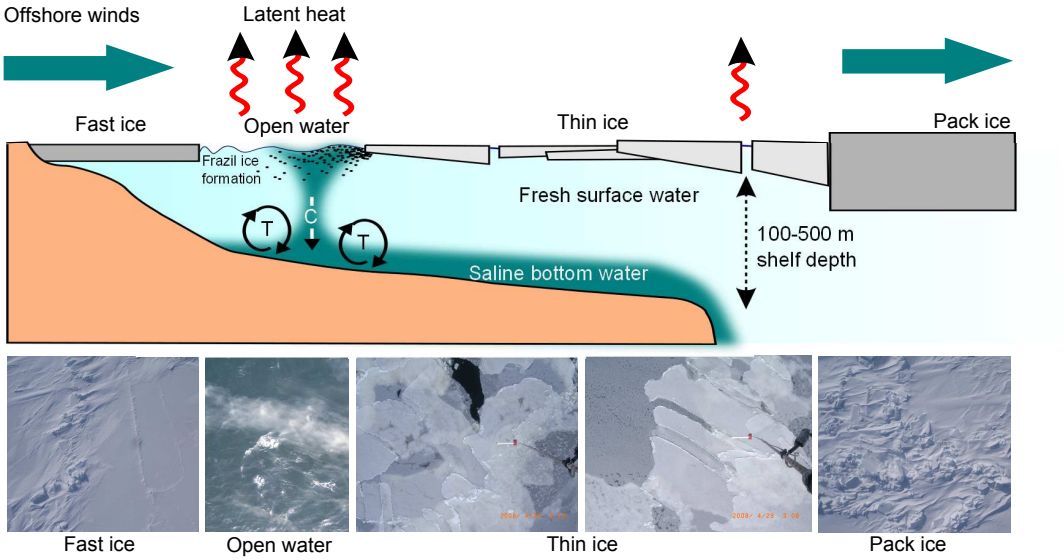

Figure 1.3: The upper panel shows a schematic drawing of physical processes taking place inside wind-driven latent heat flaw polynyas. Offshore winds push the pack ice away from the fast ice edge, exposing the freezing surface waters to the cold atmosphere. Frazil ice is formed and herded downwind until it consolidates at the pack ice edge. When drifting further offshore, the consolidated thin ice is growing by thermodynamic and dynamic processes. During ice formation, brine is released and added to the water body. If ice formation is strong enough, thermohaline convection (C) together with wind- and current-induced mixing processes (T) may indeed erode the stratification and lead to a total water homogenization, in which case dense bottom water is formed. The saline bottom water accumulates over the shelf and eventually flows down the shelf break slope to form deep water. The aerial photographs in the lower panel were taken during the TRANSDRIFT XIII campaign and show the fast ice and pack ice zone and open water (with frazil ice formation) and thin ice areas inside an active polynya.

circulated from the water bottom to the upper surface layer strengthening biological productivity (Barrie and others, 1998; Arrigo, 2005). In addition, polynyas act as a sink for contaminants and are sites of strong ocean-to-atmosphere moisture and heat losses, which lead to a rapid warming of the air column above and downwind of the polynya and therefore to modifications in the mesoscale atmospheric motions (Smith and others, 1990; Alam and Curry, 1995; Sharma, 2003; Morales Maqueda and others, 2004).

In the Laptev Sea, persistent offshore winds generate a quasi-perennial flaw polynya extending almost 2000 km along the shelf and landfast sea ice several hundreds of kilometres wide (Morales Maqueda and others, 2004). Following Zakharov (1966), the prominent flaw polynyas in the Laptev Sea are the New Siberian polynya (NS), the Western New Siberian polynya (WNS), the Anabar-Lena polynya (AL), the Taymyr polynya, the North-Eastern Taymyr polynya (NET) and the Eastern Severnaya Zemlya polynya (ESZ, compare Fig. 1.2).

According to calculations made by Aagaard and others (1985) and Dmitrenko and others (2009),

the annual net sea ice production in the entire Laptev Sea amounts to roughly 900 km^3.

Following Dethleff and others (1998), who investigated ice formation in Laptev Sea polynyas by means of a model applied to calculate ocean-to-atmosphere heat flux and the resulting new ice formation over open water, as much as 258 km^3 of ice is produced in polynyas. Putting the results of Dethleff and others (1998) in relation to the annual ice production estimated by Dmitrenko and others (2009), flaw polynyas produce about 26 % of the annual Laptev Sea ice. The average annual polynya ice production calculated by Winsor and Bjoerk (2000) is far lower. The authors investigated Arctic polynyas during 39 winter seasons from 1958 to 1997 by means of a large scale polynya model and calculated an average annual ice production of 43 km^3 (4.3 % of the annual ice production). Findings made by Willmes and others (2010a) are somewhat similar to what is suggested by Winsor and Bjoerk (2000). According to their satellite-based estimates, the annual polynya ice production amounts to only 5.5 % (55 km^3) for the total seasonal ice production and is hence significantly smaller than approximations made by Dethleff and others (1998).

Large discrepancies exist in the estimated contribution of Laptev Sea polynyas to the annual net sea ice formation. This might be a consequence of the use of different sensor systems, models, observation periods and alternating definitions for the term 'active polynya'. Nevertheless, without an exact quantification of ice formation rates, an approximation of polynya induced formation of saline water is difficult.

Following Schauer and others (1997) and Lenn and others (2008), potential sites for dense water formation are located in the central and northwestern Laptev Sea where ice production is comparatively high. Dense water formed in these polynyas is believed to feed the Cold Halocline but is found to be insufficiently dense to ventilate the layers below.

Compared to the central and northwestern polynyas, the Western New Siberian polynya (WNS; Fig. 1.2) located in the eastern Laptev Sea is a region of relatively weak to moderate ice formation rates (Willmes and others, 2010b). In addition, the large summer run-off of the Lena river freshens the surface ocean layer and leads to the development of a distinct vertical density gradient in the water column (Dmitrenko and others, 2005). The strength of the stratification is controlled by the atmospheric circulation during summer months. Anticyclonic wind conditions force the riverine water northwards and result in a stronger density stratification. Cyclonic atmospheric circulation deflects the freshwater plume of the River Lena eastward towards the East Siberian Sea, thus causing higher salinities and a weaker density stratification in the eastern Laptev Sea and the area around the WNS polynya (Hoelemann and others, 2010).

Following Dmitrenko and others (2005), who evaluated ice production in the Laptev Sea based on a hydrographical dataset, this strong vertical density gradient limits the probability for the occurrence of convection down to the sea floor during a polynya event in the eastern Laptev Sea to 20 %.

1.4 Scope of this work

Since ice production and salt formation in the Laptev Sea have received comparatively little attention, and existing studies show large discrepancies in ice and salt flux estimates, little is known about the role of the Laptev Sea polynyas for shelf water mass modification. However, understanding vertical mixing and convection processes in coastal polynyas is important, since they affect momentum, heat and biogeochemical air-sea fluxes (Morales Maqueda and others, 2004), and provide conditions for downslope transport of water, sediments and pollutants. (Reimnitz and others, 1994; Sherwood, 2000; Smedsrud, 2004).

In recognition of its importance and its barely explored state, the Laptev Sea in general and the eastern Laptev Sea in particular has been subject of several Russian-German research projects. In the framework of this cooperation, the Arctic and Antarctic Research Institute (AARI) in St. Petersburg, the Alfred Wegener Institute (AWI) in Bremerhaven, the Leibniz Institute of Marine Sciences (IFM-Geomar) in Kiel, the University of Trier, the Academy for Science and Literature in Mainz and the Lena Delta Reserve in Tiksi, focus on year-round, integrated system studies of sea ice cover, water column and sea floor across and along frontal zones and the Laptev Sea flaw polynyas during two seasonal cycles (2007 - 2009, System Laptev Sea, 2008). The objective of the project is to investigate the response of frontal zones and the polynya system in the Laptev Sea to a changing Arctic environment (e.g. Dmitrenko and others, 2010a,b; Hoelemann and others, 2010; Krumpen and others, 2010b; Willmes and others, 2010b). The presented thesis is part of the Russian-German research cooperation 'Laptev Sea System'.

Because of its accessibility, a focus of the study is put on the WNS polynya in the eastern Laptev Sea. The polynya is located less than 300 km away from Tiksi, a Russian settlement at the coast of the Lena Delta. To aid scientific investigations, oceanographic, physical and biogeochemical processes in the WNS polynya were studied in the field by means of 3 ship-based summer expeditions and 2 helicopter-based winter expeditions (TRANSDRIFT (TD) XII, September 2007; TD XIII, April 2008; TD XIV, September 2008; TD XV, March 2008 and TD XVI, September 2009). The aim of the ship-based expeditions was to deploy 4 oceanographic year-round moorings on the Laptev Sea shelf in the vicinity of the WNS polynya. During the winter expeditions, WNS

Figure 1.4: Scientific activities during TD XIII expedition. The upper left panel shows the assembling of a weather station. The lower left panel pictures the recovery of a mooring deployed for 1 month under the fast ice by means of a tripod. The right figure shows the so called EM-Bird, an airborne electromagnetic (EM) system towed by a Russian MI-8 helicopter 15 meters above the ice surface. The instrument utilises the contrast of electrical conductivity between sea water and sea ice to determine the distance to the ice-water interface (ice thickness).

polynya dynamics and ice formation were monitored with the aid of helicopter-borne surveys such as electromagnetic (HEM) ice thickness measurements and aerial photographs. In addition, a series of moorings and weather stations was installed along the fast ice edge to record hydrographic and atmospheric processes. Figure 1.4 shows scientific activities during TD XIII.

At present, it is unclear whether ice formation in the WNS polynya is high enough to induce vertical mixing processes that penetrate down to the seafloor. Nevertheless, owing to the strength of the stratification and the noticeable lack of extreme polynya events (Winsor and Bjoerk, 2000), we hypothesize that ice production alone in the WNS polynya is not high enough to erode the halocline and that the probability for dense water formation is far lower than estimated by Dmitrenko and others (2005). Hence, we believe vertical mixing processes to be predominantly related to wind-driven or current-driven turbulent processes.

To test the hypothesis, an appropriate method to investigate polynya dynamics and subsequent

fluxes on a small-scale basis is required. We therefore first compare and evaluate different established satellite or model-based approaches. The method of choice is then used to estimate ice production and salt rejection taking place during strong polynya opening events and to examine the effect on the stratification of the water body beneath.

1.5 Structure of the thesis

In this thesis we investigate the ability of the WNS polynya to modify the stratification of the water column and to form higher saline water. Owing to the strong stratification and moderate ice formation rates, we believe the probability for dense shelf bottom water formation to be far lower than estimated by Dmitrenko and others (2005). The most appropriate approach for an estimation of ice production and salt rejection in this area is determined through a comparison of different satellite-based methods and models.

In the first paper

Willmes, S., T. Krumpen, S. Adams, L. Rabenstein, C. Haas, J. Hoelemann, S. Hendricks and Heinemann G., 2010b. Cross-Validation of polynya monitoring methods from multi-sensor satellite and airborne data: A case study from the Laptev Sea, *Canadian Journal of Remote Sensing*, **36**(1), in press

we test spatial and temporal transferability of established satellite-based polynya monitoring methods to the Laptev Sea region. First we provide an overview of the feasibility and comparability of the existing methods in describing distinct polynya features, in particular polynya area and thin ice thickness. Second, we cross-validate satellite-derived polynya characteristics and compare approaches to high-resolution helicopter-borne ice thickness measurements and aerial photography acquired during the TD XIII expedition in winter 2008. Finally, we will evaluate the presented methods with respect to their applicability for long-term investigations of the Laptev Sea polynya dynamics and the inter-annual variability of ice production.

Because we find existing passive microwave satellite-based polynya monitoring methods to suffer from coarse resolution and errors in the ice thickness retrieval, monitoring of ice production in narrow leads and polynyas remains difficult with satellites alone. This gap may be filled by flux models capable of simulating polynya evolution and ice fluxes. Questions still remain as to the consistency and accuracy of flux model assessments.

The aim of the second paper

Krumpen, T., S. Willmes, M. A. Morales Maqueda, R. Gerdes, C. Haas, J.. Hoelemann and D. Schroeder, 2010c. Verification of a polynya flux model by means of thermal infrared satellite observations, *Annals of Glaciology*, in press

is therefore to test whether flux models provide realistic ice production estimates and can be used to fill the gap in narrow lead and polynya ice production monitoring. Hence, we apply a two-dimensional flux model developed by Morales Maqueda and Willmott (2000) to simulate ice production of an 11 day polynya event that took place in the southern Laptev Sea in late December, 2007. Model results are compared to ice thickness and ice production estimates, calculated using high-resolution thermal infrared satellite data obtained from the Moderate Resolution Imaging Sensor (MODIS) in conjunction with an atmospheric dataset (Riggs and others, 2003; Yu and Lindsay, 2003).

In the third paper

Krumpen, T., C. Haas, S. Hendricks, J. Hoelemann, R. Gerdes and D. Kalmbach, 2010a. HELIOS, a nadir-looking sea ice monitoring camera, submitted to *Cold Region Science and Technology*

we describe the development of a simple nadir-looking low-cost photogrammetric system that is used to obtain aerial photographs over sea ice: The HELicopter-borne Ice Observation System (HELIOS). The system was applied in this thesis (Krumpen and others, 2010c,b) and in a number of other studies (e.g. Busche and others, 2009; Dmitrenko and others, 2010b) to obtain information about polynya characteristics and to document other airborne observations. Our objective is to test whether the system fulfills requirements on accuracy for the documentation of ground- and airborne surveys of sea ice. We present the aerial unit, the image processing techniques and evaluate, based on data obtained during former expeditions, the precision of the system.

The hypothesis of the thesis is tested in the fourth paper

Krumpen, T., J. A. Hoelemann, S. Willmes, M. A. Morales Maqueda, T. Busche, I. A. Dmitrenko, R. Gerdes, C. Haas, G. Heinemann, S. Hendricks, S. Kirillov, L. Rabenstein and D. Schroeder, 2010b. Sea ice production and water mass modification in the eastern Laptev Sea, submitted to *Journal of Geophysical Research*

by applying a flux model to an exceptionally strong and consistent polynya event in 2004. In paper 2 we find that this simplified physical polynya model provides a good and fairly accurate alternative to passive microwave polynya monitoring techniques. The ability of the polynya

to form dense shelf bottom water is judged by integrating the computed amount of salt rejection over a water body with a relatively weak vertical density gradient, pre-conditioned by a cyclonic circulation during summer. The underlying hydrographic data were taken from the data archive of the AARI and former Russian-German expeditions. Prior to the simulation of the major polynya opening event observed in 2004, we test the model parameterizations and performance using a minor but well documented opening event observed during TD XIII.

2

Paper 1: Cross-Validation of polynya monitoring methods from multi-sensor satellite and airborne data: A case study for the Laptev Sea

Publication, *Canadian Journal of Remote Sensing*, 2010, **36**(1), in press

Sascha Willmes[1], Thomas Krumpen[2], Susanne Adams[1], Lasse Rabenstein[3], Christian Haas[4], Jens A. Hölemann[5], Stefan Hendricks[2], and Günther Heinemann[1]

[1]University of Trier, Dept. of Environmental Meteorology, Behringstr. 21, D-54286 Trier, Germany
[2]Alfred Wegener Institute, Dept. of Sea Ice Physics, Busse Str. 24, 27570 Bremerhaven, Germany
[3]Institute of Geophysics, ETH Zurich, Sonneggstr. 5, Switzerland
[4]University of Alberta, Dept. of Earth & Atmospheric Sciences, Edmonton, Alberta, Canada
[5]Alfred Wegener Institute, Dept. of Observational Oceanography, Am Handelshafen 12, 27570 Bremerhaven, Germany

Abstract

Wind-driven flaw polynyas in the polar oceans are recognized as regions of extensive new ice formation in the cold season. Hence, they may play an increasing role in the uncertain future of the sea ice budget in the polar oceans. The Laptev Sea polynyas in the Siberian Arctic are well recognized as significant ice producers and might gain special attention with regards to ice volume changes in the Arctic. A long-term monitoring and characterization of these polynyas requires stable methods to detect the area of open water as well as growth, thickness and evolution of thin ice. We examine different parameters and methods to observe polynya area and thin ice thickness during a prominent polynya event in the Laptev Sea in April 2008. These are derived from visible, infrared and microwave satellite data. Airborne electromagnetic ice thickness measurements with high spatial resolution and aerial photography taken across the polynya are used to assess the feasibility of the used methods for long-term and large-scale polynya monitoring within this area. Our results indicate that in the narrow flaw polynyas of the Laptev Sea the coarse resolution of commonly used microwave channel combinations provokes sources of error through mixed signals at the fast and pack ice edges. Polynya monitoring results can be significantly improved using enhanced resolution data products. This implies that previously suggested methods for the retrieval of polynya area, thin ice thickness and ice production are not transferable in space and time. Data as well as method parameterizations have to be chosen carefully to avoid large errors due to regional peculiarities.

2.1 Introduction

The Arctic Ocean has been subject to significant changes in summer and fall sea ice extent during the last two decades, in particulary during the last 5 years (Serreze and others, 2007; Stroeve and others, 2007). In addition to the apparent decrease in ice extent, recent studies provide evidence for a remarkable thinning of Arctic sea ice (e.g. Kwok and others, 2009). This has the potential to trigger an even accelerated depletion of summer sea ice in the near future which will affect the global climate system as well as the global ocean circulation (Zakharov, 1997). From this perspective, an accurate monitoring and quantification of ice production during winter is crucial for an assessment of the Arctic sea ice state.

Flaw (wind-driven) polynyas are nonlinear-shaped regions of open water and thin ice within a closed ice cover, formed by offshore winds advecting the pack ice away from the fast ice edge (Smith and others, 1990). Most of these polynyas are recurring and represent dynamic regions with large amounts of new ice forming during winter. Heat loss across the water-air interface results in strong ice production and salt rejection (Morales Maqueda and others, 2004) and the newly formed ice is incorporated into the main drift systems of the Arctic Ocean. A satellite-based operational estimation of ice formation within a polynya is preceded by mainly two monitoring challenges. First, open water/thin ice area, hereinafter referred to as polynya area (POLA), has to be derived with high accuracy and second, thin ice thickness (hi) distribution within the polynya needs to be determined. Afterwards surface heat loss and ice formation can be calculated with the aid of meteorological data. Sea ice concentrations as derived from the Scanning Multichannel Microwave Radiometer (SMMR) and Special Sensor Microwave/Imager (SSM/I) satellite sensors can be used to estimate POLA (Martin and Cavalieri, 1989; Massom and others, 1998; Bareiss and Goergen, 2005) within pre-defined boxes. This comes at the cost of a low spatial resolution (25×25 km^2) and hence, the neglect of subpixel-scale flaw leads. As shown by Kwok and others (2007), one has to take into account that large areas of thin ice are capable of influencing sea ice concentration retrievals such that the real sea ice area is underestimated. Alternatively, Markus and Burns (1995) suggested a Polynya Signature Simulation Method (PSSM) that iteratively classifies open water and thin ice at a higher spatial resolution of up to 5×5 km^2 from microwave brightness temperatures. The PSSM was previously used with slightly changing parameterizations in different studies (Kern and others, 2005; Arrigo and van Dijken, 2004; Renfrew and others, 2002). Kern (2009) showed that the PSSM can be used to observe the spatiotemporal variability of polynya dynamics. The method provides the three surface classes open water, thin ice and thick ice. A comparison with ice thickness

derived from thermal infrared data revealed that the PSSM thin ice class includes hi values of up to 0.25 m (Kern and others, 2007).

A method to infer hi from microwave data was suggested by Martin and others (2005, 2007) and recently reinforced by Tamura and others (2007, 2008) and Naoki and others (2008). Martin and others (2005) found the polarization ratios from microwave sensor data to correlate with high-resolution (~ 1 km^2) hi data calculated from surface temperatures as measured in the thermal infrared (Advanced Very High Resolution Radiometer (AVHRR) and Moderate-Resolution Imaging Spectroradiometer (MODIS) sensors) (Yu and Lindsay, 2003). The high-resolution hi retrieval is also referred to as thermal ice thickness (hi_{TH}) and restricted to clear-sky conditions. However, it provides a reasonable estimate of thicknesses for sea ice up to 0.5 m. A comprehensive comparison of SAR data with SSM/I sea ice concentrations, PSSM, and numerical modelling used to delineate the distribution of open water and thin ice as well as size and shape of the polynya, is given in Dokken and others (2002).

Here, we apply the polynya monitoring methods mentioned previously to a well documented polynya event in the Laptev Sea. Our goal is to test the spatial and temporal transferability of established methods to the Laptev Sea region, which is special in terms of a) strong local ice formation directly feeding the Transpolar Drift and b) very low salinities due to high input of freshwater from the Lena River. The first point makes a monitoring of ice production within Laptev Sea polynyas crucial for an assessment of the Arctic sea ice budget. The second point allows for a test of the applicability of monitoring methods to a region with an expected difference in surface microwave response compared to other polynya areas.

First we provide an overview of the feasibility and comparability of the existing methods in describing distinct polynya features, in particular POLA and hi. Second, we will cross-validate satellite-derived polynya characteristics and use high-resolution helicopter-borne ice thickness measurements and aerial photography acquired during an International Polar Year (IPY) campaign to assess previously suggested approaches for the classification of POLA and hi from satellite data.

Lastly, we evaluate the presented methods with respect to their applicability for long-term investigations of the Laptev Sea polynya dynamics and the inter-annual variability of ice production as well as their capabilities for model evaluation and calibration.

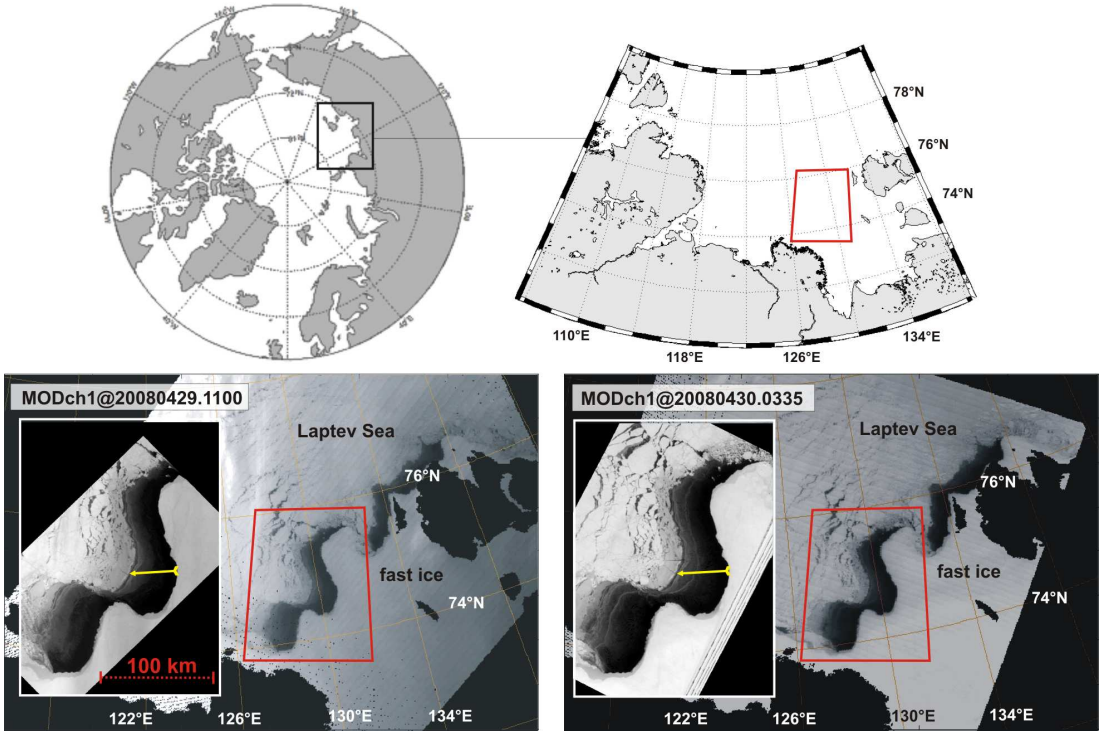

Figure 2.1: Map of the Arctic showing the location and subset of the Laptev Sea (upper panels) and MODIS(Aqua), channel 1 images for the Laptev Sea area (1 × 1 km^2 resolution, large figures) with enhanced subset (250 × 250 m^2 resolution) of the Western New Siberian polynya for April 29, 2008 at 11.00 UTC (lower left panel) and April 30, 2008 at 03.35 UTC (lower right panel). The HEM flight track from April 30 at 02.25 UTC is indicated by a yellow line.

2.2 Data and methods

This study focuses on a polynya event in the south-eastern Laptev Sea on April 29 - 30, 2008 (Fig. 2.1). The event was chosen because clear-sky conditions allowed for the use of visible/infrared satellite data while coincident Synthetic Aperture Radar (SAR) data, electromagnetic ice thickness measurements from helicopter (Helicopter Electro-Magnetic, HEM) and aerial photography are available. On April 29 - 30 the recurring Western New Siberian polynya, an eastern branch of the Laptev Sea flaw polynya (Barber and Massom, 2007; Bareiss and Goergen, 2005), was widely open and revealed mixed and partially rafted ice types as well as open water. Airborne data and ice thickness profiles from HEM measurements presented here were acquired during the TRANSDRIFT XIII expedition in April 2008. This field campaign was part of an series of land- and ship-based expeditions to the Laptev Sea within the IPY-assigned joint German-Russian project 'Laptev Sea system'.

All data were projected onto a common polar-stereographic grid centred over the observed polynya. The spatial resolution of the grid in each case was adjusted to the native resolution

of the projected data. Another consideration in the selection of imagery was that the time window of acquisitions is sufficiently small to minimize bias from ice advection and ice growth that takes places in between the records (see Table 2.1, Appendix). Most of the data shown were recorded between April 29, 20.00 UTC and April 30, 02.37 UTC (Δt = 6.5 hours). In addition, we used two MODIS images acquired on April 29 at 11.00 UTC and April 30 at 03.35 UTC (Fig. 2.1) that enclosed the actual observation period. These images show that the temporal variability of the polynya extent was small during the period that is covered by the presented data.

2.2.1 Satellite data

Environmental Satellite (ENVISAT) SAR images were used to delineate polynya edges and high-resolution backscatter features in the thin ice zone. The ENVISAT C-band wide swath data is VV-polarized and covers an area of approximately 400 × 800 km^2 with a spatial resolution of 150 × 150 m^2. Level 1 data was obtained from the European Space Agency (ESA), automatically processed and send to field for campaign planning in near real-time with a mean delay of approximately 1.5 hours.

Level 1B calibrated radiances (visible and thermal infrared) from the MODIS sensor were provided by the U.S. National Aeronautics and Space Agency (NASA) Level 1 and Atmosphere Archive and Distribution System (LAADS), while adequate AVHRR data were acquired from the U.S. National Oceanic and Administration (NOAA) Comprehensive Large Array-data Stewardship System (CLASS). In this study, MODIS data were only used to produce an overview of the polynya area from the visible channels with 1 × 1 km^2 resolution and 0.25 × 0.25 km^2 enhanced resolution (Fig. 2.1). In terms of minimizing bias from ice growth and advection, the overpass time of AVHRR was more adequate for a detailed comparison with coincident data (compare Table 2.1, Appendix) .

Daily polar gridded microwave brightness temperatures (TB) from the SSM/I sensor and Advanced Microwave Scanning Radiometer (AMSR-E) Aqua L2A global swath spatially-resampled brightness temperatures (Ashcroft and Wentz, 2008) were acquired from the U.S. National Snow and Ice Data Center (NSIDC). In addition, satellite data with enhanced spatial resolution were obtained from the Microwave Earth Remote Sensing (MERS) Laboratory at Brigham Young University (BYU) Center for Remote Sensing (Long and Hicks, 2005). Here we use AMSR-E brightness temperatures and QuikSCAT backscatter coefficients reprocessed with the Scatterometer Image Reconstruction (SIR) method. The SIR data yield an enhanced effective spatial reso-

lution by recovering surface signals from irregularly distributed swath data (Early and Long, 2001).

Brightness temperatures and QuikSCAT backscatter coefficients are used to calculate polarization ratios which are necessary for the microwave retrieval of POLA and hi. Table (2.2, Appendix) provides an overview of the TB- and backscatter- derived parameters together with their specifications and equations as well as the product they can be inverted to.

AMSR-E sea ice concentration (Spreen and others, 2008; Kaleschke and others, 2001) for the date and area of interest was provided as a daily average (6.25 × 6.25 km^2) by the University of Hamburg. A sea ice concentration chart with a resolution of nearly 1 km^2 was produced from AVHRR surface temperature data. This is achieved by utilizing the relationship with fractional sea ice cover and open water area within one pixel (POTential Open WAter Algorithm, POTOWA, Druee and Heinemann (2004).

2.2.2 Airborne data

Ice thickness data from HEM measurements (hi_{HEM}) were acquired with a single-frequency (4.08 kHz) airborne electromagnetic system, a so called EM-Bird (Haas and others, 2009). The instrument was towed by a helicopter 10 to 15 meters above the ice surface. The method utilizes the contrast of electrical conductivity between sea water and sea ice to determine the distance to the ice-water interface. An additional laser altimeter yields the distance to the uppermost reflecting surface, hence hi_{HEM} is obtained as the ice plus snow thickness from the difference between the laser range and the EM derived distance. Since the laser beam is always reflected at the uppermost surface, snow thickness, if present, is included in hi_{HEM}. The measurements were taken with point spacing of 3 to 4 m depending on the speed of the helicopter. Within the footprint of a single measurement (40 - 50 m) the accuracy over level sea ice is in the order of ± 10 cm (Haas and others, 2009; Pfaffling and others, 2007). HEM measurements over the thin ice of the WNS polynya are challenging for two reasons: The processing of the EM-Bird data is based on the assumption that sea ice can be regarded as a non-conductive medium. Over thin ice however, this assumption may be invalid because the conductivity of saline young ice can be significantly higher than that of older first or multiyear ice. This can lead to an underestimation of the real ice thickness. Therefore all hi_{HEM} data have to be interpreted as minimum ice thicknesses. Second, the conductivity of the surface waters can be low and highly variable due to the proximity to the freshwater input by the Lena River. Although a water conductivity between 2200 and 2400 S/m was used for the retrieval of ice thicknesses, our processing algo-

rithms do not take into account conductivity variations during individual flights.

On all HEM flights, geo-coded aerial photographs were taken with a downward-looking digital camera (RICOH 500SE) connected to an external 1 Hz global positioning systen (GPS) device (Krumpen and others, 2010a). System calibration flights showed that the along-track accuracy of the GPS position of individual photographs was approximately ± 60 m. Camera height was obtained from the HEM-bird laser altimeter. Images were used to provide general information about ice conditions and to aid in the calibration of HEM ice thickness measurements and SAR image interpretation.

2.2.3 Polynya area retrieval

POLA (open water plus thin ice) is derived from the Polynya Signature Simulation Method (Kern, 2009; Arrigo and van Dijken, 2004; Renfrew and others, 2002) which provides a classification of thin ice and open water areas. The method uses microwave TB data and is based on the sensitivity of passive microwave polarization ratios (vertically minus horizontally polarized brightness temperature, normalized over their sum) to thin ice and open water. It combines the low atmospheric influence at 37 GHz with the higher spatial resolution at 85 GHz. This is accomplished by applying a threshold to the 85 GHz polarization ratio (PR85) maps and adjusting this threshold iteratively until the resulting classification agrees best with coincident 37 GHz maps. For the Ross Sea Polynya in the Antarctic, the average PR85 threshold is found to be at 0.085 (Kern and others, 2007). We slightly shifted this value in our analysis iteratively to assess its influence on the accuracy of POLA retrieval, in particular with respect to the spatial resolution and the influence of mixed pixels at the polynya edges. All in all, the PSSM allows for an increase of the spatial resolution of the input data to maximum 5×5 km^2. However, we used this output resolution of PSSM (PSSM$_5$) only with AMSR-E TB data (PR89, PR36, see Table 2.2, Appendix) to ensure a reliable retrieval of the 5×5 km^2 POLA. SSM/I TB data were only used to derive POLA on the 12.5×12.5 km^2 grid (PSSM$_{12}$).

2.2.4 Thin ice thickness retrieval

Surface temperatures were derived from AVHRR thermal infrared channels following the split-window method of Key and others (1997). We chose AVHRR instead of MODIS because its record time was closer to the SAR image record. Moreover, surface temperatures acquired in the absence of direct radiation improve the inversion to ice thickness since bi-directional albedo effects do not impede a retrieval of the surface radiation budget. The hi_{TH} was calculated using the surface energy balance model suggested by Yu and Lindsay (2003) with the aid

of NCEP/DOE meteorological reanalysis data (Kanamitsu and others, 2002). The thickness retrieval is based on the assumption that the heat flux through the ice equals the atmospheric heat flux. The method yields good results for ice thicknesses below 0.5 m assuming further that vertical temperature profiles within the ice are linear and no snow is present on top of the ice (Drucker and others, 2003). As this study presents a cross-validation, no truth reference data are declared. Nevertheless, we consider hi_{TH} and hi_{HEM} as most accurate among the presented data, simply because they provide the highest spatial resolution and were successfully applied in previous studies (Yu and Lindsay, 2003; Drucker and others, 2003; Kern and others, 2007; Pfaffling and others, 2007). The largest source of error in hi_{TH} probably arises from uncertainties in NCEP data. Especially in the proximity of a polynya, meteorological reanalysis data tend to underestimate near-surface air temperature and to overestimate near-surface wind speed. We performed an error analysis with hi_{TH} and NCEP data varying air temperature by ± 5°C and wind speed by ± 3°C. This resulted in maximum hi_{TH} errors of ± 20 %. Given the above mentioned NCEP uncertainties over a polynya (air temp. too low, wind speed too high), an underestimation of hi_{TH} within the ± 20 % error range is more likely than an overestimation.

Thin ice thickness was also derived from TB data using the polarization ratios of 37 GHz SSM/I (R37) and 36 GHz AMSR-E (R36) channels (Table 2.2, Appendix). The inversion to hi (hi_{R37}, hi_{R36}) is carried out by applying the exponential model derived by Martin and others (2004, 2005). Tamura and others (2007) used polarization ratios in the 85 GHz (PR85) and 37 GHz (PR37) SSM/I channels to infer thin ice thickness. They also suggested a correction scheme for atmospheric influences which should not be applied to the Northern Hemisphere without further investigation. In this study, we do not apply their methodology exactly, but rather use R85 and R89 (see Table 2.2, Appendix) to ensure a comparison of the feasibility of TB ratios rather than methodological details. As all previously used microwave proxies for thin ice are based on a regression with hi_{TH} data, the inversion to hi in this study is performed by applying an exponential fit to the relationship with hi_{TH} from this case study (see results and discussion sections). The use of 85 GHz and 89 GHz channels is associated with the problem that these data are subject to atmospheric disturbances. Thus, 36 GHz data from AMSR-E and Ku-band backscatter from QuikSCAT are used for comparison.

2.3 Results and discussion

2.3.1 General ice conditions and their representation in satellite data

The Western New Siberian Polynya (WNS) started to open on April 27, 2008 and reached its maximum width 2 days later, on April 29, 2008. Figure (2.1) shows that after opening, between April 29, 11.00 UTC (21.00 local time) and April 30, 03.35 UTC (13.35 local time), extent and position of the outer polynya edge were very stationary. The position of the fast ice edge is located at the long-term average, which coincides approximately with the position of the 20 m isobaths Bareiss and Goergen (2005). During the observation period, three automatic weather stations located along the fast ice edge measured south-easterly near-surface winds with 8 m/s and a daily average of near-surface air temperature of -15°C. The maximum width of the polynya between the fast ice edge and the down-wind pack ice is approximately 60 km while the south-western and north-eastern edges span a distance of nearly 250 km (Fig. 2.1).

Aerial photographs taken along the HEM flight track (compare Fig. 2.1) are shown in Figure (2.2). The open water close to the fast ice edge was partially covered by frazil ice streaks which were aligned parallel to the off-shore wind (image 1, section II). Open water width at the time of image acquisition was approximately 6 km. Further off-shore, frazil ice consolidated to thin and partly rafted ice with open water patches (image 2, section II). Image 3 shows a zone of broken thin ice pieces about to refreeze to a new consistent thin ice layer. With distance from the fast ice edge the rafting frequency increased (image 4-7, section II-IV), while the size and frequency of open water patches decreased (Krumpen and others, 2010a). Rafted floes with increased ice thicknesses are found at position 7 and a closed and rather levelled ice cover is prevailing at the end of the profile (image 8, section V). At the western edge of section V newly formed ice piles up against a region of older and deformed thin ice that was formed during a previous event.

Different thin ice age and thickness stages are distinguishable in the SAR scene taken on April 30, at 02.37 UTC (Fig. 2.3a). Three bands of different backscatter orientated parallel to the polynya edge (B1-B3, see Fig. 2.3a) were formed during an opening event on April 10 (B3), and two sequenced periods of strong wind speeds on April 24 (B2) and April 28 (B1). The corresponding surface temperatures from AVHRR infrared data (Fig. 2.3b) indicate decreasing temperatures with increasing distance from the fast ice edge.

The offshore edge of the polynya shows minimum surface temperatures of approximately -14°C which was close to the near-surface air temperature of -15°C. Maximum surface temperatures

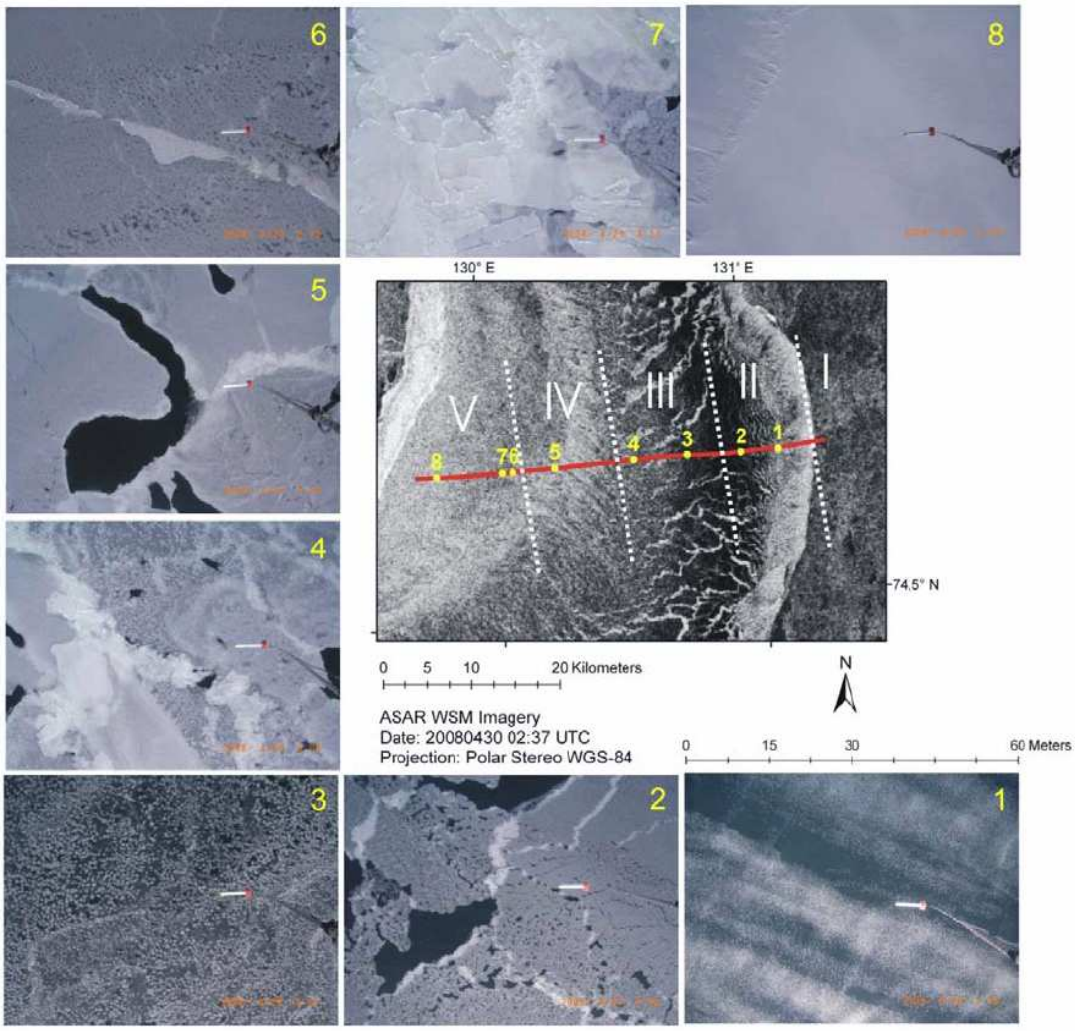

Figure 2.2: The central part of the figure is a SAR image of a part of the WNS polynya surveyed by helicopter during the polynya event on April 30, 2008 (compare Fig. 2.1 and 2.3a). Sections I-V indicate zones of different ice conditions with locations of aerial photographs (numbers 1-8) across the polynya. Photographs were taken at a- height of 50 m, covering a footprint of 60 × 40 m. The HEM-Bird is visible in the centre of images 1-8.

were found close to the fast ice edge and not higher than -4°C. This temperature is lower than expected for a region with large patches of open water (compare Fig. 2.2, section II) and most likely results from a new thin ice layer that formed between the acquisition of the aerial photographs and the AVHRR image. A composite of SAR backscatter and surface temperatures is presented in Figure (2.3c). Additionally, contour lines indicate boundaries between different thickness classes within the polynya as derived from hi_{TH} (shown later). Here, the prevailing ice thickness for the three bands B1-B3 shown in Figure (2.3a) are indicated. Ice thickness contours do not perfectly agree with the transition of the backscatter bands B1-B3. However, the youngest band (B1) is characterized by thicknesses mostly below 0.1 m. Thicker ice of 0.1 m to

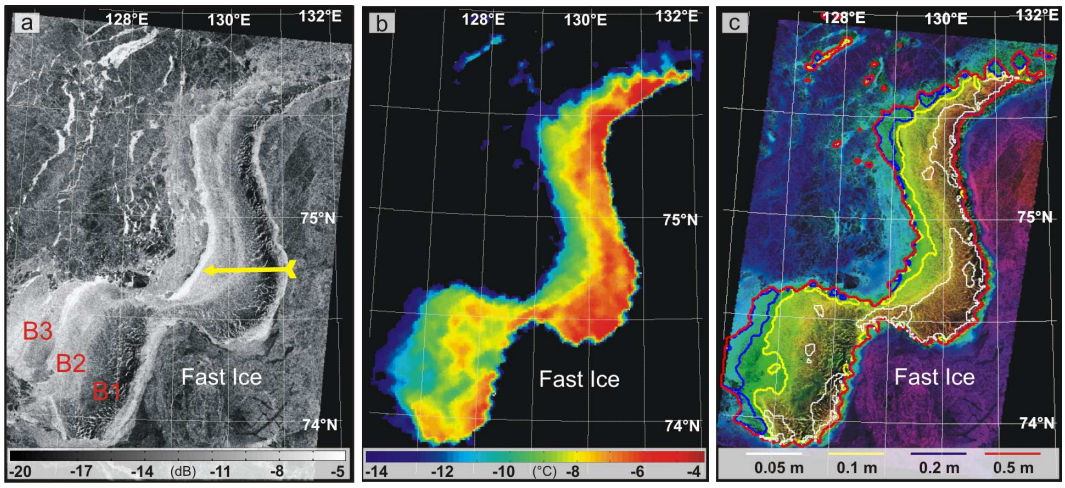

Figure 2.3: Western New Siberian polynya. a) ENVISAT SAR backscatter (dB) for April 30, 2008 (02.37 UTC). Characteristic backscatter bands B1-B3 and the helicopter flight track from April 39 at 02.54 UTC are indicated. b) Surface temperature (between -14°C and -4°C) as derived from AVHRR IR brightness temperatures from April 29, 2008 at 20.00 UTC. c) Composite of a) and b) together with contour lines (0.05 m, 0.1 m, 0.2 m, 0.5 m) of the thermal ice thickness hi_{TH} (derived from data in b).

0.5 m is found in bands B2 and B3. The increase in density of the thin ice contour lines at the off-shore edge is probably related to an increased dynamic ice growth through ice advection and compression.

Coincident enhanced resolution (SIR) QuikSCAT backscatter and two sea ice concentration products are shown in Figure (2.4). The gridded daily average reveals increasing backscat-

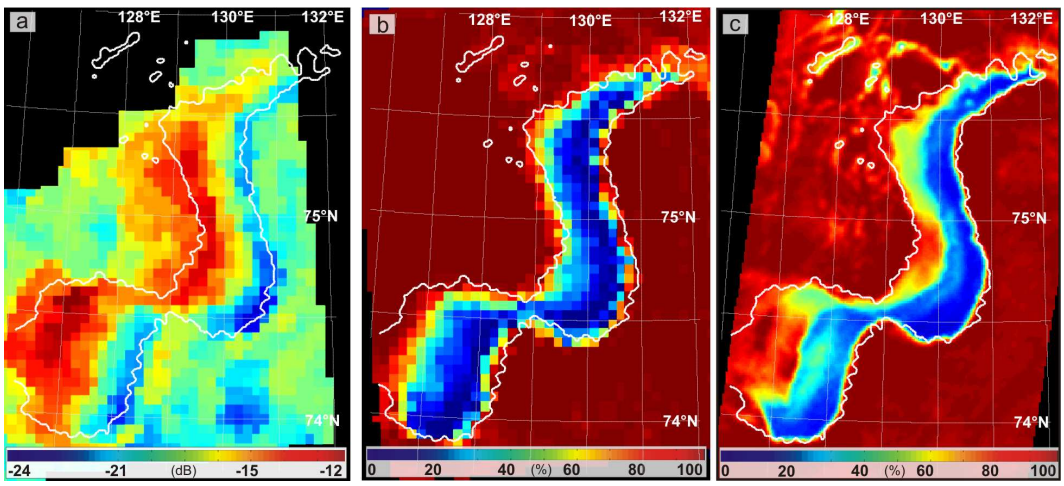

Figure 2.4: a) QuikSCAT SeaWinds backscatter (horizontal polarization) from Scatterometer Image Reconstruction (SIR) data on April 29, 2008. b) ASI sea ice concentration (daily average) from AMSR-E data for April 29, 2008. c) POTOWA sea ice concentration derived from AVHRR surface temperatures for April 29, 2008 at 20.00 UTC (see Fig. 2.2b) at the Western New Siberian polynya. The 0.5 m ice thickness contour line from hi_{TH} is shown as a white line.

ter towards the off-shore edge. This agrees partly with the linear backscatter gradient found in the ENVISAT C-band imagery (Fig. 2.3a). The resolution of 6 × 6 km^2 impedes a more detailed detection of thin ice features and increases the disturbing influence of mixed pixels at the polynya edge. The daily averaged ASI sea ice concentration (Spreen and others, 2008; Kaleschke and others, 2001), Fig. 2.4b) with a resolution of 6.25 × 6.25 km^2 indicates the effect of thin ice on the sea ice concentration retrieval (Kwok and others, 2007) through a significant underestimation of sea ice concentrations. The same applies for POTOWA sea ice concentrations (Druee and Heinemann, 2004) as derived from surface temperatures with a resolution of approximately 1 × 1 km^2 (Fig. 2.4c).

2.3.2 Comparison of different POLA and hi retrievals

An accurate estimation of POLA and hi is the most crucial step for a long-term polynya monitoring with respect to ice production. PSSM POLA was derived from AMSR-E swath data with a PR89 threshold of 0.070, yielding a resolution of 5 × 5 km^2 (PSSM_5^{070}, Fig. 2.5a, white line). In comparison, PSSM POLA from SSM/I data is shown for PR85 thresholds of 0.070 and 0.085 (PSSM_{12}^{070}, grey line and PSSM_{12}^{085}, black line). The 0.070 threshold was applied in contrast to the 0.085 threshold to achieve best alignment with polynya edges as identified in the visible and SAR satellite data (Fig. 2.1 and 2.3). Figure (2.5a) shows that the coarse resolution of PSSM_{12} suffers from large inclusions of fast and pack ice area. POLA derived from PSSM^{070} in each case does not include ice thicker than approximately 0.2 m. This is commensurate with results of Kern and others (2007), where the applicability of PSSM was limited to hi of less than 0.25 m.

The spatial distribution of R85, R36, R89 and $\mathrm{R36}_{SIR}$ (compare Table 2.2, Appendix) is presented in Figures (2.5b-e). Each of these ratios is expected to correlate inversely with hi for thicknesses less than 0.2 m (Naoki and others, 2008). In addition, the backscatter polarization ratio QR_{SIR} is shown in Figure (2.5f) . R85 and R36 show maximum values in the polynya center (Fig. 2.5b, 2.5c). This seems implausible and indicates a source of error through the contribution of low R values from fast ice, that affect the signal due to the comparably large field of view of the sensor (see Table 2.2, Appendix). Thin ice in the proximity of the fast ice edge (see 0.05 m contour line) should instead respond with high R36 and R85 according to Naoki and others (2008).

A more reasonable spatial distribution is revealed in R89, $\mathrm{R36}_{SIR}$ and QR_{SIR} (Fig. 2.5d). Here, the TB ratio is inversely related to hi as indicated through the 0.5 m and 0.05 m contour lines. The absence of this pattern in R85 and R36 values can be explained with the lower spatial resolution (12.5 × 12.5 km^2) as compared with R89 (6.25 × 6.25 km^2), $\mathrm{R36}_{SIR}$ (9 × 9 km^2) and QR_{SIR}

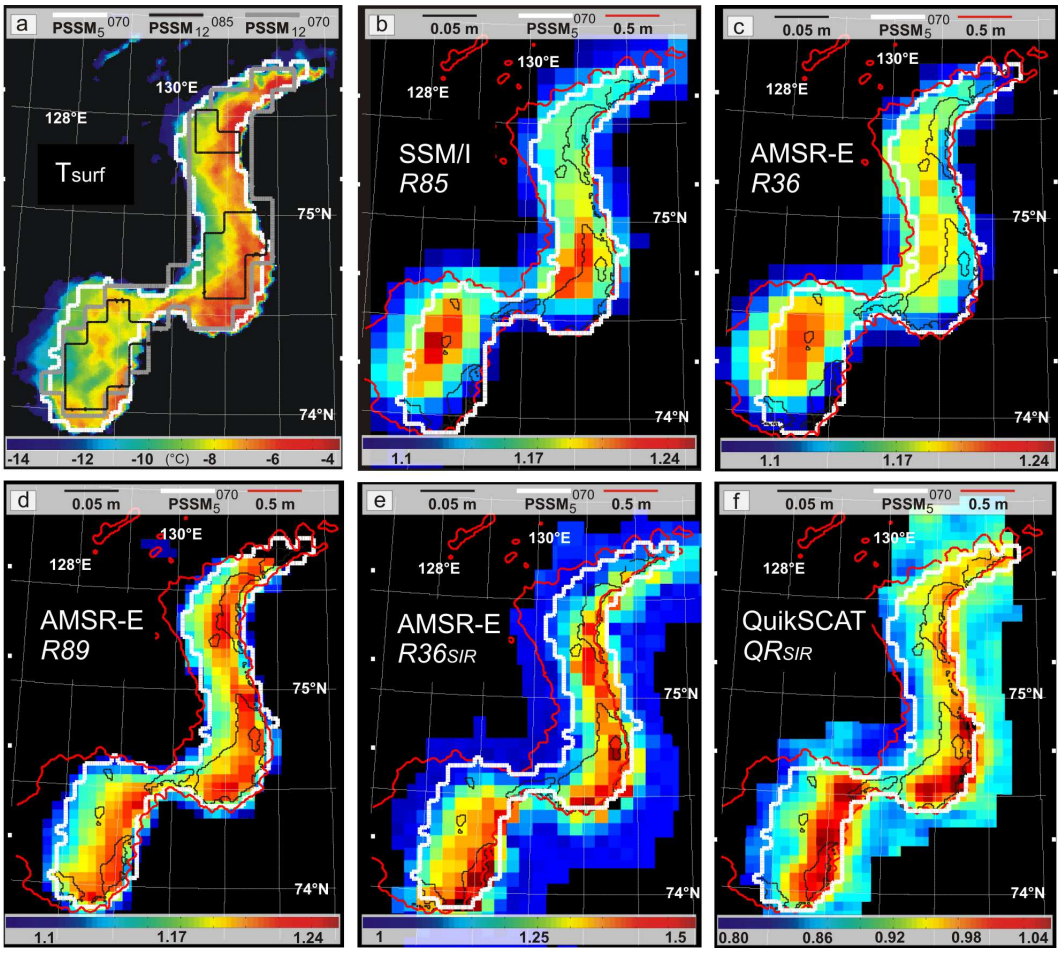

Figure 2.5: PSSM polynya area. a) Surface temperatures (between -14°C and -4°C) as derived from AVHRR IR brightness temperatures from April 29, 2008 at 20.00 UTC and AMSR-E ($PSSM_5^{070}$, white line) and SSM/I ($PSSM_{12}^{070}$, grey line and $PSSM_{12}^{085}$, black line) microwave brightness temperatures. b) R85. c) R36. d) R89. e) R36 from AMSR-E enhanced resolution SIR data. f) QuikSCAT enhanced resolution SIR data polarization ratio H/V, with 0.05 m (black) and 0.5 m (red) hi_{TH} ice thickness contour lines as well as $PSSM_5^{070}$ polynya area (white).

(6×6 km^2). Here, the resolution of the gridded data is less important than the actual field of view (FOV) of the sensor (compare Table 2.2, Apendix). Due to a large FOV, fast ice areas are contributing with very low R36 and R85 values to pixels covering the transition between fast ice and polynya, thus masking out high R36 and R85 values resulting from thin ice.

We performed an exponential fit between R values and hi_{TH} data from our case study to obtain an inversion from microwave data to hi. Results show that R36 and R85 values are rising with increasing hi_{TH} (Fig. 2.6a, b). This contradicts the in-situ based findings of Naoki and others (2008) and results from mixed microwave signals at the fast ice edge, spoiling the thin ice signature through comparably low R values (compare Fig. 2.5b, c). The R89, $R36_{SIR}$ and QR_{SIR} correlations with hi_{TH} (Fig. 2.6c, d, e) show decreasing R values with increasing hi. This in-

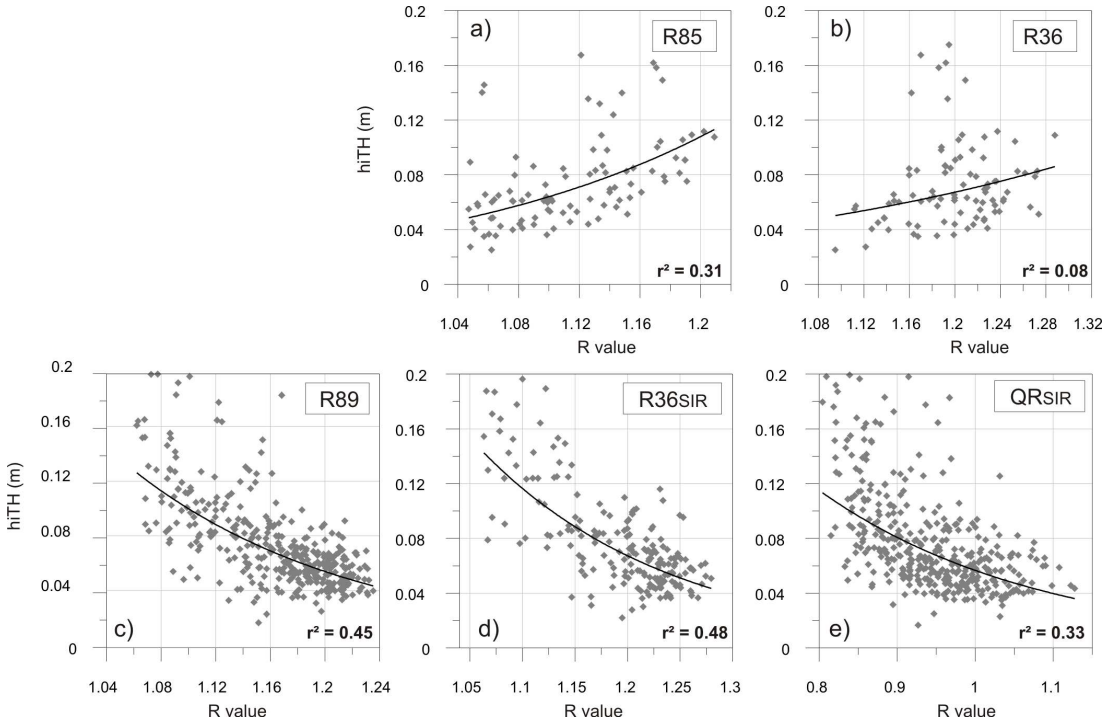

Figure 2.6: Scatterplot of thermal ice thickness hi_{TH} vs. a) R85 ($hi_{R85} = exp^{(5.2 \times R85)} \times 0.0002$; $r^2 = 0.31$), b) R36 ($hi_{R36} = exp^{(2.8 \times R36)} \times 0.002$; $r^2 = 0.08$), c) R89 ($hi_{R89} = exp^{(-6.2 \times R89)} \times 86.2$; $r^2 = 0.45$), d) R36$_{SIR}$ ($hi_{R36(SIR)} = exp^{(-5.49 \times R36_{SIR})} \times 48.59$; $r^2 = 0.48$), and e) QR$_{SIR}$ ($hi_{QR(SIR)} = exp^{(-3.55 \times QR_{SIR})} \times 1.96$; $r^2 = 0.33$). Black lines show exponential fits used for the inversion in Figure (2.7b-f).

terrelationship is commensurate with other studies (i.e. Tamura et al., 2007). R89 and R36$_{SIR}$ provide a similar quality for the inversion to hi ($r = 0.45$ and 0.48, respectively). Taking into account that the atmospheric influence on the 36 GHz TB channels is negligible compared with that in the 89 GHz channels, R36$_{SIR}$ seems to provide a convenient proxy for operational hi retrievals. The performance of QR$_{SIR}$ (Fig. 2.6e) appears to be much better for $hi < 0.1$ m. For thicker ice, QR$_{SIR}$ increases significantly. This deteriorates the exponential fit in the entire hi range from 0 to 0.2 m.

The result of the hi retrieval is presented in Figure (2.7). Values are only shown for the area that was classified as a polynya through PSSM$_5^{070}$. The hi_{TH} (Fig. 2.7a) shows that almost the entire polynya is covered with ice of less than 0.1 m thickness. Thicknesses of up to 0.5 m can only be found close to the off-shore polynya edge and thicknesses of less than 0.05 m are limited to regions close to the fast ice edge (Fig. 2.7a, contour lines).

The hi_{R85} (Fig. 2.7b) as derived from the exponential model (Fig. 2.6a) yields a reasonable spatial variability of hi within the polynya. However, one has to be cautious because this model does not explain the physical relationship between R values and hi. The positive correlation

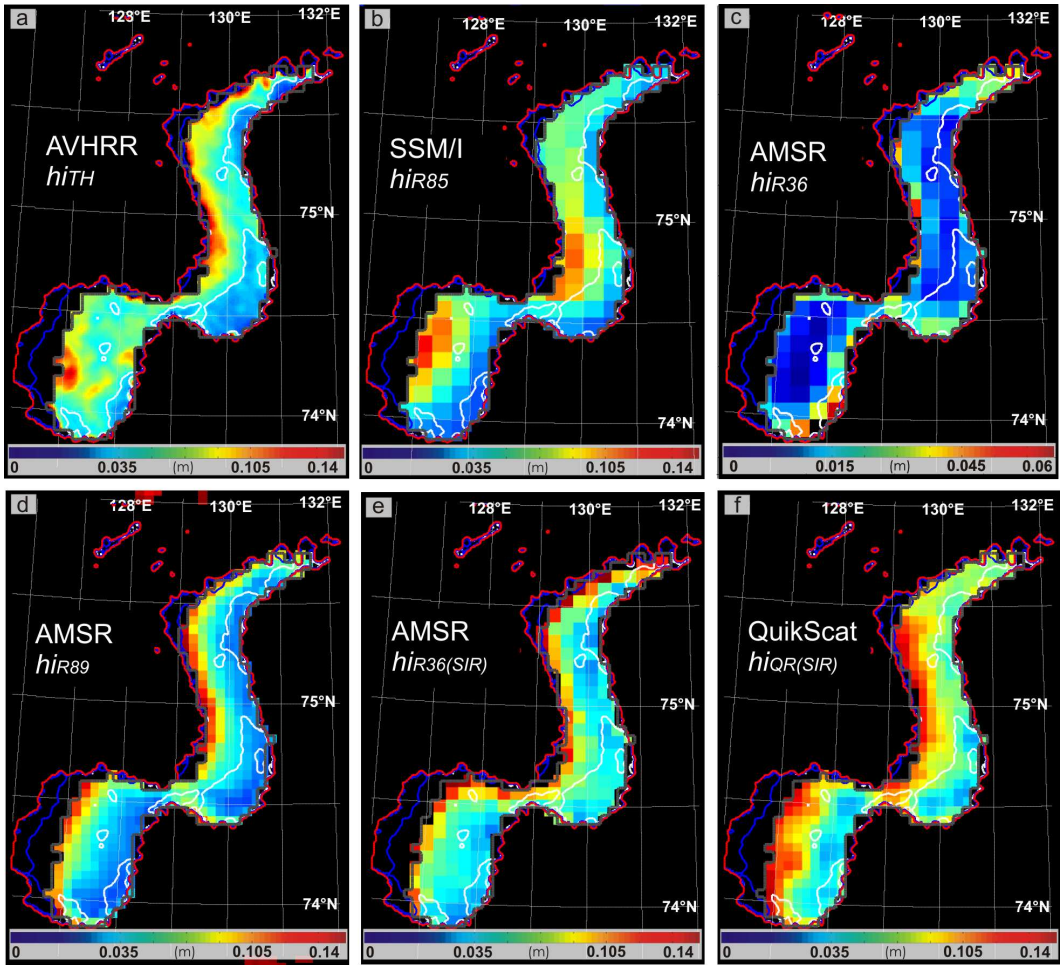

Figure 2.7: a) Thermal ice thickness (hi_{TH}) as derived from AVHRR surface temperatures from April 29, 2008 at 20.00 UTC. b) Thin ice thickness hi_{R85} as derived from R85 (see Fig. 2.6a). c) Thin ice thickness hi_{R36} as derived from R36 ((Martin and others, 2005), see Fig. 2.6b). d) Thin ice thickness hi_{R89} as derived from R89 (see Fig. 2.6c). e) Thin ice thickness $hi_{R36(SIR)}$ as derived from R36$_{SIR}$ (Fig. 2.6d). f) Thin ice thickness $hi_{QR(SIR)}$ as derived from QR$_{SIR}$ (Fig. 2.6e). Gridded ice thickness data are shown for POLA as detected with PSSM$_5^{070}$ (grey line), and hi_{TH} contour lines from data in a) are shown for 0.05 m (white), 0.2 m (blue) and 0.5 m (red).

between R85 and hi_{TH} (compare Fig. 2.6a) allows for an exponential fit for the two parameters but represents a significant source of error since it results from the unwanted influence of fast ice that contributes to the sensor's field of view area. hi_{R36} (Fig. 2.7c) as derived according to Figure (2.6b) yields an insufficient result due to the bad correlation of R36 and hi_{TH}.

The thickness parameters hi_{R89}, $hi_{R36(SIR)}$ and $hi_{QR(SIR)}$ represent reasonable spatial distributions of hi within the polynya (Fig. 2.7d-e). Here, the inversion is based on a reliable correlation (compare Fig. 2.6) and the obtained hi is continuously increasing across the polynya with maximum thicknesses of 15 cm within the PSSM$_5^{070}$ area. As stated above, $hi_{QR(SIR)}$ overestimates ice thickness in the range above 10 cm.

Results of the retrieval of POLA and average hi within the polynya are summarized in Table (2.3, Appendix). Surface temperatures, as derived from IR brightness temperatures, yield a convenient spatial resolution for polynya monitoring. The hi_{TH}, which was calculated from these data, results in a POLA value of 11.4 × 10^3 km^2 if values of hi < 0.5 m are considered a polynya and a POLA of 10.2 × 10 km^2 if the hi threshold is set to 0.2 m. The average hi results in 0.1 m for the first case and in 0.07 m for the latter. SSM/I TB data give a POLA value of 4.9 × 10^3 km^2 (with avg. hi_{R85} of 0.03 m) using PSSM$_{12}^{085}$ and 10.5 × 10^3 km^2 (with avg. hi_{R85} of 0.06 m) for PSSM$_{12}^{070}$. In comparison, AMSR-E TB data give a POLA value of 7.7 × 10^3 km^2 (with avg. hi_{R36} of 0.03 m and hi_{R89} of 0.05 m) using PSSM$_5^{085}$ and a POLA of 10.3 × 10^3 km^2 (with avg. hi_{R36} of 0.03 m and hi_{R89} of 0.07 m) using PSSM$_5^{070}$. Average $hi_{R36(SIR)}$ and $hi_{QR(SIR)}$ within PSSM$_5^{070}$ POLA amount to 0.08 m and 0.07 m, respectively.

Previous studies have found that hi retrieval from microwave data is only possible for hi < 0.2 m (Naoki and others, 2008). Therefore, one should only compare POLA and hi from microwave data with hi_{TH} values < 0.2 m. In doing so, the best agreement is found using the high-resolution microwave thin ice proxies (hi_{R89}, $hi_{R36(SIR)}$, $hi_{QR(SIR)}$) with PSSM$_5^{070}$ for POLA. As stated above, this is primarily an effect of the higher spatial resolution allowing for a better separation between thin ice and fast ice / pack ice at the polynya edges.

Using the spatial distribution of hi_{TH} < 0.2 m as a POLA reference, this case study shows that POLA derived from TB data is underestimated by as much as 50 % (30 %) when a PR85 threshold of 0.085 is applied instead of 0.070 with PSSM$_{12}$ (PSSM$_5$).

Although average hi values do not differ extremely, one has to be aware that the ice thickness profiles within the polynya are poorly represented by hi_{R36} (Fig. 2.7).

2.3.3 Comparison of profiles across the polynya

A comparison of different satellite and airborne parameters along the HEM profile (see Fig. 2.1 and 2.2) is shown in Figure (2.8). The helicopter track across the polynya led from the fast ice edge in the East (right hand side in Figure (2.8) towards the pack ice in the West (left hand side in Fig. 2.8), spanning a distance of roughly 45 km. SAR and QuikSCAT backscatter as well as normalized reflection from MODIS channel 1 increase along-track with distance from the fast ice edge (Fig. 2.8a). Lowest radar backscatter as well as the darkest surfaces are found immediately adjacent to the fast ice edge of the polynya (section II), where open water with frazil ice streaks are prevalent (Fig. 2.2, image 1). The along-track variability of the SAR linear backscatter values is higher than the brightness scatter from the visible channel (both data sets were resampled

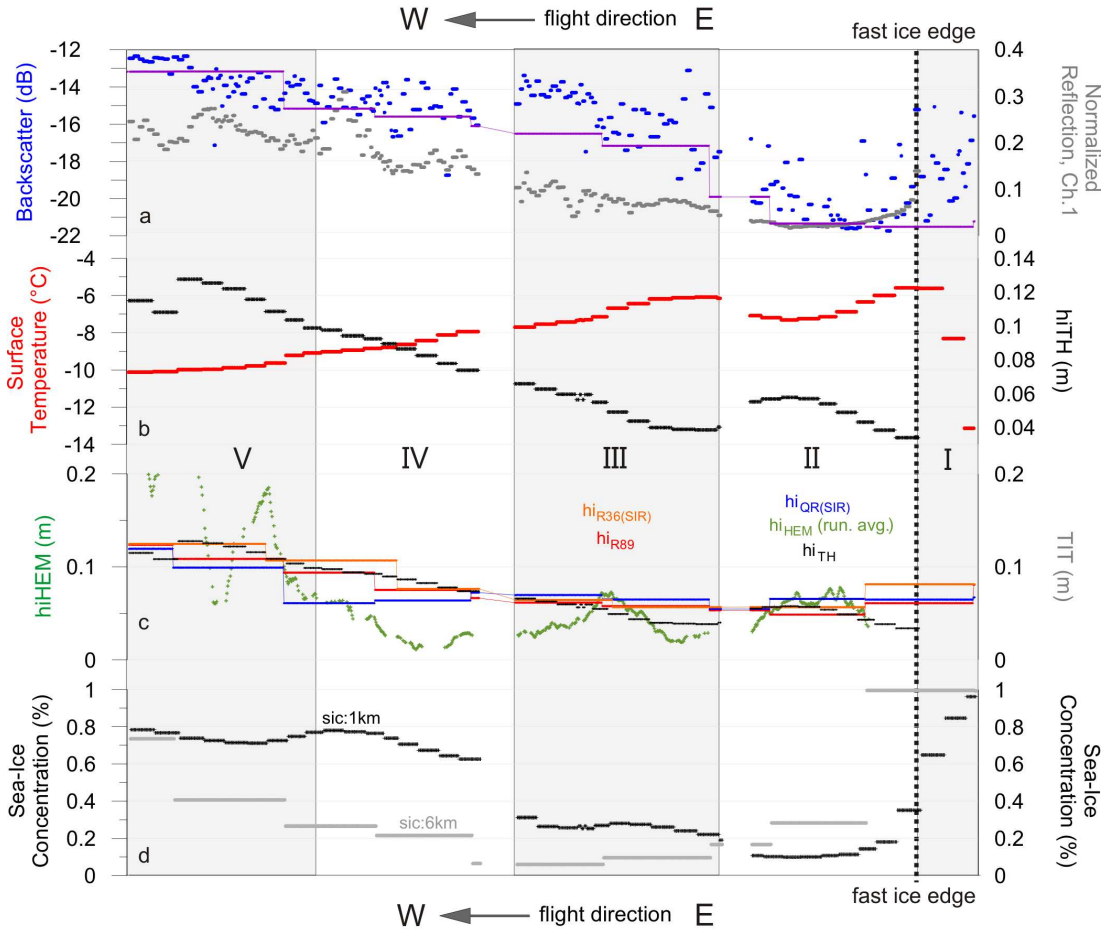

Figure 2.8: Along-track profiles of different satellite and airborne parameters. a) SAR backscatter (blue), QuikSCAT inner beam (horizontal polarization) backscatter from Scatterometer Image Reconstruction (SIR) data (purple) and swath-normalized reflection in MODIS channel 1 (grey). b) Surface temperature from AVHRR IR brightness temperatures (red) and the thermal ice thickness hi_{TH} (black). c) HEM-Bird ice thickness hi_{HEM} (green, running average, n = 23), $hi_{R36(SIR)}$ ice thickness (orange), hi_{R89} ice thickness (red), $hi_{QR(SIR)}$ ice thickness(blue) and thermal ice thickness hi_{TH} (black). d) Sea ice concentration as derived from microwave data (grey) and from AVHRR IR brightness temperatures (black) for swath data as given in Table (2.2, Appendix). Grey (shaded) boxes denote different sections as described in the text and shown in Figure (2.2).

to a spatial resolution of 200 m). Coincident values of the AVHRR surface temperature reveal an almost constant decrease from -6°C to -10°C along the EM-track (Fig. 2.8b, red curve). The hi_{TH} (Fig. 2.8, black curve) shows thin ice of 4 cm minimum in section II. The indicated lack of open water results from cold frazil ice streaks which decrease average surface temperatures below freezing (Fig. 2.2, image 1). Thicker ice up to 13 cm is found at the end of the profile (Fig. 2.8b, black curve). An intermediate hi_{TH} minimum of 4 cm occurs at about one third of the profile after ice thickness had initially increased to 6 cm (transition from section II-III). This could be a result of a more consistent ice cover at this position (Fig. 2.2, image 3) in comparison

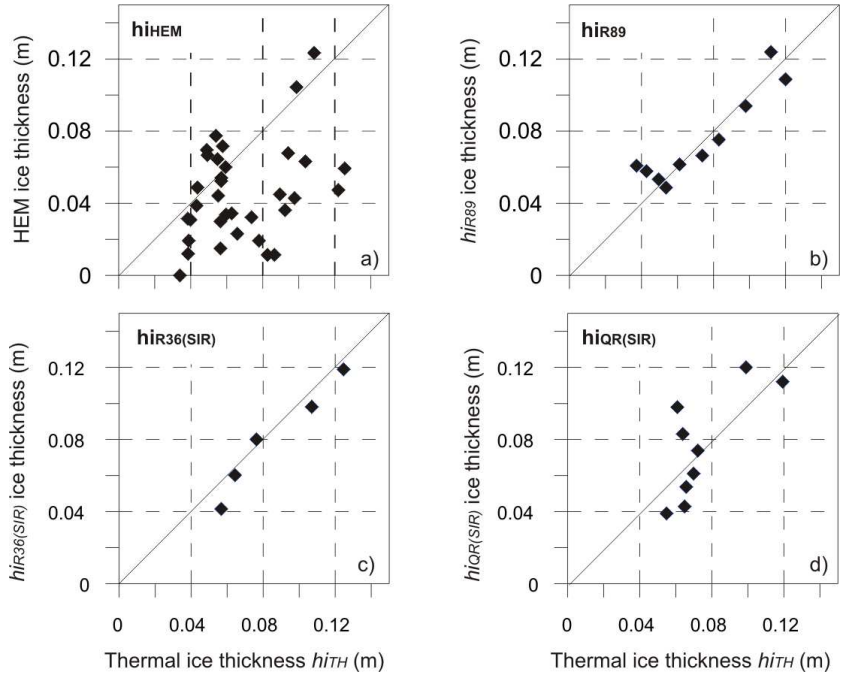

Figure 2.9: Scatterplots of coincident along-track data. a) HEM ice thickness hi_{HEM} vs. thermal ice thickness hi_{TH}, b) hi_{TH} vs. hi_{R89} ice thickness, c) hi_{TH} vs. $hi_{R36(SIR)}$ and d) hi_{TH} vs. $hi_{QR(SIR)}$. Data pairs are interpolated to the grid with the smaller resolution.

to the centre of section II (Fig. 2.2, image 3).

In Figure (2.8c), different retrievals of hi are shown in comparison. In addition to hi_{TH} (black line), $hi_{R36(SIR)}$ (orange line), hi_{R89} (red line), $hi_{QR(SIR)}$ (blue line) and hi_{HEM} (green line, running average, n = 29) are shown. The microwave based hi values reasonably depict the along-track increase in hi_{TH} (black curve and Fig. 2.8b). hi_{R36} is not shown because of bad performance in this case study.

The hi_{HEM} is characterized by large deviations from the microwave and temperature retrievals at the end of the profile (section V). Here, hi_{HEM} values reach up to 30 cm as averaged over approximately 1 km width (corresponding to a 23-point running average), while hi from microwave data and hi_{TH} do not exceed 13 cm. The opposite is found in section IV, where hi_{HEM} values are up to 7 cm lower than $hi_{R36(SIR)}$, hi_{R89}, $hi_{QR(SIR)}$ and hi_{TH}. Discrepancies between the hi_{HEM} and the hi_{TH} data are more a result of uncertainties in the HEM data than in the satellite retrievals. Even with older, thicker ice with a lower conductivity the HEM measurements are only accurate to within ± 0.1 m (Haas and others, 2009; Pfaffling and others, 2007). Therefore, a comparison of results with thicknesses in the range of 0 to 0.15 m is very challenging. Large deviations of hi_{HEM} from hi_{TH} as found in section IV and V might be explained with local variations of the water conductivity. The best fit is found in section II, where absolute val-

ues and qualitative changes agree well.

Figure (2.8d) moreover illustrates the effect of thin ice on sea ice concentration algorithms. Microwave- as well as temperature-derived sea ice concentrations are both subject to the presence of thin ice causing an underestimation of actual sea ice concentrations.

The concordance of the results of different hi retrieval methods is summarized in Figure (2.9, with data pairs interpolated to the lower resolved grid). hi_{TH} and hi_{HEM} correlate reasonably up to thicknesses of 0.1 m with hi_{TH} exceeding hi_{HEM} constantly by about 3 - 4 cm. Above hi values of 0.1 m, hi_{HEM} is significantly larger than hi_{TH} (Fig. 2.9a).

A good relationship is revealed for hi_{R89} and hi_{TH} (Fig. 2.9b), which is not surprising, taking into account that the first is derived in an exponential relationship from the latter (Fig. 2.6). Less data points, but a similar agreement is found for $hi_{R36(SIR)}$. The $hi_{QR(SIR)}$ again reveals an overestimation of hi for ice thicker than 0.08 to 0.1 m.

2.3.4 Implications for long-term and large-scale investigations of polynya dynamics

Together with meteorological data and/or results from regional climate models, remote sensing offers great potential to derive polynya dynamics (Kern and others, 2007; Arrigo and van Dijken, 2004; Dokken and others, 2002) and thin ice thickness that can be used to calculate heat loss and ice production (Tamura and others, 2008; Martin and others, 2005). As confirmed in our study, the hi retrieval approaches suggested by Martin and others (2005), Naoki and others (2008) and Tamura and others (2007) provide information on the spatial variability of ice thicknesses below 0.2 m within the polynya. However, our case study reveals strong limitations in narrow polynyas due to the coarse resolution of the microwave data. The thin ice microwave signature is affected by the proximity of the fast and pack ice with different emissivities. This might be negligible where the area/edge ratio is high and apparently, most microwave data can be successfully used in larger polynyas (Kern and others, 2007; Tamura and others, 2007; Martin and others, 2005). In long and narrow flaw polynyas, where the fraction of nonedge pixels is comparably small, the influence of microwave signals from the fast and pack ice becomes a major source of error in the thickness retrieval. Hence, as the width of the polynya decreases, the spatial resolution of the input data becomes increasingly important. For the case study presented here, AMSR-E 89 GHz, AMSR-E 36 GHz (SIR) and QuikSCAT (SIR) data reasonably depicted the across-polynya ice thickness increase as indicated by hi_{HEM} and hi_{TH}. Using hi_{R89} for a long-term monitoring of hi is impeded by non-negligible atmospheric influences in the frequency range of 80-89 GHz, such that atmospheric correction schemes would have to

be carefully applied. However, the enhanced resolution image products from AMSR-E 36 GHz and QuikSCAT data indicate good potential for an operational thin ice monitoring.

With respect to the influence of regional particularities, one has to take into account that the microwave properties of sea ice formed in the Laptev Sea may differ from those of sea ice in other regions. The relatively fresh surface waters originating from Lena River, one of the largest rivers in the Arctic, will influence the dielectric properties of sea ice forming in this region. As microwave properties of sea ice depend critically on sea ice properties related to salinity and porosity, a careful validation of algorithms is required before they can be more routinely applied. The same applies for polynya area detection with PSSM. If used in narrow flaw polynyas, the results are very sensitive to the thresholds used to discriminate between thick and thin ice.

Barber and Massom (2007) identified more than 60 recurring polynyas in the Northern Hemisphere. Since most of these are comparably small in extent, a long-term monitoring would require high-resolution microwave satellite data. Regionally limited studies are applicable if the parameters are chosen carefully and validation with high-resolution data is performed (Kern, 2008; Martin and others, 2005). Previous long-term hemispheric studies (Tamura and others, 2008) of ice production do not take into account the fraction of narrow polynyas and the accompanying influence of mixed signals at the polynya edges, possibly causing major errors in the hi retrieval.

As shown by Dokken and others (2002), SAR imagery provides a reasonable means to derive polynya area and shape. Long-term and large-scale investigations with SAR data require substantial effort compared to using PSSM with passive microwave data. An automatic thin ice area retrieval from SAR is impeded by highly variable backscatter features of thin ice (bare thin ice, frost flowers, rafting). Scatterometer data (SeaWinds, Fig. 2.4) are apparently somewhat sensitive to hi. However, the thin ice backscatter variability applies here in the same way as with SAR data. The sensitivity of sea ice concentrations to thin ice (Kwok and others, 2007) might provide a proxy for hi. Determining if open water or thin ice are responsible for low sea ice concentrations is arbitrary however, if not validated with hi data and/or in-situ measurements.

In the entire Laptev Sea flaw polynya, part of which is represented by the WNS in our case study, the winter ice production for the winter of 1991/1992 was estimated to be 258 km^3 (Dethleff and others, 1998) which equals about 9 % of the volume of the Siberian Branch of the Transpolar Drift. Thus, an investigation of the long-term variability of ice formation in this area would be of substantial interest for an assessment of Arctic sea ice variability. Our results

indicate that SSM/I data can be used to determine POLA from the PSSM method. However, an accurate hi retrieval requires sensors or data products with a higher spatial resolution.

2.4 Summary and conclusions

The Western New Siberian polynya in the Laptev Sea is investigated by a combination of multi-sensor satellite and airborne data. Our goal was to assess the feasibility of various polynya monitoring methods with respect to long-term investigations of polynya dynamics and ice formation within this area.

Results show that a major source of error in the derived ice thickness information arises from the influence of mixed water, thin and thick ice signals at the polynya edge when coarse resolution microwave data are used. Using enhanced resolution data products indicates potential for a significant improvement of thin ice monitoring.

Long-term polynya studies need to account for regional particularities of polynya size and shape. Large-scale studies might suffer from errors in the thickness retrieval when coarse resolution microwave data are used. The retrieval of polynya area by means of the Polynya Signature Simulation Method is very sensitive to applied thresholds and can easily be underestimated by as much as 50 %.

In this study we present helicopter-based high-resolution ice thickness data (hi_{HEM}). These observations show that the spatial variability of ice thickness is largely smoothed out using infrared (hi_{TH}) or microwave data. Nevertheless, hi_{TH}, and hi_{R89}, $hi_{R36(SIR)}$, and $hi_{QR(SIR)}$ in the presented case study capture the across-polynya increase in ice thickness, while the accuracy of thin ice retrieval from 36 GHz, 37 GHz and 85 GHz TB channels is significantly reduced by the low spatial resolution.

Our results imply that previously suggested algorithms for the regional-scale detection of thin ice thickness from microwave data are not necessarily transferable to the Laptev Sea. Long-term studies in this region need to take into account specific polynya features, such as prevailing surface salinities and the fraction of nonedge pixels.

2.5 Acknowledgments

The helpful comments of three anonymous reviewers are kindly acknowledged. This study was funded by the German Ministry for Education and Research (BMBF) within the framework of the joint German-Russian project 'System Laptev Sea', under grant 0360639E. The authors

kindly acknowledge exchange and helping hands during field campaigns from other project members and Russian colleagues. We are also very grateful to Thorsten Markus and Stefan Kern for informative and instructive personal communication. ENVISAT SAR images were obtained through ESA AO-project AO500. AVHRR images were provided by CLASS/NOAA, MODIS images by LAADS/NASA, AMSR-E/SSM/I brightness temperatures and NASA TEAM sea ice concentrations by the U.S. NSIDC, AMSR-E ASI sea ice concentrations by the University of Bremen and QuikSCAT as well as AMSR enhanced resolution data Scatterometer Image Reconstruction data by the BYU Center for Remote Sensing.

2.6 Appendix

Table 2.1: Overview of raw data, sensors and platforms, derived parameters, source of acquisition and time of record for all the data presented in this study. Note: SSM/I brightness temperatures and SeaWinds scatterometer data were used as daily averages for April 29, 2008 because no suitable swath data were available.

Sensor	Platform and specifications	Derived parameters	Source	Record time
Satellite				
MODIS	Terra, MOD02QKM	Visible: normalized reflection	LAADS	April 29, 1100 UTC April 30, 0335 UTC
AVHRR	NOAA-15, LAC	Surface temperature, hi_{TH}, sea ice concentration	CLASS	April 29, 2000 UTC
ASAR	ENVISAT	Surface backscatter	ESA	April 30, 0237 UTC
SSM/I	DMSP F-13	TB, PSSM POLA, hi_{R37}, hi_{R85}	NSIDC	April 29, daily avg.
AMSR-E	Aqua	TB, PSSM POLA, hi_{R36}, hi_{R89}	NSIDC	April 29, 2134 UTC
AMSR-E	Aqua	TB_{SIR}, $hi_{R36(SIR)}$	BYU	April 29, daily avg.
SeaWinds	QuikSCAT	Backscatter$_{SIR}$, $hi_{QR(SIR)}$	BYU	April 29, daily avg.
Airborne				
HEM-Bird	Helicopter	hi_{HEM}	AWI	April 29, 02.54 UTC
Orthographic camera	Helicopter	Surface photography	AWI	April 29, 02.54 UTC

Table 2.2: Overview of TB channels used (V denoting vertical and H denoting horizontal polarization), frequency, field of view of sensor channels (FOV), equations, retrieved parameters, effective spatial resolution on grid, and names of methods.

Sensor data	Frequency (GHz)	FOV (km)	Parameter ID	Equation	Retrieved quantity	Method	Name	Spatial resolution on grid (km)
SSM/I	85	15 × 13	PR85	(85V-85H)/(85V+85H)	POLA	PSSM	$PSSM_{12}$	12.5 × 12.5
SSM/I	37	37 × 28	PR37	(37V-37H)/(37V+37H)	POLA	PSSM	$PSSM_{12}$	12.5 × 12.5
AMSR-E	89	6 × 4	PR89	(89V-89H)/(89V+89H)	POLA	PSSM	$PSSM_5$	5 × 5
AMSR-E	36	14 × 8	PR36	(36V-36H)/(36V+36H)	POLA	PSSM	$PSSM_5$	5 × 5
SSM/I	37	37 × 28	R37	37V/37H	hi	(Martin and others, 2004)	hi_{R37}	25 × 25
SSM/I	85	15 × 13	R85	85V/85H	hi	Exp. fit (Fig. 2.6)	hi_{R85}	12.5 × 12.5
AMSR-E	36	14 × 8	R36	36V/36H	hi	(Martin and others, 2004)	hi_{R36}	12.5 × 12.5
AMSR-E	89	6 × 4	R89	89V/89H	hi	Exp. fit (Fig. 2.6)	hi_{R89}	6.25 × 6.25
AMSR-E (SIR)	36	14 × 8	$R36_{SIR}$	36V/36H	hi	Exp. fit (Fig. 2.6)	$hi_{R36(SIR)}$	10 × 10
QuikSCAT (SIR)	13.4	35 × 25	QR_{SIR}	σ^0V/σ^0H	hi	Exp. fit (Fig. 2.6)	$hi_{QR(SIR)}$	6 × 6

Table 2.3: Comparison of polynya area (POLA) and average thin ice thickness (hi) within the polynya as derived from the various algorithms discussed in the paper. a) Thermal ice thickness data hi_{TH} for POLA (as indicated by the 0.2 m and 0.5 m contour lines) and hi. b) SSM/I microwave brightness temperatures with PSSM (in different parameterizations) for POLA and with hi_{R37} and hi_{R85} for hi. c) AMSR-E microwave brightness temperatures with PSSM (in different parameterizations) for POLA and with hi_{R36} and hi_{R89} for hi. d) $hi_{R36(SIR)}$ for average hi and e) $hi_{QR(SIR)}$ for average hi.

Sensor	POLA (10^3 km^2)	avg. hi (m)
a) AVHRR (20.00 UTC) (Fig. 2.7a)		
Thermal ice thickness $hi_{TH} < 0.5$ m	11.4	0.1
Thermal ice thickness $hi_{TH} > 0.5$ m	10.23	0.07
b) SSM/I (daily avg.)		
PSSM_{12}^{085}	4.9	
hi_{R37}		0.04
hi_{R85}		0.03
PSSM_{12}^{070}	10.5	
hi_{R37}		0.05
hi_{R85} (Fig. 2.7b)		0.06
c) AMSRE (21.24 UTC)		
PSSM_{5}^{085}	7.7	
hi_{R36}		0.03
hi_{R89}		0.05
PSSM_{5}^{070}	10.34	
hi_{R36} (Fig. 2.7c)		0.03
hi_{R89} (Fig. 2.7d)		0.07
d) AMSR SIR (UTC noon)		
$hi_{R36(SIR)}$ (Fig. 2.7e)		0.08
e) QuikSCAT SIR (daily values)		
$hi_{QR(SIR)}$ (Fig. 2.7f)		0.07

3

Paper 2: Evaluation of a polynya flux model by means of thermal infrared satellite estimates

Publication, *Annals of Glaciology*, in press

Thomas Krumpen[1], Sascha Willmes[2], Miguel Angel Morales Maqueda[3], Christian Haas[4], Jens A. Hölemann[5], Rüdiger Gerdes[1], and David Schröder[2]

[1]Alfred Wegener Institute, Dept. of Sea Ice Physics, Busse Str. 24, 27570 Bremerhaven, Germany

[2]University of Trier, Dept. of Environmental Meteorology, Behringstr. 21, D-54286 Trier, Germany

[3]National Oceanography Centre, 6 Brownlow Str., Liverpool L3 5DA, UK.

[4]University of Alberta, Dept. of Earth & Atmospheric Sciences, Edmonton, Alberta, Canada

[5]Alfred Wegener Institute, Dept. of Observational Oceanography , Am Handelshafen 12, 27570 Bremerhaven, Germany

Abstract

Here we test the ability of a two-dimensional flux model to simulate polynya events with narrow open water zones by comparing model results to ice thickness and ice production estimates derived from thermal infrared MODIS observations in conjunction with an atmospheric dataset. Given a polynya boundary and an atmospheric dataset, the model correctly reproduces the shape of an 11 day-long event, using only a few simple conservation laws. Ice production is slightly overestimated by the model, owing to an underestimated ice thickness. We achieved best model results with the consolidation thickness parameterization developed by Biggs and others (2000). Observed regional discrepancies between model and satellite estimates might be a consequence of the missing representation of the dynamic of the thin ice thickening like rafting. We conclude that this simplified polynya model is a valuable tool for studying polynya dynamics and estimating associated fluxes of single polynya events.

3.1 Introduction

Wind-driven flaw polynyas are nonlinear-shaped regions of open-water and thin ice within a closed ice cover, formed by offshore winds advecting the pack ice away from fast ice edges (Smith and others, 1990). In flaw polynyas, large amounts of ice are generated and salt is expelled into the underlying waters (e.g. Renfrew and others, 2002). As Arctic sea ice volume shrinks rapidly (Haas and others, 2008; Kwok and others, 2009), the monitoring of ice production within Arctic polynyas with satellites and models is a crucial objective of ongoing polar research.

Passive microwave satellites allow for a direct deduction of polynya area, and together with atmospheric data, a retrieval of thin ice thickness and ice production. With their global coverage and their ability to penetrate cloud cover, passive microwave sensors can be used for long-term and large-scale monitoring of polynya dynamics and associated ice formation (e.g. Kern, 2009 and Willmes and others, 2010a). Unfortunately, the accuracy of the retrieval method depends on regional particularities of polynya size and shape. The coarse spatial resolution of passive microwave satellite data, if applied to narrow polynyas, generates errors through mixed signals at the fast and pack ice edges (Willmes and others, 2010b), and results in an underestimation of ice production.

Thus, monitoring of ice production in narrow leads and polynyas remains difficult with satellites alone. This gap may be filled by flux models capable of simulating polynya evolution and ice fluxes. Flux balance models were first formulated by Pease (1987), embracing the idea of Lebedev (1968) that wind-generated polynyas attain a maximum size resulting from a balance between the flux of frazil ice produced in the open water area and the wind-driven offshore divergence of consolidated new ice. If fluxes are not in balance, the polynya area is evolving.

Questions still remain as to the consistency and accuracy of flux model assessments. Markus and Burns (1995) found that the area of a polynya retrieved from passive microwave data agreed reasonably well with area estimates made by a one-dimensional polynya flux model. Haarpaintner and others (2001) and Skogseth and others (2004), who compared flux simulations in the Storfjorden polynya with ice area and ice drift information obtained from Synthetic Aperture Radar (SAR) images, confirmed these good agreements. The estimation of ice and salt fluxes in polynyas requires, besides correct representation of the polynya extent, an accurate determination of ice growth in both open water and thin ice zones. However, a direct comparison of ice production estimates made by flux models with satellite-based approximations is

still missing.

The aim of this paper is therefore to test whether flux models provide realistic ice production estimates and consequently are capable of filling the gap in narrow lead and polynya ice production monitoring.

Below we apply a two-dimensional flux model developed by Morales Maqueda and Willmott (2000) to simulate ice production of an 11 day polynya event that took place in the southern Laptev Sea in late December 2007. Model results are compared to ice thickness and ice production estimates calculated using high-resolution thermal infrared satellite data obtained from the Moderate Resolution Imaging Sensor (MODIS) in conjunction with an atmospheric dataset (Riggs and others, 2003; Yu and Lindsay, 2003). The approach is limited to clear sky conditions, but yields good results for ice thicknesses below 0.5 m (Willmes and others, 2010b). Based on the comparison, we will evaluate model applicability and identify mechanisms in the model that are fairly well represented or require further adjustments.

The paper is structured as follows: We first describe the model and dataset used for comparison (section 2). In section 3 we link simulations to satellite estimates. Model results are discussed in section 4. A conclusion is drawn in section 5.

3.2 Material and methods

Below, we briefly introduce the concept of the two-dimensional time-depended polynya flux model, the methodology to derive ice production from thermal infrared satellite data and the applied atmospheric dataset. The polynya event was chosen based on MODIS and Environmental Satellite (ENVISAT) SAR observations. In late December 2007, 11 days of offshore winds and low temperatures led to the formation of a wide coastal polynya, located directly north of the Lena Delta: the Anabar-Lena polynya. Fast ice and pack ice edges, and the polynya area are easily identifiable in SAR images in Figure (3.1). The ENVISAT C-band wide swath data is VV-polarized and covers an area of approximately 400 × 800 km^2 with a spatial resolution of 150 × 150 m^2. According to SAR observations, the thin ice formed during 11 days of offshore winds covers an area of approximately 3.5 % of the entire Laptev Sea. Because relatively calm wind conditions combined with low air temperatures limited the development of large open-water areas, passive microwave sea ice concentration data reveals no or only minor polynya activity.

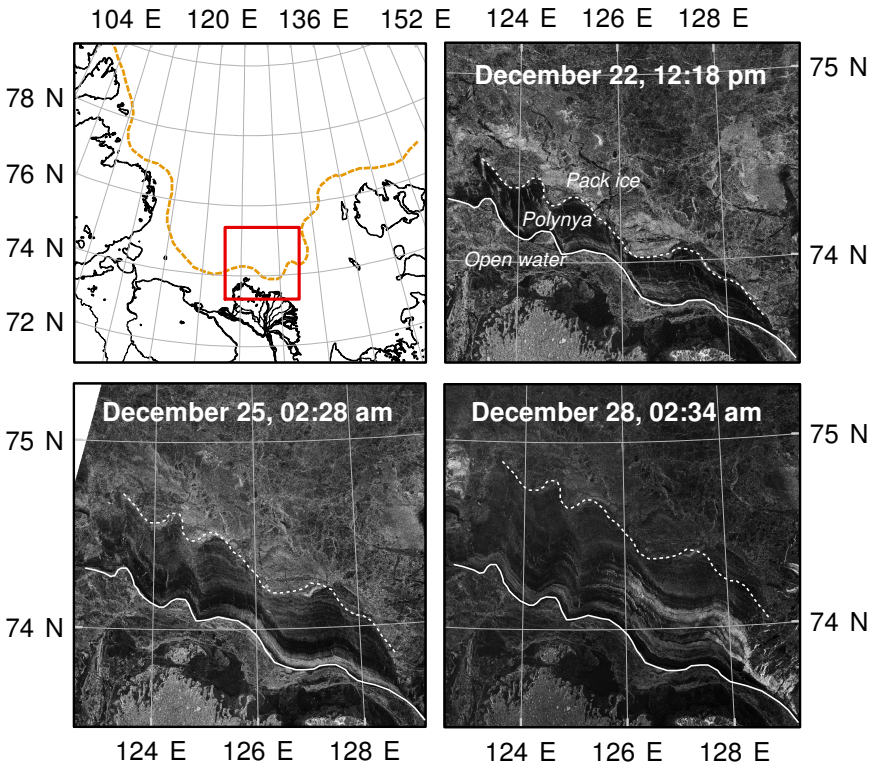

Figure 3.1: The upper left panel shows the Laptev Sea and mean recurrent coastal polynya locations (orange line). The red box represents the footprint of three ENVISAT SAR images, shown in the upper right, lower left and lower right panels. The scenes were acquired between December 21 and December 28, 2007, and cover the position of the Anabar-Lena polynya, showing the fast ice belt (south of white line), the active polynya zone and a region of freely floating pack ice (north of dashed white line).

3.2.1 Model description

The applied two-dimensional flux model was developed by Morales Maqueda and Willmott (2000) to simulate the location and temporal evolution of wind-driven polynyas. This model builds upon earlier one-dimensional unsteady and two-dimensional steady theories (Pease, 1987; Darby and others, 1994, 1995; Willmott and others, 1997).

The model distinguishes between two regions in a wind-driven polynya (Fig. 3.2). Region 1 is the area of open water where frazil ice is formed. Region 2 is the thin ice area. This latter region starts where the frazil ice, arriving from region 1, consolidates to a new ice layer and ends at the first year ice pack. The term polynya includes both the open water area and the thin ice zone. The boundary between region 1 and region 2 will be termed 'open water edge'.

The open water edge is represented by a curve $C(\mathbf{R}, t) = 0$, where $\mathbf{R}$ is the position vector of a

point on the open water edge. From Morales Maqueda and Willmott (2000) the evolution of the point **R** is determined by

$$\frac{\partial \mathbf{R}}{\partial t} = \frac{H\mathbf{U} - h_c\mathbf{u}}{H - h_c}, \tag{3.1}$$

where h_c and **u** are the thickness and velocity of frazil ice arriving at the edge C. H is the thickness of the consolidated ice formed when the frazil ice 'piles up' against C, while **U** is the drift velocity of the consolidated new ice.
According to Morales Maqueda and Willmott (2000) the evolution of H, **U**, h_c and **u** is determined as follows:

When the wind is blowing offshore, the pack ice drifts away from the fast ice edge and open water is formed. Within the open water zone, frazil ice formation takes place. The frazil ice production in the open water area is calculated following Martin and Kauffman (1981) by

$$\partial h/\partial t = \frac{-Q_{net}}{\rho_f L_s}. \tag{3.2}$$

ρ_f in Equation (3.2) is the frazil ice density of 950 kg m^3 (Martin and Kauffman, 1981) and L_s = 234.14 kJ kg^{-1} is the latent heat of fusion for sea ice (Yen and others, 1991). The surface heat balance Q_{net} can be decomposed as

$$Q_s + Q_l + Q_{lw} + (1-\alpha)\, Q_{sw} = Q_{net}, \tag{3.3}$$

where Q_s and Q_l are the turbulent sensible and latent heat fluxes calculated using a bulk parameterization with a transfer coefficient of 2.0×10^{-3} (Morales Maqueda and others, 2004), Q_{lw} is the net longwave radiation of the sea surface, Q_{sw} is the shortwave solar radiation and α is the surface albedo (e.g. Cavalieri and Martin, 1994 and Morales Maqueda and others, 2004). If Q_{net} is negative, the water body emits heat to the atmosphere and frazil ice is produced. In late December, the incoming solar radiation and the heat flux due to precipitation can be neglected. The atmospheric forcing is assumed to be uniform over region 1 and region 2.

After formation, Langmuir circulation, created by the interaction of the waves with the wind stress, herds frazil ice into slurries taking the form of long bands or plumes. Wind pushes the long bands of grease ice downwind (Pease, 1987; Martin, 2001). The velocity **u** of the frazil ice drift is determined following Martin and Kauffman (1981). The effect of surface currents on the frazil ice drift trajectories is neglected.

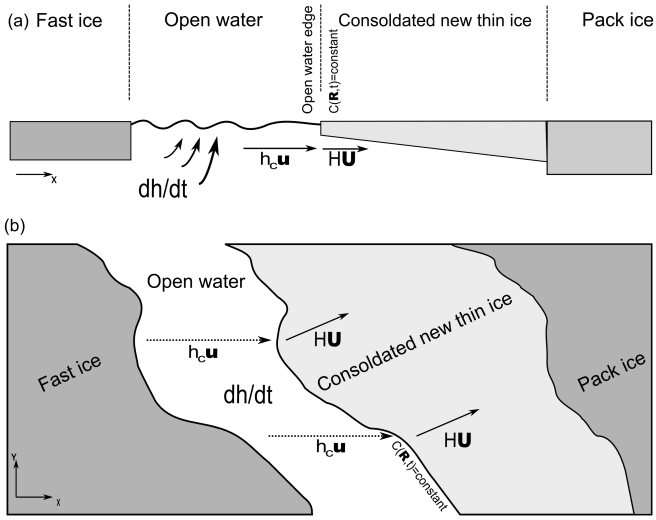

Figure 3.2: Schematic drawing illustrating the polynya model in the one-dimensional (a) and two-dimensional (b) cases (adapted from Willmott and others (1997)). In the open water area frazil ice growths with rate $\partial h/\partial t$, and is then herded downwind with speed $\mathbf{u}$, until it arrives with thickness h_c at the open water edge, $C(\mathbf{R}, t)$ = constant. Here it piles up to a thickness H, and then drifts as consolidated ice away from the edge with speed $\mathbf{U}$.

At the open water edge, h_c consolidates to a thin ice layer with thickness H. In this study, we apply the parameterization for H developed by Biggs and others (2000) to avoid situations where h_c becomes larger than H. Following Biggs and others (2000), H is derived in terms of the depth of frazil ice arriving at C and the component, normal to C, of the frazil ice velocity relative to the velocity of the consolidated new ice.

After consolidation, the continuous thermodynamic growth of new ice formed is calculated by Stefan's law (Maykut, 1986; Petrich and Eicken, 2010). Through some simplifications, the so called degree day model is capable of estimating a fairly accurate prediction of sea ice growth. The drift of the new ice is determined by Zubov's law (Leppaeranta, 2005). The occurrence of rafting inside the thin ice area is not taken into account.

For a comprehensive description of the model and numerical methods employed we refer the reader to Morales Maqueda and Willmott (2000) and Willmott and others (2007).

3.2.2 Thermal infrared satellite data

We use Level 1B calibrated radiances (thermal infrared) from the MODIS sensor, provided by the U.S. National Aeronautics and Space Agency (NASA) Level 1 and Atmosphere Archive and Distribution System (LAADS) to derive ice surface temperatures from brightness temperatures at 11 μm and 12 μm (MODIS channels 31 and 32, respectively, (Riggs and others, 2003)). The

spatial resolution of the sensor is approximately 1 × 1 km^2. The MODIS cloud mask (MOD35) product is used at the 'confident clear' level to determine clear-sky regions and to avoid a potential temperature bias due to sea smoke.

Following Yu and Lindsay (2003), the thermal thin ice thickness h_{th} is inferred from the obtained ice surface temperatures T_s by

$$h_{th} = k_i(T_s - T_o)/Q_{net}, \tag{3.4}$$

where T_o = -1.86 °C is the seawater temperature at freezing point and k_i = 2.03 W m^{-1} K^{-1} is the thermal conductivity of sea ice (Drucker and others, 2003). Q_{net} is calculated from Equation (3.3), with same parameterizations as used for the model. The thickness retrieval is based on the assumption that the heat flux through the ice equals the total atmospheric heat flux. The method implies that vertical temperature profiles within the ice are linear and no snow is present on top. It yields good results for ice thicknesses below 0.5 m, for which its accuracy is estimated to be ± 20 % (Drucker and others, 2003).

In total, we identified 67 MODIS scenes, covering the Anabar-Lena polynya between December 20 and December 30, 2007. The time of interest is characterized by very low cloud coverage and the absence of snowfall, such that surface temperature composites could be assembled on a daily basis, except for December 29.

Assuming that surface heat loss is entirely used for ice formation, the ice production for ice thinner than 0.5 m is determined by equation

$$\partial h_{th}/\partial t = \frac{-Q_{net}}{\rho_i L_s}, \tag{3.5}$$

where ρ_i = 920 kg m^3 is the density of thin ice. For a detailed description on ice thickness retrieval from surface temperature information we refer to Willmes and others (2010b).

3.2.3 Atmospheric data

Model and MODIS computations are based on 6-hourly analysis data from the global numerical weather prediction model of the German Weather Service GME (Majewski and others, 2002). Mean sea level pressure, 2 m air temperature and humidity and 10 m wind vector were extracted from a single grid point in the centre of the polynya (Fig. 3.3). The applicability of the analyzed data is shown by a comparison with automatic weather stations (Schroeder and others, 2010).

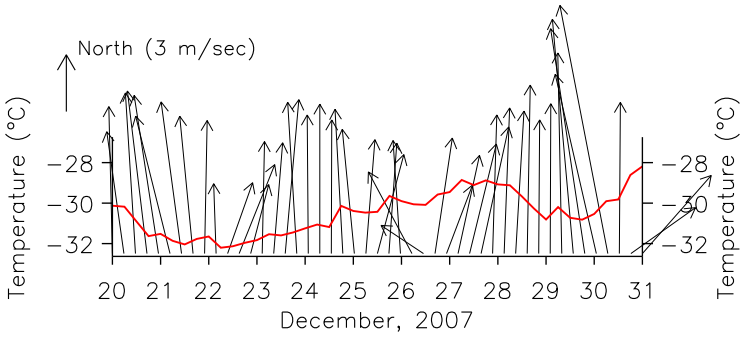

Figure 3.3: 2 m air temperatures and 10 m wind vectors during study period taken from atmospheric dataset. Wind vectors show the direction of air flow, with their lengths representing wind speed.

3.3 Results

The evolution of open water and thin ice, and associated ice production was simulated with the polynya flux model. Model results were interpolated to a grid with a spacing equal to the spatial resolution of the MODIS sensor. The drift algorithm for consolidated ice (Zubov's law) requires the ice drift deviation angle from the wind direction and ice drift velocity in percent of wind velocity to be known. These constants were taken from SAR images (Haarpaintner and others, 2001). The model boundary is the fast ice edge. Broken fast ice pieces at the polynya edge hamper comparison of model results with MODIS thermal estimates. Hence, we restrict comparison to the 100 km wide polynya centre covered solely by thin ice. The area is located between 124° E and 127° E. The method to infer thermal infrared thickness and production is restricted to ice thinner than 0.5 m. We therefore limit the model evaluation to this thermal range (0 - 0.5 m). Model thicknesses and resultant ice production exceeding 0.5 m are excluded from comparison. Note that for December 29 a MODIS composite is not available. For this particular date, we interpolate between satellite approximations made on December 28 and December 30.

Figure (3.4) shows flux model results and satellite estimates for December 25. Polynya ice thickness distribution and ice production were computed from MODIS data and model results. A SAR image, taken on December 25 at 02 a.m. UTC shows the areal extent of the polynya (compare Fig. 3.1). The banded zones of high and low backscatter in between fast ice edge and pack ice correspond to young ice, formed between December 20 and December 25. Partially, these patterns are preserved in thermal MODIS ice thickness information. The mean thickness for the polynya area below 0.5 m is 0.32 m with minimum ice thicknesses of 0.04 m. The ice area adjacent to the pack ice edge (compare SAR scene) is thicker than 0.5 m, and consequently not

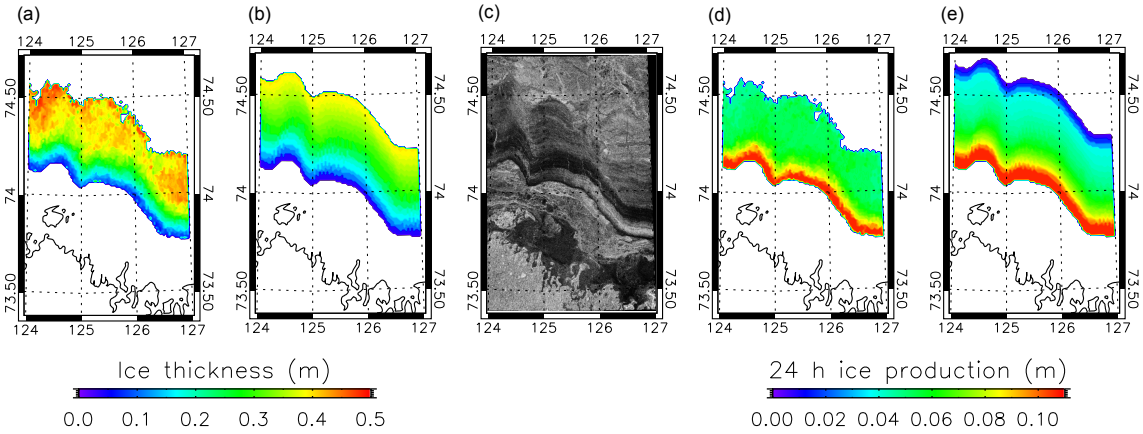

Figure 3.4: Polynya flux model results and satellite estimates for December 25. (a) and (b) represent ice thickness distribution inside the thin ice area, from MODIS approximations and model, respectively. (c) shows a SAR scene, taken at 02 a.m. UTC. (d) and (e) show satellite-based and modelled daily ice volume production.

included in the thermal approach. The mean model polynya thickness is lower (0.27 m), and the maximum thickness does not exceed 0.4 m. According to Figure (3.4) the agreement between MODIS and model ice production is high and the shape of the polynya is well resolved by the model. Note that the opening event is not visible in sea ice concentration data derived from the Advanced Microwave Scanning Radiometer (AMSR-E).

Below, we compare satellite and model polynya area evolution, thickness distribution and ice production rates for ice thinner than 0.5 m.

The polynya area evolution, as retrieved from model, MODIS and ENVISAT SAR estimates, is presented in Figure (3.5). The thermal and model area estimates show the evolution of ice areas thinner than 0.5 m. In contrast, SAR area estimates include, based on a visual image segmentation, the entire thin ice area formed between fast ice and pack ice edge during 11 days of

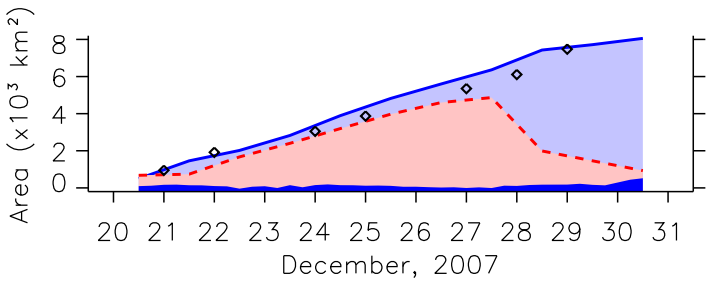

Figure 3.5: Total polynya area (light-blue shaded) and open water fraction (blue shaded) calculated with the flux model. MODIS based polynya area estimates are presented in the red shaded area. Diamonds show area information taken from ENVISAT SAR images.

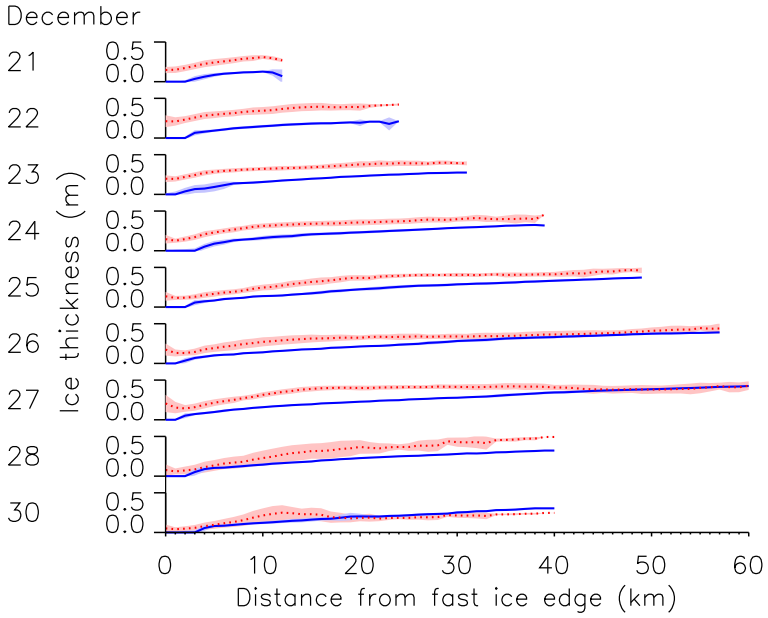

Figure 3.6: Zonally averaged polynya ice thickness distribution (m) as a function of distance from fast ice edge (km) for 9 days of polynya activity. The red dotted line represents MODIS thermal ice thickness and the blue solid line flux model estimations. Corresponding shaded areas indicate one standard deviation from mean thickness.

polynya activity (compare Fig 3.1).

According to the last SAR image available prior to the end of the observation period, the polynya reaches an area of approximately 7.9×10^3 km^2. This corresponds to an average opening width of 87 km. During the first 8 days of offshore winds (compare Fig. 3.3), polynya area is continuously increasing regardless of the methodology used for area calculation. MODIS area approximations are slightly lower than SAR area estimates, since the thickness of thin ice close to the pack ice edge is beyond the limit of the thermal ice thickness retrieval. Ice growth beyond 0.5 m also causes the sharp drop in MODIS area from 4.8×10^3 km^2 down to 1.1×10^3 km^2 between December 28 and December 30. Model thin ice areas exceed ice thicknesses of 0.5 m only at the very end of the observation period. Hence, the model area closely follows SAR area estimates.

A direct comparison of the computed open water area with satellite approximations is not possible, since reliable satellite-based open water estimates are missing. In SAR images, often no clear limit exists between open water and consolidated thin ice, due to the smooth transition from low to high frazil ice concentration. MODIS based open water estimates suffer from mixed pixel signatures. Following Equation (3.4) open water areas are characterized by a surface temperature close to the freezing point of seawater. Unfortunately, the presence of frazil ice, Lang-

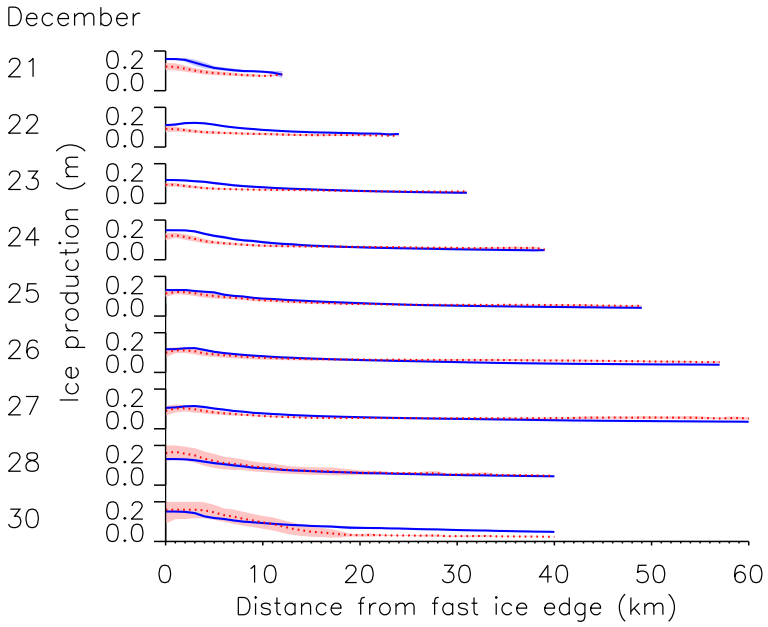

Figure 3.7: Zonally averaged 24 h ice volume production (m) as a function of distance from fast ice edge (km) for 9 days of polynya activity. The red dotted line corresponds to ice production as derived from MODIS. The blue solid line represents flux model estimations. Corresponding shaded areas indicate one standard deviation from mean thickness.

muir streaks or ice floes in the water column lowers the averaged surface temperature within the sensor footprint beneath freezing point, such that potential open water areas are classified as very thin ice.

Figure (3.6) shows the zonally averaged ice thickness profile across the polynya and its standard deviation, computed from MODIS composites and model results for 9 days of polynya activity. Both MODIS and model show an increase in ice thickness with increasing distance from the fast ice edge. The simulated ice thickness tends to be generally lower than thermal ice thickness. Standard deviations are higher for thermal ice thicknesses than for model thickness.

Nearby the fast ice edge, the model shows a small strip of open water with ice thickness equal to 0. Within this zone, ice growth in the model takes place as frazil ice formation, which is herded offshore until it consolidates at the open water edge. Following the parameterization developed by Biggs and others (2000), the consolidation thickness varies between 0.06 m (December 27) and 0.15 m (December 25). After consolidation, the ice thickness in the model is governed by thermodynamic processes as described by Stefan's law (Petrich and Eicken, 2010).

The MODIS sensor does not show open water zones. Instead, the zone close to the fast ice edge is characterized by very low thicknesses varying between 0.06 m (December 30) and 0.20 m

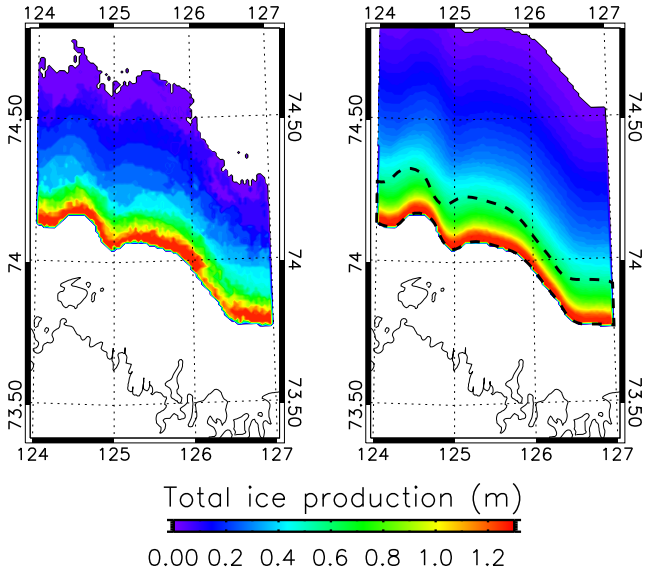

Figure 3.8: Total amount of ice produced (m) within 11 days of polynya activity (December 20 - December 30, 2007). Left panel: Ice production based on MODIS thermal infrared data. Right panel: Model simulated ice production. In the area near the fast ice edge the accumulated ice production amounts to 1.3 m (MODIS) and 1.2 m (flux model), respectively. The dashed black line shows the extent of the mask area applied in Figure (3.9).

(December 22). With increasing distance from the fast ice edge, the difference in MODIS and model estimates is decreasing, except for December 21 and December 22.

Figure (3.7) shows the zonally averaged ice production across the polynya computed from MODIS and model results. Modelled ice production agrees well with MODIS estimates. At the fast ice edge, highest ice production rates are achieved, either in the form of frazil ice production (model), or by means of conductive heat flux through very thin ice (MODIS, compare Fig. 3.6). Ice production is then decreasing with distance from the fast ice edge, owing to the increasing ice thickness. Largest deviations in MODIS and model ice production estimates occur 0 to 10 km offshore the fast ice edge.

The accumulated total ice production over 11 days in the entire polynya area is presented in Figure 3.8. Because modelled ice thickness exceeds 0.5 m only at the end of the observation period, its ice production area extends far north (see also Fig. 3.5). MODIS and the flux model calculate the accumulated ice production per km^2 in the area near the fast ice edge to be 1.3 m and 1.2 m, respectively. Beyond the fast ice edge region, ice formation rates are higher in the model, which results from lower ice thickness estimates (Fig. 3.6). The mean accumulated ice production per km^2 is 0.4 m and 0.37 m, for MODIS and model respectively. The satellite observed characteristics of ice production are well captured by the model.

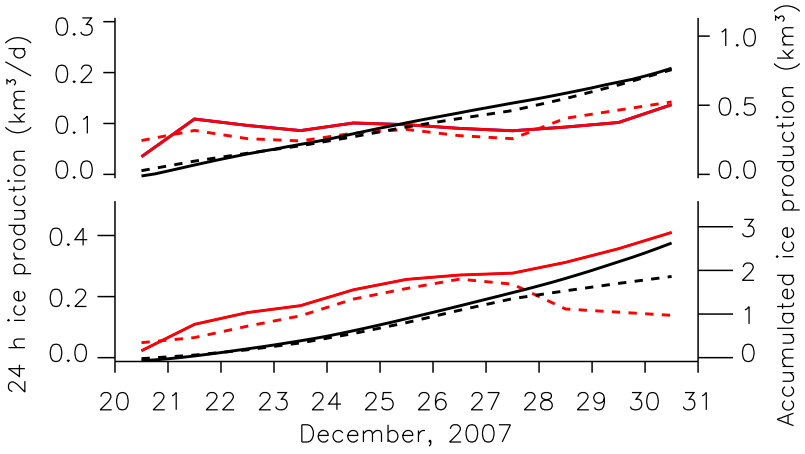

Figure 3.9: MODIS and model mean daily and accumulated total ice production between December 20 and December 30. Upper panel: Mean daily and accumulated total ice production within a predefined 900 km^2 big area offshore the fast ice edge (mask area is shown in Fig. 3.8). Modelled and thermal mean daily ice production (km^3/d) are represented by the solid red and dashed red line, respectively (left axis). Modelled and thermal accumulated total ice production (km^3/d) is represented by the solid black and dashed black line (right axis). Lower panel: Mean and accumulated total ice production for the entire polynya area. The color and line code are the same as in the upper panel.

Figure (3.9) presents the MODIS and model mean daily and accumulated total ice production. Calculations in the upper panel are limited to an area of 900 km^2 adjacent to the fast ice edge. This area includes open water and parts of the thin ice zone. The extent of the mask area is drawn in Figure (3.8) and is equivalent to the polynya area 1.5 days after opening. During the first 8 days, the modelled mean daily and accumulated total production slightly exceeds MODIS estimates. However, an increase in MODIS ice production on December 28 and December 30, causes the accumulated ice volumes to equal towards the end of the observation period. The total ice production inside the mask area amounts to 0.9 km^3.

In the lower panel, all ice areas thinner than 0.5 m were taken into account for volume approximations. Again, in the beginning the model shows a higher daily mean production, until, on December 28, the MODIS polynya area is decreasing owing to an increase in ice thickness beyond 0.5 m (compare Fig. 3.5). As a consequence, modelled daily ice production becomes twice as high as MODIS estimates, resulting in a 30 % higher total ice volume.

3.4 Discussion

The determination of the open water edge is a central element in the model concept. Unfortunately, the reliability of the modelled open water width is difficult to assess directly, since

for the prescribed situation satellite-based open water width estimates are missing. This is because the identification of open water in SAR and MODIS scenes is hampered by the narrowness of the open water zone and the presence of frazil ice in the water column.

Nevertheless, since ice production rates are highest inside the open water area, the spatial distribution of highly productive zones gives evidence for the extent of open water. Consequently, the achieved accuracy of the open water simulation can be determined through a comparison of satellite-based estimates with modelled zones of high ice growth rates. Moreover, a good agreement between modelled and thermal ice thickness distribution is a second indication for model reliability.

An initial comparison of thermal infrared ice thickness and production estimates with model computations has shown that the flux model is capable of reproducing quite well the shape of the polynya and salient features of the landfast ice boundary.

Note that the equations to derive ice thickness and ice production from MODIS are, by definition, very close to the equations that are used in the model. In addition, the applied atmospheric forcing is identical. Hence, the accuracy of the simulation primary depends on if a realistic fast ice boundary is used and if the movement of the pack ice edge is prescribed correctly (by estimating appropriate parameters for Zubov's law from SAR images). Another well-known uncertainty in polynya simulations is the parameterization of the collection depth H, since the evolution of the open water edge is extremely sensitive to it. Early one-dimensional and two-dimensional polynya flux models have used constant values for H, typically between 0.02 and 0.3 m (e.g. Martin and Kauffman, 1981; Pease, 1987; Haarpaintner and others, 2001), chosen by fitting flux model results to the observed widths of the open-water zone. Winsor and Bjoerk (2000) assume H to be a linear function of the 10 m wind speed, increasing from 0.1 to 0.3 m as the wind speed increases from 5 to 35 m s^{-1}. Biggs and others (2000) developed a parameterization to avoid situations where the thickness of frazil ice arriving at the polynya edge becomes larger than H. All different parameterizations for H were tested in the model and results were compared to satellite approximations (not shown here). For the event investigated in this paper, we found that the parameterization developed by Biggs and others (2000) yields the most realistic open water extent. Parameterizations using constant H are either numerically unstable or lead to a crude overestimation in open water area.

Furthermore, regional differences between satellite estimates and model results are related to the representation of physical processes in the model and possible deficiencies in the atmospheric datasets. Below, we discuss parameterizations and mechanisms that are fairly well rep-

resented or require further adjustments.

Because the GME dataset is spatially quite uniform, we use atmospheric forcing fields extracted from a single grid point in the centre of the polynya. The mean deviation in longshore wind velocity from the polynya centre is 0.4 ± 0.21 m sec^{-1}. The average longshore differences in wind direction and temperature are $4.4 \pm 3.1°$ and 0.34 ± 0.32°C, respectively. The resultant uncertainty in heat flux computations is 35 ± 30 W m^{-2}, which is equivalent to a frazil ice production error of 1.1 ± 0.009 m m^{-2} d^{-1}. However, in reality strong gradients of air temperature and wind speed across and along the polynya may exist which are not captured by the GME dataset and which may lead to uncertainties in ice production estimates. Furthermore, in the atmospheric GME model polynyas are not present, thus the 2 m air temperatures are valid over thin ice only. Following Ebner and others (2010), 2 m air temperatures over open water can be significantly higher than over the ice. This may result in an overestimation of both model and satellite-based ice production.

Some physical processes that do have an impact on the formation and maintenance of the polynya are not considered in the model. There is evidence that frazil ice trajectories are affected by ocean currents (Willmott and others, 1997). In the flux model, we assume frazil ice motion to be purely wind driven, since the strength and direction of near surface currents are unknown. In addition, inertial motions and tidal currents might advect warmer water from outside into the polynya area, thus hindering frazil ice production (Willmott and others, 2007). The error associated with this uncertainty is unknown.

The simplifications made in the model become increasingly important as the open water region grows in size. In our case, the simulated polynya develops under moderate wind speeds and low air temperatures, such that the open water area stays relatively small. If the open water width becomes wider, which is the case for polynya events in the Laptev Sea taking place in late April (Willmes and others, 2010a), spatial variations in atmospheric and oceanic forcing would significantly alter frazil ice motion.

Beside the parameterization of H, discrepancies between satellite estimates and model can also be a consequence of the incomplete, or missing, representation of dynamic processes taking place inside the thin ice area. According to Skogseth and others (2005), rafting and ridging in polynyas can play a significant role in ice thickening, the creation of open water area and ice production. Rafting and ridging primarily result from a compression of the thin ice zone, owing to differences between the drift of the outer pack ice and the evolution of the open water edge.

During the opening of the Anabar-Lena polynya, we assume compression to result exclusively

in rafting. This assumption is supported by aerial photographs taken on winter expeditions in the Laptev Sea during different flights across active polynyas (TRANSDRIFT XIII, TRANSDRIFT XV). The aerial images show that the occurrence of rafting increases with distance from the fast ice. This is because, at the onset of an opening event, when the thin ice zone is rather small, compression operates on a relatively small thin ice area leading to high rafting rates. With increasing thin ice width, the rafting probability weakens. This possibly explains the decrease in discrepancies between satellite approximations and model results towards the end of the observation period. To account for rafting in the model, one could simulate the evolution of the outer pack ice and open water edge separately and take the difference between drifts as a measure of compression acting on the thin ice zone. Nevertheless, an implementation of a dynamic thickening component is difficult, since studies on rafting probabilities in thin ice zones are limited to characterizations of processes such as energy consumption (Worby and others, 1996; Babko and others, 2002).

The spatial and quantitative agreement between modelled and satellite-based total ice volume production is high (Fig. 3.8). The largest deviations in ice production estimates coincide with areas of high disparity between simulated and thermal infrared thickness (compare Fig. 3.6, Fig. 3.7 and Fig. 3.9). If we limit satellite and model comparison to the highly productive zone close to the fast ice edge (masked area in Fig. 3.8 and upper panel of Fig. 3.9), differences in ice volume calculations are even smaller. Taking into account the entire polynya area (lower panel Fig. 3.9), the model overestimates ice production by 30 %. This is due to the differences in simulated and satellite-based polynya area estimates (Fig. 3.5), which is again, a consequence of the underestimated model ice thickness.

3.5 Conclusion

We have compared two commonly used approaches to estimate ice production by applying them to an observed Laptev Sea polynya event. A two-dimensional flux model developed by Morales Maqueda and Willmott (2000) is used to calculate the location of transition between open water and thin ice, the drift of consolidated new ice and associated ice formation. Results from this model are in agreement with ice thickness and production estimates obtained from MODIS thermal infrared data in conjunction with an atmospheric dataset.

Given a polynya boundary (coastline or fast ice edge) and an atmospheric dataset, the model is capable of describing the shape of the polynya realistically using only a few simple conservation laws. The mean accumulated ice productions unit area for 11 days of polynya activity are

0.4 m and 0.37 m for thermal and model estimates, respectively. The accumulated ice productions in the area near the fast ice edge amount to 1.3 m and 1.2 m, respectively. Further offshore, ice formation rates are overestimated by the model, owing to the fact that it underestimates the ice thickness.

We conclude that this simplified physical polynya model is a valuable tool for studying polynya dynamics and estimating associated fluxes of single polynya events. It provides an alternative to passive microwave polynya monitoring techniques, which are often not capable of resolving narrow polynyas formed under moderate or low wind forcing.

The best model results are achieved with the consolidation thickness parameterization developed by Biggs and others (2000). The implementation of dynamic thin ice thickening could eventually improve observed regional discrepancies between model and satellite. When simulating polynya events of larger longshore dimension, the use of a spatially non-uniform forcing dataset would be required. However, with increasing complexity, a purely numerical approach is needed.

3.6 Acknowledgments

This work was carried out as part of the German-Russian cooperation 'System Laptev Sea', funded by the BMBF under grant 03G0639A and the Alfred Wegener Institute. Satellite data were obtained through ESA Project EO-500 'Formation, transport and distribution of sediment-laden sea ice in the Arctic Shelf seas'. MODIS images were provided by LAADS/NASA and AMSR-E ASI sea ice concentrations by the University of Bremen, Germany. The GME analyses were made available by the German Weather Service.

4

Paper 3: HELIOS, a nadir-looking sea ice monitoring camera

Manuscript, submitted to *Cold Region Science and Technology*

Thomas Krumpen[1], Christian Haas[2], Stefan Hendricks[1], Jens A. Hölemann[3], Dirk Kalmbach[1], Rüdiger Gerdes[1]

[1]Alfred Wegener Institute, Dept. of Sea Ice Physics, Busse Str. 24, 27570 Bremerhaven, Germany
[2]University of Alberta, Dept. of Earth & Atmospheric Sciences, Edmonton, Alberta, Canada
[3]Alfred Wegener Institute, Dept. of Observational Oceanography, Am Handelshafen 12, 27570 Bremerhaven, Germany

Abstract

We present the prototype of a simplified photogrammetric system (HELicopter-borne Ice Observation System, HELIOS) and demonstrate how it can be used for the documentation of ground- and airborne sea ice surveys. The aerial unit consists of a nadir-looking digital camera mounted on a gimble, a GPS receiver and a computer. It is of low-cost and weight and is designed such that it withstands low temperatures, operates autonomously and fits to any standard helicopter skid. Systematic errors arise from the GPS-based determination of the camera position, the pointing accuracy of the gimbal, and the camera alignment in flight direction. Because most sea ice mapping projects require an accuracy far below conventional mapping standards, HELIOS offers a broad range of applications. This includes the photogrammetric documentation of experimental sites as well as the verification of satellite-, and model-based estimates of sea ice and snow cover properties. Images taken simultaneously with other airborne observations provide a valuable tool to assess the accuracy of those measurements.

4.1 Introduction

The investigation of sea ice in Arctic regions by means of aerial photography goes back until the 1940s. By that time photographs were the only remote sensing tool obtained on an operational level at high latitudes (Johannessen and others, 2005). Because practically all sea ice characteristics that are captured by the human eye can be determined on the basis of photographs as well, they were used to support navigation in Northern Sea Routes and to gain fundamental insight into principals of ice dynamics and formation (Bushuyev and others, 1964; Tucker and Govon, 1981; Hall and Rothrock, 1987).

Today, aerial photographs are no longer used on an operational basis. Since the 1980s, information on sea ice concentration and dynamics have been obtained, most reliably and over larger regions, from passive and active microwave sensors mounted on satellites or airborne platforms. In addition, the implementation of camera systems on board of aircrafts in Polar regions poses difficulties different to standard photogrammetric surveys: First, the transport of expensive photogrammetric systems demands extensive logistical efforts (Barnea and others, 2009). Second, most aircrafts that are used on Arctic surveys are helicopters without a designated shooting hole. Consequently, the heavy camera equipment needs to be placed outside the aircraft, which requires special protection and heating and limits the payload. Third, the camera operation can be complicated and time consuming.

The lack of aerial photography of sea ice was pointed out at the Climate and the Cryosphere (CliC) workshop on Arctic sea ice observations in Tromsoe, 2009. The objectives of this workshop were to develop, standardize, and implement observation and measurement protocols for Arctic sea ice in coastal, seasonal, and perennial ice zones (Perovich and Gerland, 2009). It was proposed that there is a need for better and standardized documentation of airborne and ground-based sea ice measurements. Here, aerial photographs do provide a valuable contribution. Moreover, images can be used on field campaigns and expeditions to support planning and decision making (Steer and others, 2008) as well as to validate the accuracy of model results and airborne and satellite-based estimates of sea ice and snow cover properties (Leisti and others, 2009; Krumpen and others, 2010b).

In this paper, we describe the development of a simple nadir-looking low-cost photogrammetric unit that is capable of filling the gap in experimental site documentation. The HELicopter-borne Ice Observation System (HELIOS) is designed such that it can be easily mounted on standard helicopters, withstands extreme conditions, operates autonomously and is simple to

manufacture. Our aim is to test whether the system fulfils requirements on accuracy for the documentation of ground- and airborne surveys of sea ice.

Below, we present the aerial unit, the image processing techniques and evaluate, based on data obtained during former expeditions, the precision of the system. Finally, we address and discuss several camera applications on sea ice.

4.2 The aerial unit

The presented aerial unit is based on a low-cost consumer camera. The usage of these cameras for aerial photogrammetry has been discussed for a long period among the photogrammetric community (Barnea and others, 2009). It was shown by Laebe and Foerster (2004), Petrie (2006) and Petrie and Walker (2007) that low-cost consumer cameras, under certain, limited accuracy requirements, can be succesfully implemented for photogrammetric purposes. The photogrammetric requirements in terms of accuracy and image quality for sea ice applications like the verification of satellite-, and model-based estimates are far below conventional mapping standards, since the image error is several magnitudes smaller than the spatial resolution of common model or satellite data products. Below, the system components and image processing techniques are described in detail.

Photogrammetric surveys in the Arctic environment require robust and energy efficient digital equipment. The HELIOS prototype is equipped with a rugged digital camera, the RICOH Caplio 500SE. The camera has an 8.3 megapixel sensor (7.18 x 5.32 mm CCD) and a wide angle 3 x optical zoom lens, equivalent to a focal length of 28 - 84 mm on a 35 mm film. The image quality is high, with good saturation and contrast, and there is little to no evidence of corner softness and radial distortion. The camera is enclosed in a weatherproof plastic dome, which has been designed to withstand contact with water and extreme temperatures.

To compensate for pitch and roll of the aircraft, the nadir-looking camera is fitted on a two-axis gimbal (Fig. 4.1, left panel). The camera mount contains isolation bushings, insulating the sensor from vibration. The camera and gimbal were given additional weather protection by placing the unit inside a heated plastic enclosure (0.41 x 0.41 x 0.3 m). The plastic enclosure is designed such that it fits to any standard helicopter skids (Fig. 4.1, right panel).

The RICOH camera is capable to write GPS information into the image header. Geographic positions can be taken either from an internal or external GPS device. The internal GPS receiver

Figure 4.1: (Left) RICOH® camera 500SE placed on a two-axis gimbal for tilt compensation. (Right) Photograph of HELIOS (HELicopter-borne Ice Observation System) mounted on a BELL Helicopter.

consists of a 1 Hz SiRFStar III chip. As an external receiver we are using a 4 Hz Amtel/u-blox Antaris® chip placed outside the plastic enclosure to improve GPS reception. The position accuracy of the GPS receivers were tested by comparing measurements against a reference point of known location. Results are listed in Table (4.1).

Some mapping applications like photogrammetric surveys of experimental sites require proper flight track and acquisition point planning. This can be done using a geographical information systems (GIS) or a flight management software. During flight, a GPS connected to the software shows the real-time position of the aircraft relative to the mission trail and the image acquisition points. When the acquisition point is reached, the camera is released manually by a laptop computer from inside the helicopter via a Bluetooth channel. If photographs are taken simultaneously with other airborne measurements, the system can be set such that it is released automatically with a predefined acquisition interval. Photographs taken are stored on the camera internal flash memory card. Under flight conditions, the operating-time of the battery driven system is approximately 4 hours.

Table 4.1: Accuracy of GPS receivers tested by comparing the measurements against a reference point of known location.

GPS-Chip	SiRFStar III	Amtel/u-blox Antaris
Frequency	1 Hz	4 Hz
Mean distance from reference point	± 4.4 m	± 2.9 m
STDV	± 7.2 m	± 2.2 m

4.2.1 Image processing

The fundamental task of aerial photography is to establish the geometric relationship between the image and the object as it existed at the time of the image event (Mikhail and others, 2001). Below, this process is referred to as georeferencing (Mather 1999).

To locate and orientate the image in the object coordinate system, the image center coordinates (X_0, Y_0, and Z_0), the focal length, and the three orientation parameters, pitch, roll and yaw (ω,φ,κ), are needed (Mikhail and others, 2001; Kasser and Egels, 2002; Paine and Kiser, 2003; Lillesand and others, 2004). High precision photogrammetry also requires the determination of camera interior parameters in a laboratory. However, our requirements on accuracy are comparatively low and the interior camera calibration is a cost intensive procedure. Thus, the lens geometry is neglected by assuming it to be flat-field.

X_0, Y_0, and Z_0 positions are taken from the camera internal GPS device. If using an external antenna, X_0, Y_0, and Z_0 need to be corrected for the displacement between the external GPS receiver and the camera position.

Pitch and roll of the aircraft are assumed to be fully compensated by the gimbal shown in Figure (4.1), such that ω and φ are set to 0. κ is close to the flight direction and can be computed from a GPS receiver with two antennas placed at different positions. The measurement differences taken by the two antennas enable the determination of an accurate camera orientation relative to the flight direction. Note that this method requires additional processing and filtering (Barnea and others, 2009). To keep the system as simple as possible we therefore suggest to set κ equivalent to the flight direction. Errors associated to this assumption are discussed below.

4.2.2 Qualitative system evaluation

During a Russian-German research expedition in winter 2009 (TRANSDRIFT XV), the accuracy of the camera system was tested by making 20 flights across a set of points of known location (ground control points, GCP). Flight speed was approximately 130 km/h and flight height was constant around 85 m. Image positions were taken 10 times with the external 4 Hz GPS receiver, and 10 times with the internal 1 Hz device. An image example is given in Figure (4.2).

The mean displacement of image points from the GCP's is equivalent to the X_0 and Y_0 position error induced by the use of different GPS frequencies. Image georeferencing based on a 1 Hz device results in a position mismatch of ± 60 m. The use of a 4 Hz chip significantly improves the accuracy of X_0 and Y_0 determination by 75 % to ± 15 m.

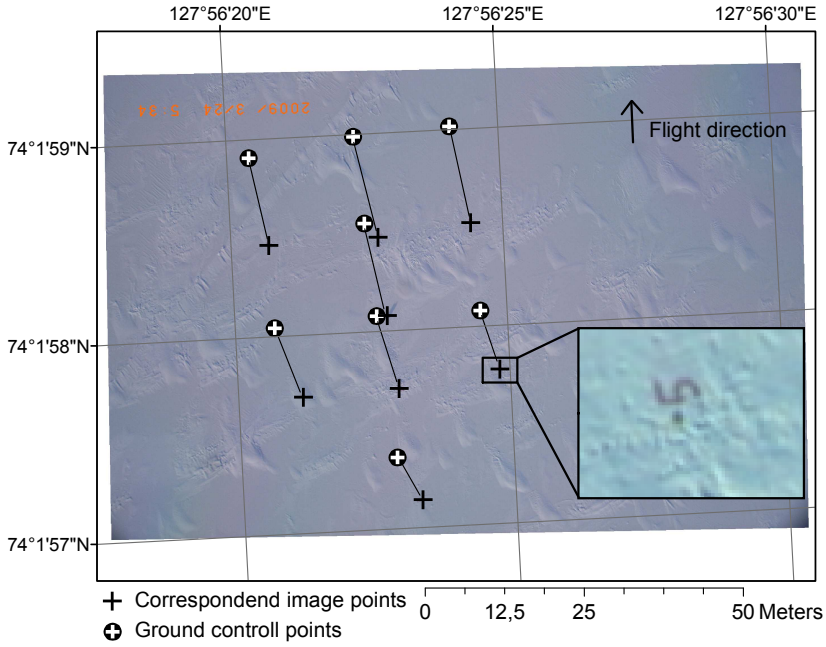

Figure 4.2: Aerial photograph taken with HELIOS on March 24, 2009 (TD XV) using a 4 Hz GPS receiver. Image was obtained at 85 m flight height and covers a footprint of 109 x 72 m. The black crosses mark ground control points (GCP) of known locations on the fast ice (see enlargement). The white crosses show the locations of corresponding image points on the georeferenced image. Displacements between image points and GCP's gives evidence for the accuracy of the system. Residuals should be of comparable size and point in random directions. A tendency in the displacement indicates the presence of a systematic error. Here, the image is tilted by an angle of 4° against flight direction (pitch, ω). The mean offset of image points from GCP's is 12 m.

Following Mikhail and others (2001), the pointing accuracy of the gimbal is calculated via the relative displacement between image points. We estimated the pointing accuracy in φ direction to be within a range of ± 1°. Thus, the pointing accuracy of the gimbal in roll direction is satisfying. Unfortunately, the camera pitch against flight direction, induced by high helicopter velocities, cannot be fully compensated by the suspension. Due to momentum, the precision of ω compensation is ± 5°.

To keep the system as simple as possible, we suggest setting yaw equivalent to the flight direction. However, an aircraft in a crosswind can have several degrees of yaw. To quantify how close yaw (κ) is to the flight direction, we compared the camera orientation recorded by a digital compass with flight direction estimates computed from the GPS track (Fig. 4.3, upper panel). The data were obtained during a crosswind flight with a Russian MI-8 helicopter (TD XV). The wind velocity during flight was approximately 6 m sec^{-1}. For the prescribed flight, the mean deviation between flight direction and camera orientation was ± 2°, which is acceptable. However,

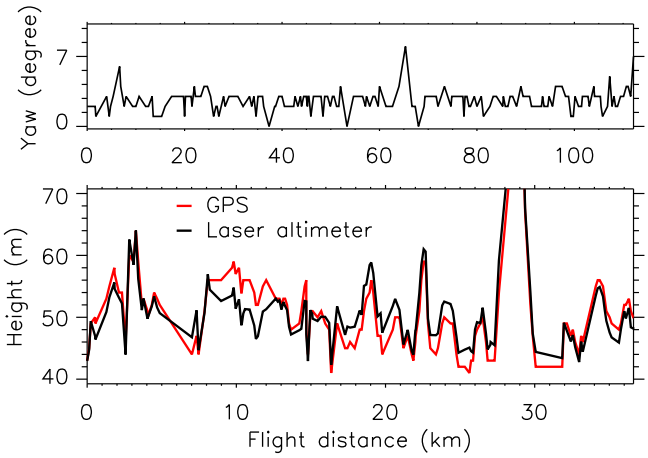

Figure 4.3: (Upper panel) Yaw (κ) error resulting from the assumption that the camera is aligned with the flight path. The error is computed from the difference between true camera orientation recorded by a digital compass and flight direction computed from the GPS track. Data was obtained during a crosswind flight with a Russian MI-8 helicopter. The wind velocity at 2 m height was approximately 6 m sec^{-1}. (Lower panel) Comparison of the camera height as obtained from the 1 Hz GPS receiver with height information taken from a laser altimeter. The difference gives evidence about the accuracy of the estimated GPS camera height. Data was obtained during a HEM flight in April, 2008 in the Laptev Sea (TD XIII).

maximum values of ± 8° can occur. Note that yaw angles might significantly differ under higher wind speeds and if using smaller helicopters.

An additional error arises from uncertainties in GPS camera height estimations. A comparison of the camera height as obtained from the 1 Hz GPS receiver with height information taken from a laser altimeter, gives evidence about the accuracy of the estimated camera height (Fig. 4.3, lower panel). If the helicopter maintains height at a constant level, the mean Z_0 positioning error is approximately ± 4 m. Data were obtained to during a helicopter-borne, electromagnetic (HEM) ice thickness measurement flight (Haas and others, 2009) in April, 2008 in the Laptev Sea (TD XIII).

The error associated to the missing interior calibration of the camera is unknown. For example, lens distortion might result in radial displacements of imaged points from their theoretically correct positions. This is the most relevant interior aberration and can directly affect the accuracy of the system. Nevertheless, aberrations related to the lens geometry are rather small compared to systematic errors introduced by the GPS and the gimbal. Hence, an interior calibration of the camera would not significantly improve the performance of the system.

4.3 System applicability for various mapping projects

Whether HELIOS can be used to document ground- and airborne sea ice surveys depends on the required accuracy of the mapping project.

An important application for aerial photography is to service short-range ship navigation of scientific groups and companies by using imagery to visually classify sea ice distribution and characteristics. For this application, requirements on geometric image accuracy are usually low and adequate results can be achieved by a hand-held camera, where the system time has been synchronized with a GPS. A trained observer can then easily separate between multiyear and first year ice, estimate the rate of compression in sea ice fields and localize potential navigation passages. Here, the advantage of a system like HELIOS merely lies in its simple autonomous operation.

Furthermore, aerial photographs can be used for the verification of satellite-, and model-based estimates of sea ice and snow cover properties (Steer and others, 2008). For this application HELIOS is suitable, as the image error is several magnitudes smaller than the spatial resolution of common model or satellite data products.

In the past, images obtained by HELIOS were successfully applied in a number of studies. For example, information taken from aerial photographs were used by Willmes and others (2010b) to contribute to the cross-validation of ice thickness estimates made by the Moderate Resolution Imaging Sensor (MODIS) and the Advanced Microwave Scanning Radiometer. They further aided interpretation of Environmental Satellite (ENVISAT) Synthetic Aperture Radar (SAR) imagery (Krumpen and others, 2010b) and TerraSAR-X scenes (Busche and others, 2009). Moreover, photographs taken during a flight across a polynya in the Laptev Sea were employed for the calibration and validation of a polynya flux model (Krumpen and others, 2010b), and to investigate the hydrographic response to ice formation (Dmitrenko and others, 2010b).

If investigating potential anchoring grounds for ships and landing strips for planes, mapping sea ice characteristics in the vicinity of experimental sites, or surveying the experimental site itself, a much higher accuracy (in an order of several meters) is needed. It was shown that this level of accuracy is archived by the camera system, if a GPS with a frequency of more than 4 Hz is used and flight conditions are relatively stable. Figure (4.4) shows a mosaic of aerial photographs taken with HELIOS over an experimental site of the Ocean Atmosphere Sea Ice Snowpack (OASIS 2009) campaign in Barrow, Alaska. According to the mismatch between registered images, the accuracy of the georeferenced photographs is around $\pm$ 8 m. Theoretically,

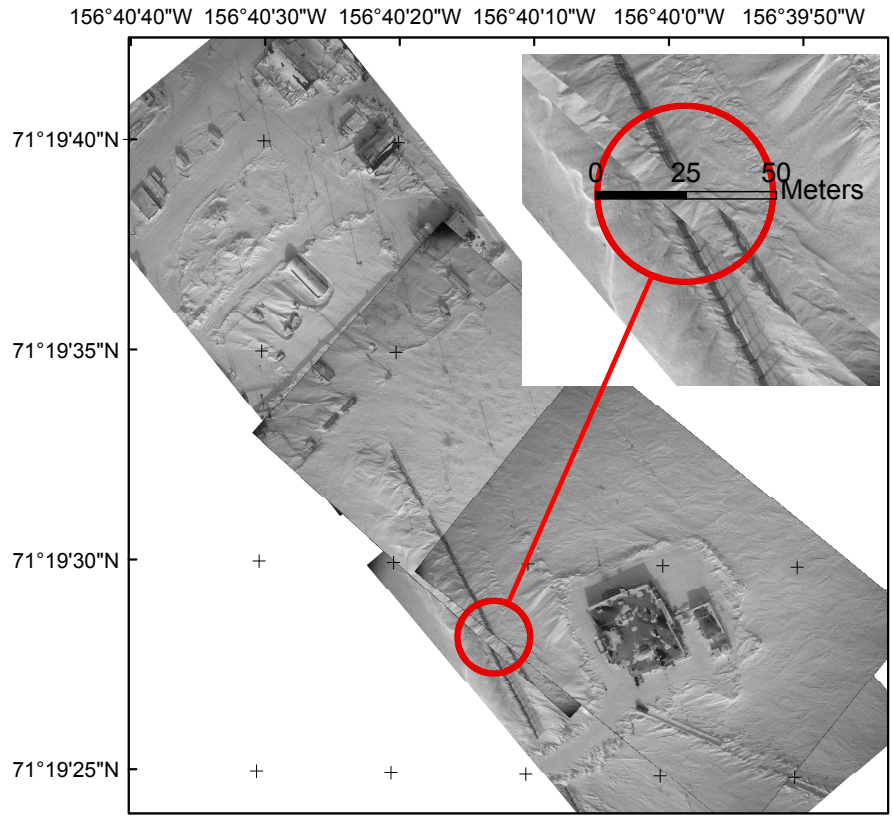

Figure 4.4: Mosaic of aerial photographs, taken during a flight over Barrow, Alaska. 2 images were obtained with a 50 % overlap heading towards North-West, and 2 photographs were taken without overlap heading towards South-East. Flight height was 250 m and flight speed was approximately 70 km/h. The mismatch between registered images gives evidence for the system accuracy (see enlargement).

the precision of the image localization and orientation can be further improved by the use of 10 Hz GPS, a GPS reference station and/or a reduction in flight speed.

Moreover, HELIOS was applied to document a number of other airborne observations. For instance, images taken simultaneously to sea ice surface temperature records made by a pyrometer were used to obtain information about the spatial distribution of open water patches, compression such as rafting or ridging, and the presence of frost flowers or snow on top of the ice. Some parameters such as ice concentration, ice type, compression and floe size can be extracted automatically from digital 8-bit, RGB (red, green, blue) images. This is done by band thresholding, simple classification methods or convolution filters. For an in-depth description and discussion of these processing techniques we refer to Weissling and others (2009).

Figure (4.5) shows a series of aerial photographs collected during the pyrometer flight across

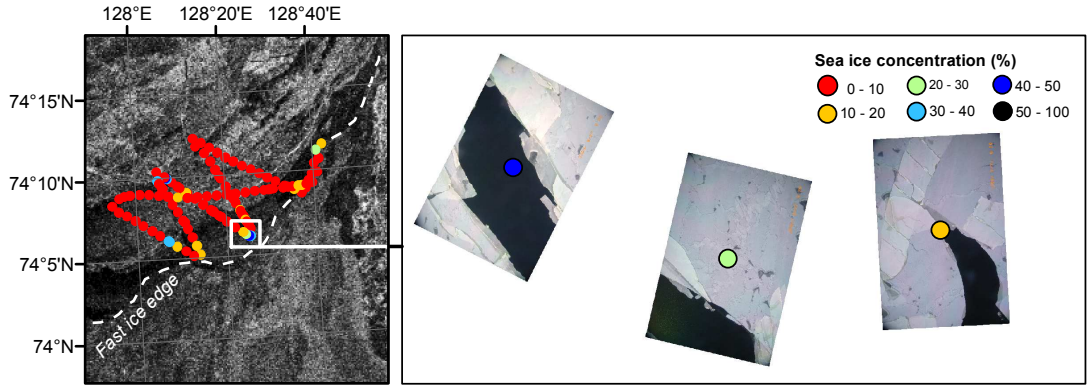

Figure 4.5: Aerial photographs taken during a flight across the Western New Siberian polynya in the Laptev Sea on March 27, 2009. The image footprints are plotted as coloured dots on top of a SAR scene, acquired approximately 1 h before the survey (left panel). The color-code corresponds to the classified fraction (%) of open water present in each image. In addition to information on sea ice concentration, photographs provide insight into ice dynamics (rafting and ridging), and the presence of frost flowers or snow on top of the ice (right panel).

an active polynya on March 27, 2009. To determine the fractions of open water in each photo, a band thresholding method is used. Note that photographs taken over water or ice without snow cover often show mirror-like reflections of light. These specular effects are caused by the relationship that exists among solar elevation, azimuth angle and camera orientation (Lillesand and others, 2004). Thus, a radiometric image enhancement needs to be done prior to segmentation. Cross- and along track variation in illumination are corrected by fitting a polynomial function of second order to the cross- and along track means.

Likewise, spatial information on rafted and unrafted ice in polynyas can be obtained from the imagery. Figure (4.7) shows a single image taken simultaniously with a HEM flight on April 29, 2008 across a polynya and segmentation results. The segmentation thresholds were set such that a digital number (DN) below 60 identifies open water, while a DN above 120 comprises rafting. Classes are then segmented into areas of connected pixels. The minimum area of a potential open water or rafting zone is 0.2 m^2. To separate between rafted ice and unrafted ice a minimum contrast between features is needed. Flat sun angles, clouds or the presence of snow or frost flowers on thin ice make it difficult or impossible to distinguish between rafted and unrafted ice using a simple threshold value. Another limiting factor for ice feature separation is the ice thickness. Unrafted ice thicker than 0.3 m has a brightness value similar to rafted ice. Thus, a separation works well only for unrafted ice thinner than 0.3 m. Figure (4.6) presents fractions of classified open water and rafted ice in individual aerial photos taken during the same flight with distance from the polynya edge. At the time of the aerial survey, the observed

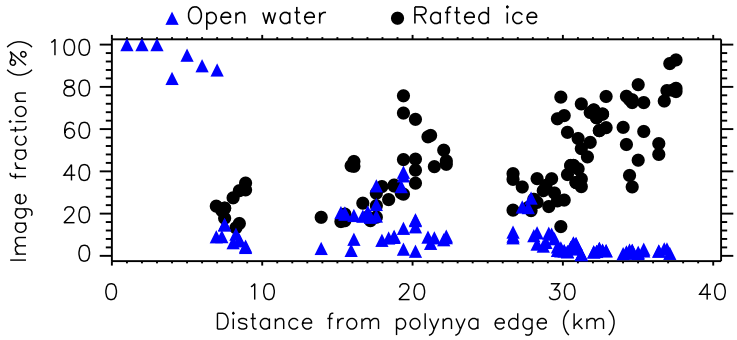

Figure 4.6: Image segmentation results of an aerial photo survey performed across a polynya in the Laptev Sea on April 29, 2008 at 4 UTC: Blue triangles represent the open water fraction extracted from individual aerial photos with distance from fast ice edge. The black circles show the fraction of rafted thin ice.

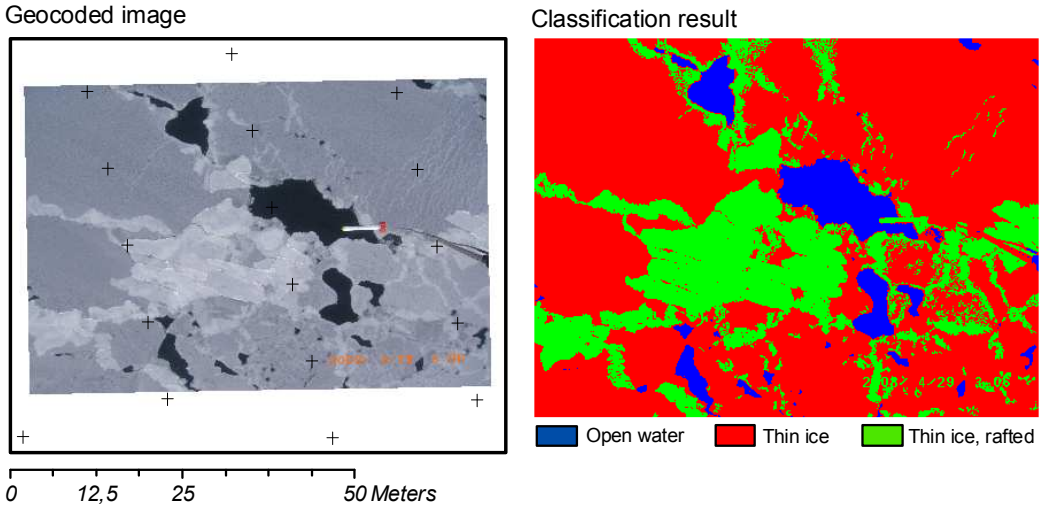

Figure 4.7: Ice type segmentation. Top: georeferenced aerial image acquired on April 29, 2008 at 4 am UTC over the polynya. The photograph was taken simultaneously with a HEM survey at 45 m height. Image footprint is 70 x 62 m. Bottom: Image segmentation result showing the separation of open water (blue) and areas of non-rafted (red) and rafted (green) ice.

polynya open water width was 7 km. Thin ice covered an area of 7 to 38 km on the downwind side of the polynya. Data gaps between 9 - 14 km and 23 - 26 km result from HEM instrument calibration (Haas and others, 2009).

Some airborne instruments, like HEM ice thickness sensors, require flying altitudes below 50 m. Hence, the image footprint becomes relatively small and converges towards the accuracy of the georeferenced image. As a consequence, features measured by the instrument may be outside the image frame. Nevertheless, photographs can be used to assess the relative accuracy of the low-level airborne measurements.

4.4 Conclusion

In this paper we present the prototype of a low-cost photogrammetric system that can be used for the mapping of sea ice in high latitudes. The system is designed for simplicity and flexibility. It withstands low temperatures, operates autonomously and fits to any standard helicopter skid.

The performace of the system was tested by means of accuracy analysis and case studies. Overall, we found HELIOS to be sufficient for the documentation of various ground- and airborne sea ice surveillances. This applies to standardized and regular documentation of sea ice surface properties as well as the verification of satellite-, and model-based estimates of sea ice and snow cover properties. Images taken simultaneously with other airborne observations provide a valuable tool to assess the accuracy of those measurements. Depending on the required accuracy of a mapping project, HELIOS can further be used for photogrammetric surveys.

4.5 Acknowledgments

This work was part of the German-Russian cooperation 'System Laptev Sea' funded by the BMBF under grant 03G0639A and the Alfred Wegener Institute. The authors kindly acknowledge exchange and helping hands during field campaigns from other project members and Russian colleagues. ENVISAT Satellite data were obtained through ESA Project EO-500 'Formation, transport and distribution of sediment-laden sea-ice in the Arctic Shelf seas'.

5

Paper 4: Sea ice production and water mass modification in the eastern Laptev Sea

Manuscript, submitted to *Journal of Geophysical Research*

Thomas Krumpen[1], Jens A. Hölemann[2], Sascha Willmes[3], Miguel Angel Morales Maqueda[4], Thomas Busche[5], Igor A. Dmitrenko[6], Rüdiger Gerdes[1], Christian Haas[7], Günther Heinemann[3], Stefan Hendricks[1], Heidi Kassens[6], Lasse Rabenstein[8], and David Schröder[3]

[1]Department of Sea Ice Physics, Alfred Wegener Institute, Busse Str. 24, 27570 Bremerhaven, Germany

[2]Department of Observational Oceanography, Alfred Wegener Institute, Busse Str. 24, 27570 Bremerhaven, Germany.

[3]Department of Environmental Meteorology, University of Trier, Behringstr. 21, D-54286 Trier, Germany.

[4]National Oceanography Centre, 6 Brownlow Str., Liverpool L3 5DA, UK

[5]Microwave and Radar Institute, German Aerospace Center, Oberpfaffenhofen-Wessling, Germany

[6]Leibniz Institute of Marine Sciences, University of Kiel, Germany

[7]Department of Earth & Atmospheric Sciences, University of Alberta, Edmonton, Alberta, Canada

[8]Institute of Geophysics, ETH Zurich, Sonneggstr. 5, Switzerland

Abstract

A simple polynya flux model driven by standard atmospheric forcing is used to examine the effect of ice formation taking place during an exceptionally strong Western New Siberian polynya event in February 2004 in the Laptev Sea. The ability of the polynya to form dense shelf bottom water is investigated by adding the brine released during the 2004 polynya event to the average winter density stratification of the water body, pre-conditioned by summers with a cyclonic atmospheric forcing (comparatively weakly stratified water column). Beforehand, the model performance is tested by applying it to the simulation of a well documented event in April 2008. Neglecting the replenishment of water masses by advection into the polynya area, we find the likelihood of convective mixing down to the bottom to be extremely low. The strong density stratification and the apparent lack of extreme polynya events in the eastern Laptev Sea limit convective mixing to a depth of 20 m or less. We conclude that the observed breakdown of the stratification during polynya events is therefore predominantly related to wind- and tidally-driven turbulent mixing.

5.1 Introduction

Numerous coastal polynyas form every winter in all peripheral shelf seas of the central Arctic (Gloersen and others, 1992; Barber and Massom, 2007). These coastal polynyas (also termed flaw polynyas when they form adjacent to landfast-ice), are nonlinear-shaped regions of open water and thin ice created as offshore winds push the pack ice away from the coast or the landfast-ice edge (Smith and others, 1990; Morales Maqueda and others, 2004). Surface heat loss within a coastal polynya results in the formation of frazil ice that is transported towards the downwind edge of the polynya. The frazil ice arriving at the polynya edge forms a thin layer of ice and water slurry called grease ice (Winsor and Bjoerk, 2000) which thickens and eventually consolidates as it drifts further offshore. Salt expelled during the formation of ice leads to a downward precipitation of brine that causes thermohaline convection and erodes the density stratification of the water column (Ivanov and Golovin, 2007). The thermohaline convection may indeed lead to total water homogenization, in which case dense bottom water is formed (Backhaus and others, 1997). Density-driven vertical mixing in coastal polynyas is a key control of the shelf sea dynamics since it affects momentum, heat and biogeochemical air-sea fluxes (Morales Maqueda and others, 2004), and provides conditions for downslope transport of water, sediments and pollutants. (Reimnitz and others, 1994; Sherwood, 2000; Smedsrud, 2004).

The Laptev Sea flaw polynyas are among the most controversially discussed circum-Arctic shelf seas in terms of ice production and polynya induced formation of higher saline water (Zakharov, 1966; Cavalieri and Martin, 1994; Dethleff and others, 1998; Dmitrenko and others, 2005, 2009;

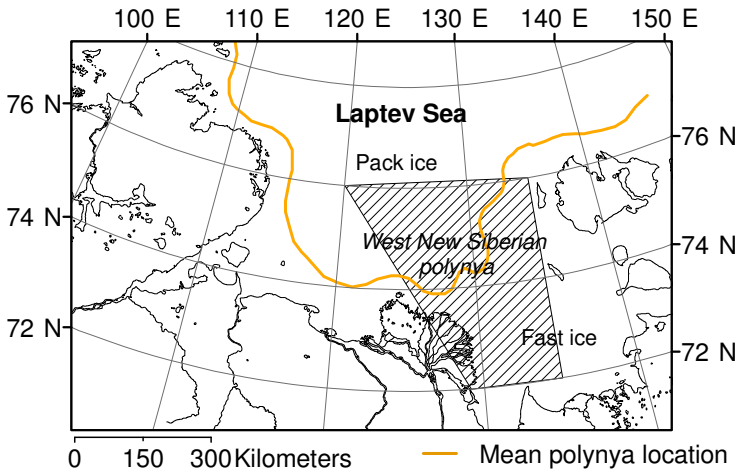

Figure 5.1: Map of the Laptev Sea and mean location of recurrent coastal polynya (yellow line). The grey box indicates the position of the Western New Siberian polynya.

Willmes and others, 2010a). It is estimated that as much as 20 % of the ice transported through Fram Strait is produced in Laptev Sea flaw polynyas (Rigor and Colony, 1997). This shows that the polynyas in the Laptev Sea are very active with high ice production. However, the ice volume produced is fairly modest compared to, for example, the Beaufort Sea owing to the relatively short coastline (Winsor and Bjoerk, 2000). Following Winsor and Bjoerk (2000), who investigated Arctic polynyas between 1958 and 1997 by means of a polynya model, there is also a noticeable lack of polynya extreme event.

Potential sites for dense water formation are located in the central and northwestern Laptev Sea (Willmes and others, 2010a). Following Schauer and others (1997) and Lenn and others (2008) the dense water formed in these polynyas is believed to feed the Arctic halocline but is found to be insufficiently dense to ventilate the layers below.

In the eastern Laptev Sea and the area around the Western New Siberian polynya (WNS; Fig. 5.1), the large summer run-off of the Lena river freshens the surface ocean layer and leads to the development of a distinct vertical density gradient in the water column (Dmitrenko and others, 2005). The strength of the stratification is controlled by the atmospheric circulation during summer months. Anticyclonic wind conditions force the riverine water northwards and result in a stronger density stratification in the eastern Laptev sea. Cyclonic atmospheric circulation deflects the freshwater plume of the River Lena eastward towards the East Siberian Sea, thus causing higher salinities in the eastern Laptev Sea and the area around the WNS polynya. This results in weaker density stratification, as observed in 2007 by Hoelemann and others (2010).

According to Dmitrenko and others (2005), the probability for convective mixing in the region of the Western New Siberian polynya is around 20 %. Their findings are based on hydrological data obtained between 1979 and 1999 rather than sea-ice observations. Owing to the strong stratification and the noticeable lack of extreme polynya events (Winsor and Bjoerk, 2000), we hypothesize that ice production alone in the WNS polynya is not high enough to erode the halocline and that the probability for dense water formation is far lower than the 20 % calculated by Dmitrenko and others (2005). In this paper, this hypothesis is tested by examining the effect of intense ice formation taking place during an exceptionally strong and consistent polynya event on a water column structure with a relatively weak vertical density gradient, pre-conditioned by a cyclonic atmospheric circulation during summer.

Below we use an idealized polynya flux model (Pease, 1987) to simulate an extremely strong opening event of the WNS polynya. Starting on February 10, 2004, constant offshore winds opened up the polynya for a period of 27 days. The flux model computes the evolution of

the open water area and resultant thin ice zone, and the associated ice and salt fluxes. The water body was pre-conditioned toward a weak stratification state by a cyclonic atmospheric circulation regime during summer 2003. For the calculation presented in this study we used an average water mass structure that is representative of the density stratification in the area of the WNS polynya during years with a cyclonic atmospheric circulation. The underlying hydrographic data were taken from the data archive of the Russian Arctic and Antarctic Research Institute and former Russian-German expeditions. The ability of the polynya to form dense shelf bottom water is judged by integrating the amount of salt rejection over the weakly stratified water column.

Because ice production and salt rejection in a polynya are highest inside the open water zone, an accurate determination of ice and salt fluxes requires a correct simulation of the open water edge evolution (Morales Maqueda and others, 2004). Unfortunately, a satellite-based verification of computed open water extents is difficult, since open water edges are not easily identifiable in satellite images (Barber and others, 2001; Haarpaintner and others, 2001). Prior to the simulation of the major polynya opening event observed in 2004, we therefore tested the model parameterizations and performance by applying it to a minor but well documented opening event in April, 2008. The event lasted for approximately 6 days and was observed during the TRANSDRIFT XIII (TD XIII) expedition carried out within the framework of the Russian-German research cooperation programme "Laptev Sea System". Information on the temporal and spatial evolution of the open water area and pack ice edges, as well as the thickness of thin ice, were obtained from photogrammetric and electromagnetic airborne surveys, thermal infrared satellite imagery and high-resolution RADAR satellites.

The structure of the paper is as follows. First, the model description is given in section 2. We then describe the dataset used for model calibration and verification (section 3). In section 4, we apply the model to the well documented event of April 2008 and to the exceptionally strong opening event of February 2004. In addition, the model parameterizations and performance are tested and discussed by comparing simulated open water width and thin ice thickness with observations and satellite-based estimates. Subsequently, we investigate the effect of ice production during the 2004 event on a weakly stratified water body, pre-conditioned by a cyclonic circulation regime in summer (section 5). Conclusions are drawn in section 6.

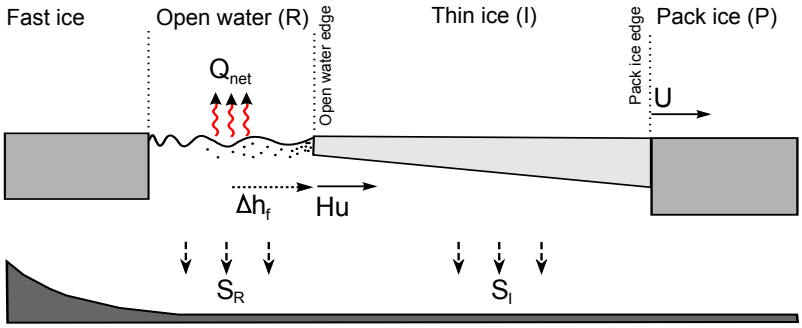

Figure 5.2: Schematic illustrating of the polynya model. In the open water area, heat loss to the atmosphere (Q_{net}) results in frazil ice growth with rate $\Delta h_f/\Delta_t$. Frazil ice piles up against the open water edge with thickness H and then drifts away from the edge with speed u. The pack ice edge moves with velocity U. The instantaneous salt flux from frazil ice growth in the open water zone is given by S_R. Salt rejection induced by the continuous growth of consolidated new ice is denoted by S_I.

5.2 Polynya flux model description

The objective of our model is to calculate the amount of ice production and salt rejection in a flaw polynya on the basis of wind and air temperature information. Below, we briefly describe the concepts behind the model. Following Haarpaintner and others (2001), two simple one-dimensional drift algorithms are used to simulate the evolutions of the open water region and the pack ice edge (Fig. 5.2).

The first algorithm computes the width of the wind-generated open water zone R (Pease, 1987). Because of its simple idealized formulation and its ability to provide fairly accurate ice production estimates (Krumpen and others, 2010c), a flux model is used. Polynya flux models were first formulated by (Pease, 1987), embracing an idea of Lebedev (1968) that wind-generated coastal polynyas attain a maximum size determined by a balance between ice production within and flux of ice out of the open water zone (e.g. Willmott and others, 2007).

Following (Pease, 1987), the width of the open water zone, R, can be expressed as

$$R_t = R_{t-\Delta_t}(1-\Delta h_f/H) + u\Delta_t, \tag{5.1}$$

where R_t is the open water width at time t and Δt is the temporal resolution of the atmospheric dataset. Δh_f is the amount of frazil ice produced in the water column between time t and $t-\Delta t$, calculated from the surface heat balance Q_{net} (Cavalieri and Martin, 1994):

$$Q_s + Q_l + Q_{lw} + (1-\alpha)\,Q_{sw} = -Q_{net}/\left(\rho_f L_s\right) = h_f, \tag{5.2}$$

where Q_s and Q_l are the turbulent sensible and latent heat fluxes, respectively, Q_{lw} is the net longwave radiation at the sea surface, Q_{sw} is the shortwave solar radiation, and α is the surface albedo (Cavalieri and Martin, 1994; Morales Maqueda and others, 2004). In Equation (5.2), ρ_f is the frazil ice density and L_s is the latent heat of fusion for sea ice (Martin and Kauffman, 1981; Pease, 1987). If Q_{net} is negative, the water body transfers heat to the atmosphere and frazil ice is produced. The atmospheric forcing is assumed to be uniform over both the open water and thin ice regions. Finally, u in (1) is the speed of consolidated new ice at the open water edge (Fig. 5.2).

After formation, frazil ice instantaneously piles up against the open water edge and consolidates into a thin ice layer with thickness H. Following Biggs and others (2000), in this study we determine H as a function of the depth of frazil ice arriving at the open water edge and an increase in thickness caused by the piling up of frazil ice against ice floes.

According to Skogseth and others (2004), the drift of consolidated new ice away from the open water edge, u, can be described by

$$u = \epsilon_c U_a cos(\varphi_m - \varphi_o), \tag{5.3}$$

where ϵ_c is a non-dimensional proportionality constant, U_a is wind speed, φ_m is the wind direction, and φ_o is is the wind direction with strongest effect on the opening of the polynya (Haarpaintner and others, 2001). Following (Pease, 1987), the constant of proportionality is set to 0.03. In Equation (5.3), φ_o is taken from satellite images (Skogseth and others, 2004) and is set to 130° for the WNS polynya.

The continuous thermodynamic growth of the consolidated new ice is calculated by Stefan's law (Petrich and Eicken, 2010). In spite of its simplicity, the so called degree day model is capable of producing fairly accurate predictions of sea ice growth.

The evolution of the pack ice edge P is reconstructed by a second drift equation

$$P_t = P_{t-\Delta_t} + U\Delta_t, \tag{5.4}$$

where P_t is the pack ice extent at time t and U is the velocity of the pack ice drift. U is calculated similar to Equation (5.3), but with ϵ_c set to 0.01. Following Haarpaintner and others (2001), the variability in ice drift between 1 % of the wind velocity in very dense pack ice and 3 % inside the polynya area is based on a comparison between the displacement of individual ice floes in SAR scenes and the wind velocity.

The width of the thin ice zone I is calculated as the difference between P and R. The area of the polynya is computed by multiplying its width times the alongshore length L of the WNS polynya (195 km).

The accuracy of ice production estimates obtained from a polynya flux model was investigated by Krumpen and others (2010c), who compared model results to ice thickness and ice production estimates derived from thermal infrared satellite data. It was found that regional discrepancies between model and satellite observations are at least partly due to the missing representation of the dynamics of thin ice thickening. To overcome this deficiency, we parameterize the effect of dynamic thickening of thin ice in the model by assuming that the differential drift of the pack ice and consolidated new ice, $U - u$, results in ice rafting and, therefore, compression of the thin ice zone, I. The dynamic ice thickening caused by this compression is governed by the equation of conservation of mass. Based on literature and field observations we assume rafting to be limited to ice thinner than 0.3 m (Melling and others, 1993; Worby and others, 1996; Babko and others, 2002). There is a lack of studies on rafting probabilities in thin ice, and so it is not known how the compression is distributed through ice thinner than 0.3 m. However, for simplicity, we assume the effects of compression on a thin ice zone to decrease linearly with ice thickness.

As ice grows, salt is rejected and added to the water body. The amount of salt rejected is dependent on the initial surface salinity. The instantaneous salt flux from frazil ice growth in the open water zone, S_R, is calculated following Winsor and Bjoerk (2000). The formulation of Ryvlin (1974) is used to estimate salt rejection induced by the continuous growth of consolidated ice, S_I.

5.3 Data

5.3.1 Satellite observations

The evolution of the 2004 and 2008 polynya events were continuously monitored with different satellites.

Environmental Satellite (ENVISAT) Advanced Synthetic Aperture Radar (SAR) images provide information about ice dynamics in the eastern Laptev Sea. Each polynya event is covered by 4 scenes. Two of the scenes for 2008 and another two for 2004 are shown in Figure (5.3) and Figure (5.4), respectively. The ENVISAT C-band wide swath data is VV-polarized and covers an area of approximately 400 × 800 km^2 with a spatial resolution of 150 × 150 m^2. Fast ice and

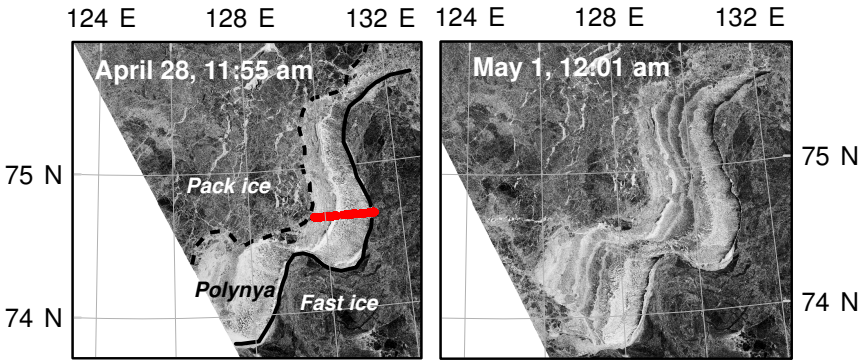

Figure 5.3: ENVISAT SAR images acquired on April 27 and May 1, 2008, covering the Western New Siberian polynya. The sea ice regime consists of the fast-ice zone (south of the black solid line), an active polynya zone (open water and thin ice), and a region of freely floating pack-ice (north of the black dashed line). The red line in the left panel highlights the profile of the HEM-Bird ice thickness measurements on April 29 at 4 UTC.

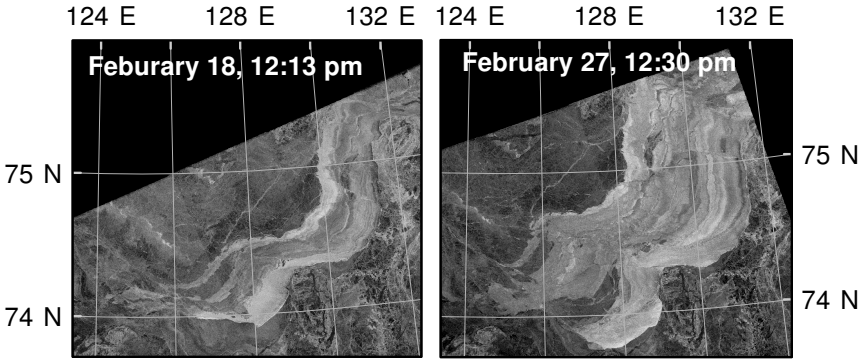

Figure 5.4: ENVISAT SAR images acquired on February 18 and 27, 2004. The scenes cover the position of the Western New Siberian polynya, showing the fast ice belt, the active polynya zone, and a region of freely floating pack ice.

pack ice edges, and hence the polynya width, are easily identifiable in SAR images. The determination of open water width is not straight forward, since the backscatter signatures inside the open water region and the consolidation zone can be very inhomogeneous and vary with meteorological conditions. In addition, often no clear boundary does exists between open water and consolidated thin ice. To validate open water width simulated by the model in 2008, the interpretation of ENVISAT SAR imagery is aided by helicopter-based observations, high-resolution TerraSAR-X scenes, meteorological data, and surface temperature information from the Advanced Very High Resolution Radiometer (AVHRR). The validation of the 2004 event simulation is exclusively based on ENVISAT SAR scenes, thermal AVHRR images and atmospheric information.

The TerraSAR-X scenes (Strip Map Mode, X-Band) are dual-polarized (HH-VV) with a spatial

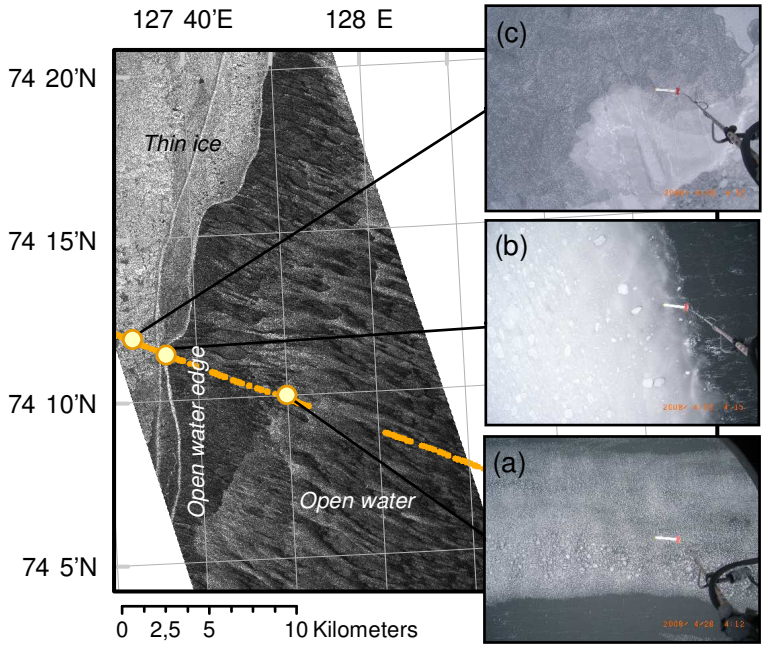

Figure 5.5: TerraSAR-X SAR image acquired on April 28, 2008 at 8.37 UTC. The scene covers parts of the open water and thin ice zones of the WNS polynya. Aerial photographs taken on a helicopter flight across the polynya are plotted on top of the SAR scene as orange dots. The three enlarged aerial photographs, with the black lines pointing to the corresponding footprint, show the open water zone (a), the open water edge (b), and rafted thin ice (c).

resolution of 6.6 × 1.2 m^2 and cover a 15 km wide and 150 km long swath across the polynya. The 5 images were primarily used to investigate polarimetric ice signatures (Busche and others, 2009). However, we also found the high-resolution sensor to be a valuable instrument to monitor thin ice dynamics and the evolution of the consolidation and open water zone during TD XIII. An example is given in Figure (5.5). A TerraSAR-X image obtained on April 28, 2008 at 8.37 UTC is shown together with drift corrected aerial photographs, taken three hours and 40 minutes before satellite acquisition. The three enlarged aerial photographs, with the black lines pointing to the corresponding footprint, show the open water zone (a), the open water edge (b), and rafted thin ice (c).

To validate the model simulated ice thickness, thermal infrared data is used to derive estimates of thermal ice thickness, h_{TH}, calculated with the aid of an atmospheric dataset (section 3.4) using the surface energy balance model suggested by Yu and Lindsay (2003). Ice surface temperatures are derived from thermal infrared channels following the split-window method of Key and others (1997). Level 1B calibrated radiances (visible and thermal infrared) were obtained from the U.S. National Oceanic and Administration (NOAA) Comprehensive Large Array-

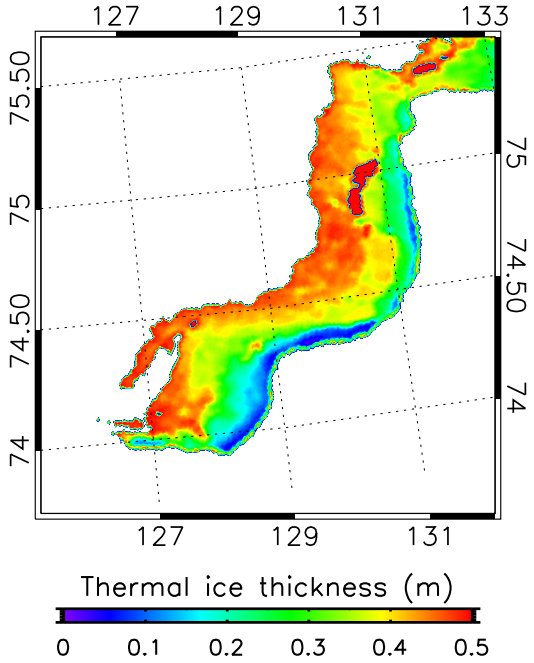

Figure 5.6: Thermal ice thickness (h_{TH}) as derived from AVHRR surface temperatures taken on February 18, 2004, at 12:00 UTC and NCEP/DOE reanalysis data.

data Stewardship System (CLASS). The spatial resolution of AVHRR Local Area Coverage (LAC) data is 1.1 × 1.1 km^2. The method requires clear-sky conditions. In total, we identified 1 scene, covering the event in 2008, and 2 scenes imaging the opening in 2004. The thickness retrieval is based on the assumption that the heat flux through the ice equals the atmospheric heat flux. The method yields good results for ice thicknesses below 0.5 m, further assuming that vertical temperature profiles within the ice are linear and no snow is present on top of the ice (Drucker and others, 2003). Figure (5.6) shows the thermal ice thickness distribution inside the polynya area as derived from an AVHRR image taken on February 18, 2004.

5.3.2 Airborne data

During TD XIII, two helicopter-borne surveys of electromagnetic (HEM) ice thickness, h_{HEM}, were performed across and along the WNS polynya. The profile obtained on April 29, 2008 is shown in Figure (5.3). It is used to validate polynya flux computations. The so called EM-Bird, is an airborne electromagnetic (EM) system with a single-frequency of 4.08 kHz (Haas and others, 2009). The instrument was towed by a helicopter 15 meters above the ice surface. The method utilises the contrast of electrical conductivity between sea water and sea ice to determine the

distance to the ice-water interface. An additional laser altimeter yields the distance to the uppermost reflecting surface, hence h_{HEM} is obtained as the ice- plus snow thickness from the difference between the laser range and the EM derived distance. Since the laser beam is always reflected at the uppermost surface, snow thickness, if present, is included in h_{HEM}. However, the polynya event in 2008 is characterized by the absence of a snow cover on the thin ice, and therefore h_{HEM} presents the real ice thickness. The measurements were taken with point spacing of 3 to 4 m depending on the speed of the helicopter. Within the footprint of a single measurement (40 - 50 meter) the accuracy over level sea ice is in the order of ± 0.1 m (Pfaffling and others, 2007; Haas and others, 2009).

On all HEM flights, geo-coded aerial photographs were taken with a downward-looking digital camera (Krumpen and others, 2010a). Images were used to provide general information about ice dynamics, to support the calibration of HEM ice thickness measurements and to aid TerraSAR-X and ENVISAT image interpretation (Fig. 5.5).

5.3.3 Historical hydrographic information

The mean stratification of the water column in winter 2004 was constructed by using salinity records obtained during the Arctic and Antarctic Research Institute (ARRI) Sever expeditions (1979-1990, 1992 and, 1993), together with CTD measurements made during several Russian-German winter expeditions (Dmitrenko and others, 2005). The mean stratification pattern and its standard deviation (STDV) is calculated by averaging salinity measurements made during winter surveys, pre-conditioned by summers with a cyclonic atmospheric circulation regime. In total, 10 stations completed between February and May in the region of the WNS polynya are used to calculate the mean stratification pattern. Most of the surveys were carried out in the 70s and 80s, when the atmospheric circulation in summer was predominantly cyclonic (Dmitrenko and others, 2009).

5.3.4 Atmospheric dataset

The model is driven with atmospheric data extracted from a single grid point in the center of the polynya. Polynya evolution, ice production and salt rejection are calculated using sea level pressure, 2 m air temperature and humidity, precipitation, surface net radiation and 10 m wind vectors.

The simulation of the opening event of 2008 is driven with 1-hourly data from COSMO simulations (Consortium for Small-Scale Modeling) which were specifically performed for the Laptev

Sea area by Schroeder and others (2010). By prescribing the polynya areas daily these data account for the impact of polynyas on the atmospheric boundary layer. The quality of the COSMO data is shown by a comparison with automatic weather stations and surface temperature derived from MODIS satellite data (Schroeder and others, 2010).

Ice and salt fluxes during the polynya event of 2004 are computed with 6-hour NCEP/DOE reanalysis atmospheric forcing fields (Kanamitsu and others, 2002).

5.4 Model simulations

5.4.1 Satellite observations and atmospheric conditions during the 2008 event

According to airborne observations, AVHRR scenes and TerraSAR-X and ENVISAT SAR imagery, the 2008 polynya event started on April 27 and lasted for a period of 6 days. Consistent offshore winds and temperatures between - 17°C and - 4°C, upper panel) led to the formation of a 4 - 16 km wide open water zone and an extensive region of new thin ice. On May 2 air temperatures raised above the freezing point of sea water, causing the polynya to gain heat and ice production to halt.

The COSMO-based 1-hourly air temperatures and 6-hourly wind velocities for the time of interest are presented in the upper panel of Figure (5.7). Figure (5.3) shows the WNS polynya as observed by two SAR scenes acquired on April 28 and May 1, 2008. Open water zones are made visible by the brighter parallel wind-generated Langmuir streaks oriented perpendicular to the fast ice edge (Drucker and others, 2003). The bright and dark radar backscatter features within the polynya region are associated with pancake and frazil ice formation (Kwok and others, 2007). Several bands of consolidated new thin ice orientated nearly parallel to the fast ice edge are apparent downwind of the open water area.

5.4.2 Simulation of the 2008 event

The polynya flux model was used to simulate the first 5.25 days of the 2008 polynya opening event. The model's atmospheric forcing was extracted from the COSMO atmospheric dataset. Frazil ice production in the open water area, ice growth in the thin ice zone, and associated salt rejection were calculated by making the following assumptions. First, the salinity of the surface layer at the onset of the polynya opening was set to 26 psu, following hydrographic observations made along the fast ice edge during TD XIII. Second, frazil ice growth in model

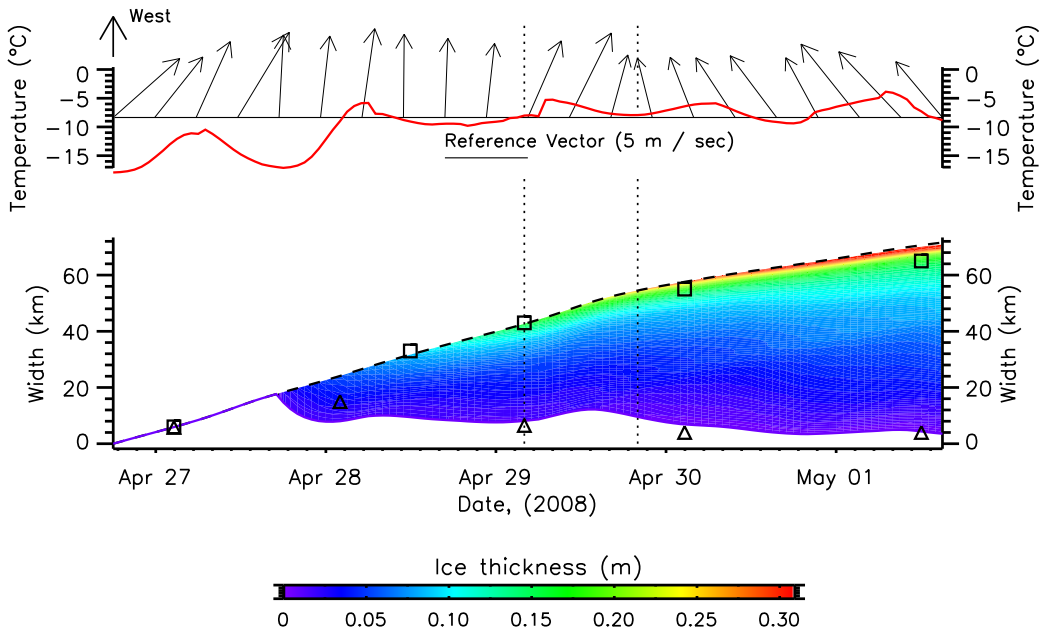

Figure 5.7: Atmospheric data (COSMO) and polynya model results during the study period in April 2008. Upper panel: 2 m air temperatures and 10 m wind vectors showing the direction of air flow, with their lengths representing wind speed. Lower panel: Modelled (black dashed line) and observed (black rectangles) total polynya width. Modelled ice thickness is colour-coded. The white area is the simulated open water width and the black triangles represent the observed open water width. Dotted vertical lines mark the dates of ice thickness reference measurements (HEM-Bird: April 29, 4 UTC; AVHRR: April 29, 20 UTC) used for model verification.

computations was suppressed for the first 24 hours, because supercooling of the water body started approximately 1 day after the polynya started to open (Dmitrenko and others, 2010b).

The lower panel of Figure (5.7) presents the simulated and observed evolution of the widths of the open water and thin ice areas, and the modelled thin ice thickness over the 5.25 days of simulation. At the onset of the polynya event, persistent easterly winds push the pack ice edge offshore, resulting in the development of a wide open water zone. A thin ice zone in the model develops 24 hours after frazil ice formation starts, and is then continuously thickening by thermodynamic and dynamic processes. On April 29, the modelled thin ice zone extends up to 40 km offshore and the open water area reaches a width of approximately 8 km. Later, a slight change in wind direction and a temporary decrease in wind velocity cause a slow down of ice offshore transport, reducing the width of the open water zone to 4 km.

The simulated evolution of the WNS polynya agrees well with observations. The mean deviation between modelled and satellite observed position of the pack ice edge is 0.5 km. The deviation between modelled open water width and satellite and airborne observations is 1.4

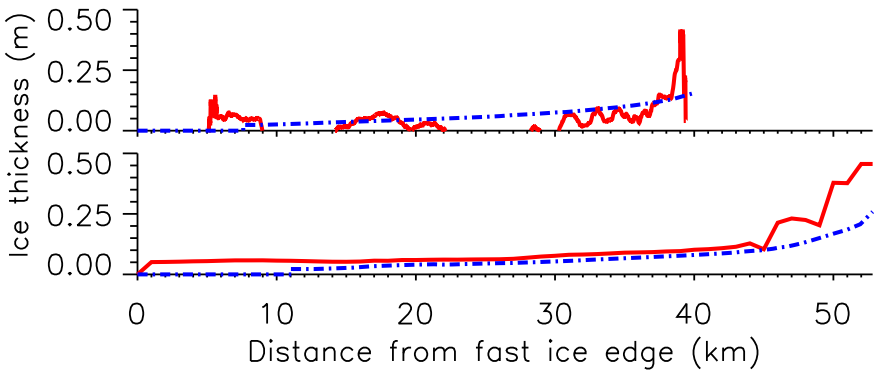

Figure 5.8: Upper panel: Comparison of the HEM-Bird ice thickness profile (solid red line) taken on April 29, 2008 at 4 UTC across the thin ice zone with the modelled ice thickness profile (dashed blue line). Lower panel: Comparison of an AVHRR derived ice thickness profile (h_{TH}, solid red line, April 29 2008, 20 UTC) of the thin ice zone with the simulated ice thickness profile (dashed blue line).

km.

The accuracy of the simulated thin ice thickness is tested by comparing model results to ice thickness estimates obtained from the HEM flight on April 29 at 4 UTC and from a thermal infrared AVHRR scene acquired 14 hours later (Fig. 5.8). For comparison, HEM measurements were averaged over a 250 m interval. Gaps in h_{HEM} data at distances of 9 - 14 km and 23 - 26 km offshore the fast ice edge are the result of HEM instrument calibration (Pfaffling and others, 2007). The comparison shows that simulated ice thickness is near the range of h_{HEM} measurements, although the model slightly underestimates the observations. Highest ice thicknesses can be found close to the pack ice edge in both HEM observations and model simulations.

The agreement between AVHRR infrared ice thickness and model results is also high. Note that the AVHRR ice thickness profile shown in Figure (5.8) is averaged along the polynya. Both AVHRR and model data show an increase in ice thickness with distance from the fast ice edge. The simulated ice thickness tends to be generally lower than thermal ice thickness observations. As opposed to the model, the AVHRR sensor does not resolve the open water zone. Instead, the zone close to the fast ice edge is characterized by very low thicknesses varying between 0.01 and 0.05 m.

In total, an ice volume of 1.3 km^3 is formed between April 27 and May 01, 2008. Of this ice, 38 % (0.5 km^3) is produced in the open water zone, which represents on average 25 % of the entire polynya area. The total amount of salt rejected is about 0.14×10^{11} kg, of which 0.08×10^{11} kg are rejected as frazil ice forms in open water zone. According to calculations made by Winsor and Bjoerk (2000), the mean seasonal salt rejection in this area is around 0.77×10^{11} kg. Without any advection and the absence of a stratification, 0.08×10^{11} kg of salt would increase

the salinity of the open water zone, which has a depth of 25 m, by approximately 1.0 psu.

5.4.3 Discussion of flux model parameterizations and performance

Because ice production and salt rejection are highest in the open water area, accurate determination of the open water edge in the model is of paramount importance. The comparison of simulated open water width with observations made by helicopter, high-resolution TerraSAR-X scenes and ENVISAT SAR images has shown that the flux model is capable of simulating correctly the extend of the open water zone (Fig. 5.7). This is in agreement with findings made by Haarpaintner and others (2001), Skogseth and others (2004) and Krumpen and others (2010c). Deviations between simulated and observed open water widths are related to the parameterizations and representation of physical processes in the model, and are discussed below.

The assumption of spatial uniformity is justified by the fact that longshore variations in wind direction and air temperature, and their associated errors in computed ice and salt fluxes, are comparatively small for both polynya events. Nevertheless, if dealing with larger longshore polynya dimensions, the use of a two-dimensional flux approach driven by a spatially variable atmospheric forcing is required (Krumpen and others, 2010c). Note that in contrast to the NCEP/DOE reanalysis data used for the simulation of the 2004 event, the COSMO dataset incorporates the impact of the polynya on the atmospheric boundary layer. Therefore 2 m air temperature and the resulting ice production rate are more accurate.

A shortcoming of the polynya flux model is that frazil ice is assumed to instantaneously pile up against the thin ice edge. The incorporation of a finite frazil ice drift rate (Ou, 1988) and the effect of currents on the modelled frazil ice drift trajectories (Willmott and others, 1997) becomes important as the open water region grows in size. However, the development of large open water zones in the eastern Laptev Sea polynyas is generally a rare event owing to prevailing low temperatures and moderate wind speeds during winter (Winsor and Bjoerk, 2000).

We find the simulated open water region width and thin ice thickness to be extremely sensitive to the parameterization of the collection depth H. Different parameterizations used in one-dimensional and two-dimensional polynya flux models are discussed in Martin and Kauffman (1981), Pease (1987), Winsor and Bjoerk (2000), Morales Maqueda and Willmott (2000) and Krumpen and others (2010c). The use of a constant thickness parameterization (0.1 m or 0.2 m) leads to a crude overestimation of the width of the open water region and the thin ice thickness. In our study, the best results were achieved by using the parameterization of Biggs and others (2000), who determine the consolidation thickness as the sum of the thickness of frazil ice ar-

riving at the edge and a pile up depth. In an earlier study we have shown that, in addition to a more correct representation of the open water extent, the use of this parameterization results in more realistic thin ice thickness (Krumpen and others, 2010c).

Both HEM and AVHRR derived thin ice thickness profiles show a strong increase in thickness towards the pack ice edge (Fig. 5.8). This increase is also visible in the simulated ice thickness distribution, and results from enhanced dynamic ice growth. In the model, the compression of the thin ice zone (dynamic thickening) is a consequence of the difference in pack ice drift U and consolidated new ice velocity u. At the onset of the event, compression acts on a relatively narrow thin ice zone, resulting in a strong dynamic ice thickening. When the thin ice zone is growing in width, compression is distributed over a larger area and ice deformation weakens. The good agreement between observations and simulations indicates that the representation of dynamic ice growth in the model is a reasonable approximation. However, the drift equations for U and u are highly simplified and contain empirically tuned and highly uncertain parameters (Equation 5.3). Owing to the plasticity of the thin ice cover, ice drift rates are likely to vary in space and time. The associated errors are unknown.

Note that the HEM profiles used to verify model results are challenging for two reasons. Firstly, the processing of the EM-Bird data is based on the assumption that sea ice can be regarded as a non-conductive medium. Over thin ice, however, this assumption may be invalid because the conductivity of saline young ice can be significantly higher than that of older first year or multi year ice. This may lead to underestimates of the ice thickness. Therefore, all h_{HEM} data have to be interpreted as minimum ice thicknesses. Secondly, the conductivity of the surface waters can be low and highly variable due to their proximity to the freshwater input by the Lena River. Although a relatively low water conductivity of between 2200 and 2400 S m^{-1} was used for the retrieval of ice thicknesses, our processing algorithms do not take into account conductivity variations during individual flights.

The accuracy of thermal infrared AVHRR thickness estimates is difficult to assess but believed to be within a range of ± 20 % (Drucker and others, 2003). Because time of interest is characterized by the absence of snow coverage, the largest source of error in h_{TH} probably arises from uncertainties in the atmospheric dataset. Unfortunately, AVHRR thermal thickness estimates do not resolve open water zones present on SAR imagery and aerial photography. In thermal infrared observations open water areas are characterized by a surface temperature close to the freezing point of seawater. However, the presence of frazil ice, Langmuir streaks or ice floes in the water column lowers the averaged surface temperature within the sensor footprint beneath

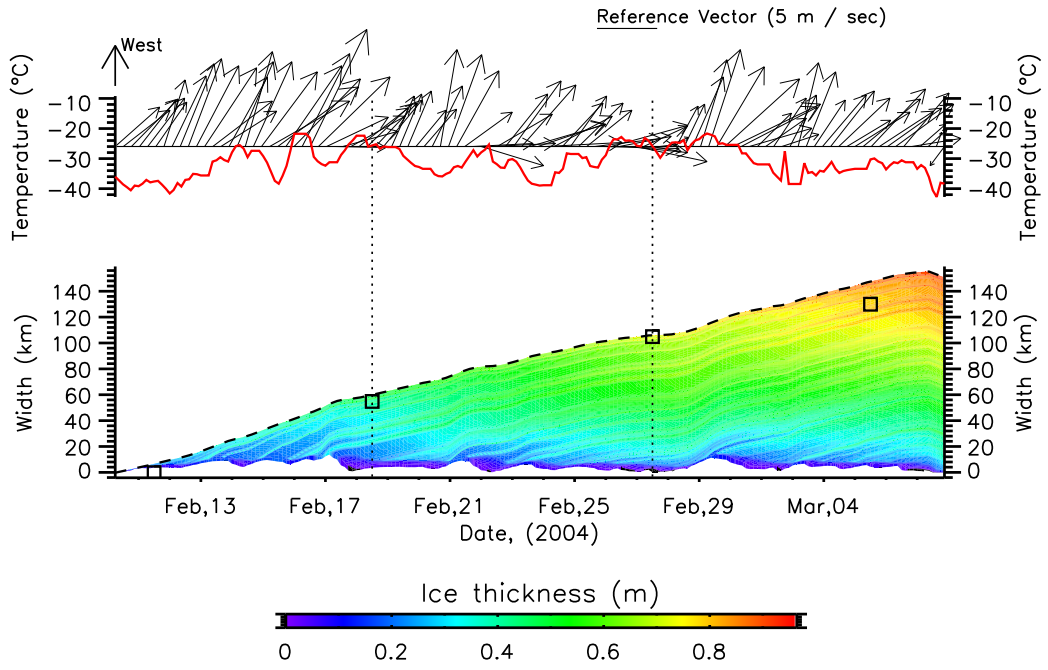

Figure 5.9: Atmospheric data (NCEP) and polynya model results during the study period in February 2004. Upper panel: 2 m air temperatures and 10 m wind vectors showing the direction of air flow, with their lengths representing wind speed. Lower panel: Simulated (black dashed line) and observed (black rectangles) total polynya width. Simulated ice thickness is colour-coded. The white area is the simulated open water width. Dotted vertical lines mark the dates of ice thickness reference measurements (h_{TH}, AVHRR thermal infrared ice thickness estimates for February 18, and February 27, 2004).

freezing point, such that potential open water areas are classified as very thin ice.

5.4.4 Satellite observations and atmospheric conditions during the 2004 event

According to the ENVISAT SAR scenes, the polynya event in 2004 started on February 10, and remained open for 27 days. Strong and consistent offshore winds, together with extremely low air temperatures of between -44°C and -22°C, resulted in strong ice formation and the development of a broad open water area. Figure (5.9, upper panel) presents 6-hourly air temperatures and wind velocities taken from NCEP/DOE reanalysis data, extracted from a single point nominally in the center of the polynya. Figure (5.4) shows two SAR images taken on February 18 and February 27, 2004. The polynya opened in a northwest direction. The thin ice zone grew up to an extent of approximately 140 km. A sudden change in wind direction on March 5, caused a temporary closure of the polynya. As in Figure (5.3), the presence of Langmuir streaks indicates ice production in extensive open water zones. The banded structures orientated parallel to the polynya edge are located in the thin ice region.

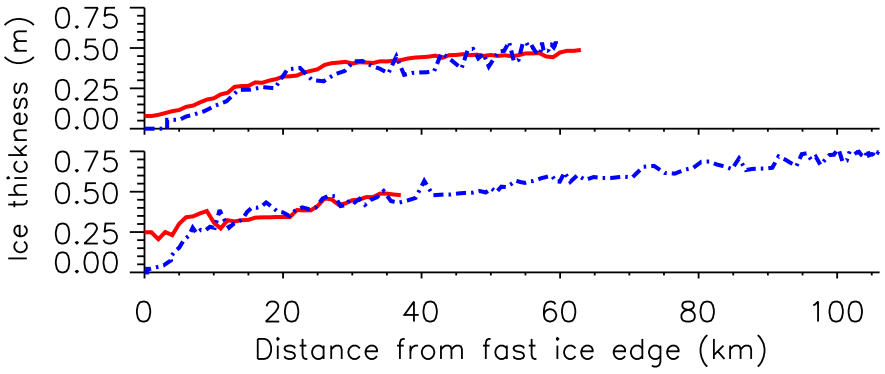

Figure 5.10: Comparison of AVHRR based ice thickness profile (h_{TH}, solid red line) of the thin ice zone with the simulated ice thickness profile (dashed blue line) for February 18 (upper panel) and February 27 2004 (lower panel).

5.4.5 Simulation of the 2004 event

We applied the polynya flux model to the simulation of the exceptionally strong polynya event in 2004. The evolution of the open water and thin ice zones, and the associated ice production and salt rejection, were calculated with atmospheric forcing extracted from NCEP/DOE reanalysis data.

The lower panel of Figure (5.9) presents the simulated and observed evolution of the extents of the open water and thin ice regions, as well as the modelled thin ice thickness over the 27 day duration of the polynya event. The simulated drift of the outer pack ice edge slightly overestimates the remotely sensed drift. A validation of the computed open water width is difficult with ENVISAT SAR images alone.

Low air temperatures and high wind velocities (Fig. 5.9, upper panel), result in an enhanced thermodynamic and dynamic growth of the thin ice zone compared to the 2008 event.

To evaluate the accuracy of the simulated thin ice thickness, we again compare AVHRR infrared ice thickness observations with the model results (Fig. 5.10). The agreement between thermal ice thickness profiles taken on February 18 and February 27 and simulations is high. The mean thin ice thickness on February 18 is 0.34 m for AVHRR and 0.38 m for model ice thickness. The respective thin ice thicknesses on February 27 are 0.32 m and 0.37 m. Note that neither the open water zone nor areas of ice thicker than 0.5 m are resolved by AVHRR.

We estimate that, between February 10 and March 5, 2004, an ice volume of 26 km^3 was produced. Consequently, the 2004 polynya event is approximately 20 times stronger than the event of late April 2008. Approximately 8.1 km^3 (32 % of the total ice production) originates from

frazil ice growth in the open water zone. A comparison of our calculations with estimates made by Dethleff and others (1998), Winsor and Bjoerk (2000) and Dmitrenko and others (2005) confirms this event as an exceptionally strong one. Dethleff and others (1998) calculated the flaw polynyas to produce about 7.4 m of ice per year, while Winsor and Bjoerk (2000) assumes it to be around 14.2 m. Following calculations made by Dmitrenko and others (2005), the average annual polynya ice production is far lower (3 - 4 m). The total amount of salt rejected during the polynya event was estimated at about 2.9×10^{11} kg, of which 1.5×10^{11} kg were rejected in the open water area as frazil ice was created.

5.4.6 Discussion of the 2004 event simulation

The simulated evolution of the pack ice edge is in good agreement with satellite observations. Unfortunately, a validation of the simulated open water width is difficult, as the edge of the open water region is not easily identifiable in SAR scenes. We have confidence, however, in our simulation of the open water evolution, as it was proven to be acceptably accurate for the well documented 2008 event. An additional indication of the level of accuracy of the model is derived from a comparison of the average length of Langmuir streaks in SAR images with the simulated open water width. A comparison shows that the model tends to slightly overestimate the open water width.

The good agreement between simulated thin ice thickness and AVHRR based estimates indicates that the algorithms to calculate the ice drift rates U and u are well tuned. It also suggest that the parameterizations of the thickness of consolidated new ice (Biggs and others, 2000) and of the dynamic thickening of thin ice are appropriate. For a discussion on the accuracy of the thermal AVHRR approach and the errors associated with the different parameterizations of physical processes we refer the reader to section 4.3. Note that an additional uncertainty in the h_{TH} estimates arises from the potential presence of snow on the thin ice. The magnitude of this source of error is unknown.

5.5 Effect of ice formation on the water column stratification

To investigate the effect of thermodynamic ice formation on the stratification of the water body, we uniformly distribute the rejected salt within a 5 km wide band adjacent to the landfast ice (5 km is the mean polynya open water width). Information on mean winter stratification and its standard deviation is derived from historical hydrographic data (section 3.3). Figure (5.11)

shows the stratification of the water column and its STDV before and after the polynya event. Neglecting any horizontal advection of dense water, release of brines from freezing sea ice convectively erodes the pronounced seasonal halocline down to a depth of 20 m (Fig. 5.11, medium grey shading). If instead of the mean winter stratification, we use the mean winter stratification minus its STDV, the convective mixing depth is reduced to 15 m (Fig. 5.11, dark grey shading). If we add, rather than subtract, the STDV to the mean winter stratification the shelf stratification can be fully eroded and dense shelf bottom water can be formed (Fig. 5.11, light grey shading).

The use of the mean climatological stratification plus/minus its STDV to investigate the impact of polynya events on dense water formation is admittedly somewhat crude. The approach is merely exploratory, but sufficiently rigorous, we expect, to provide a zero-order estimate of the potential contribution of polynya events to winter destratification. The mixed layer depths we report on in the previous paragraph may probably be considered as upper bound estimates of destratification potential, as in our simulations, destratification is favored in a number of ways that we enumerate in the following. First, the climatological mean density stratification was calculated by averaging salinity measurements made during winter surveys pre-conditioned for destratification by cyclonic summers. Moreover, the observed winter patterns might have been weakened by preceding polynya activity. Second, as pointed out in section 5.2, ice formation and salt rejection rates taking place for the 2004 opening event were exceptionally high. Third, the model generally overestimates ice formation, and hence salt rejection, owing to the incomplete representation of some physical processes, or their effects, in both the atmospheric dataset and the model (section 4.3). Fourth, ocean currents which are neglected in our model, tend to advect fresher water into the area, thus replenishing eroded water masses and helping to restore stratification. An inclusion of these advective processes in the model would strengthen the stability of the water column and lower the production of ice. For example, if we assume water masses to be replenished by some constant current of 0.02 m s^{-1} normal to the coastline (Winsor and Bjoerk, 2000), replacing the water volume affected by ice formation with water at the initial stratification, the mean convective mixing depth is only 14 m.

Recent year-round mooring observations made during the period from September 2007 until September 2009 in the region of the WNS polynya provide evidence that active polynya formation is usually accompanied by a sharp decrease in near-bottom water salinity and temperature (Hoelemann and others, 2010). These observations are inconsistent with dense water formation by brine rejection and support our hypothesis that even during strong WNS polynya events, ice production is not high enough to erode the halocline. Hoelemann and others (2010) suggest that the salinity decrease is likely to be induced by a wind driven breakdown of the

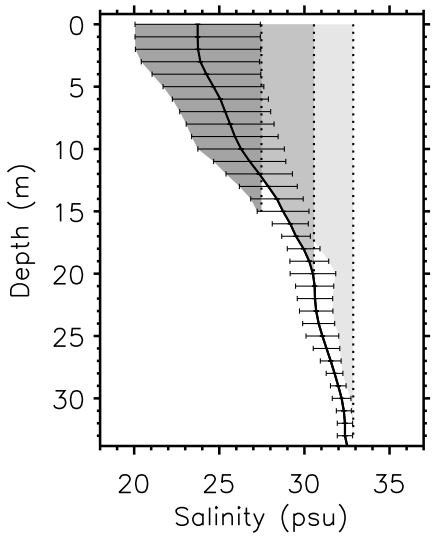

Figure 5.11: Effect of salt rejection on the stratification of the water body. The mean water layer stratification prior to the onset of the opening event is represented by the black solid line. Error bars denote the standard deviation (STDV) from mean. Information on mean stratification and its variance is computed from the historical hydrographic data. The grey shaded areas represent the simulated salinity increase for three different stratification strengths (mean-STDV, dark grey shaded; mean, medium grey shaded; mean+STDV, light grey shaded).

stratification and a cross-pycnocline turbulent mixing, leading to an admixture of the brine enriched but still buoyant surface waters to the more saline, and denser bottom waters (> 25 m water depth).

At present, vertical transport of heat and matter on shelf seas is believed to be controlled by both turbulent and convective mixing (Schauer, 1995; Rippeth, 2008). Our results provide indirect evidence that the mechanisms responsible for the destratification and vertical mixing in the area around the WNS polynya are predominantly wind- and tidally driven, rather than convective. This has far-reaching consequences for both the vertical and lateral distribution of nutrient, sediments, pollutants and heat.

5.6 Conclusions

A simple polynya model driven by standard atmospheric forcing has been used to estimate ice production during an exceptionally strong WNS polynya event in February 2004. The ability of the polynya to form dense shelf bottom water was investigated by adding the brine released during the polynya event to the average winter density stratification of the water body preconditioned by summers with a cyclonic atmospheric forcing. The model performance was

also tested by applying it to the simulation of a well documented WNS polynya event in April 2008.

The simulation of the opening event in 2008 shows that the model is capable of reproducing correctly the extent of the open water zone and the location of the pack ice edge. The good agreement between simulated thickness of the thin ice zone and estimates made by airborne surveys and AVHRR satellite indicates that the model is well tuned, and suggests that the approach is a suitable tool to investigate the dynamics and export rates of flaw polynyas. Owing to a number of biases in the representation and parameterization of physical processes in the model, ice production and salt rejection is overestimated. Applying the model to the strong polynya event in 2004, results in a total ice volume production of 26 km^3. This corresponds to a brine release of 2.9×10^{11} kg. Neglecting the replenishment of water masses by advection into the polynya area, the likelihood of convective mixing down to the bottom is extremely low. The strength of the density stratification and the noticeable lack of polynya extreme events in the eastern Laptev Sea limit convective mixing to a depth of 20 m or less. This assumption is further supported by mooring based observations in the WNS polynya that show that large polynya openings are usually associated with a decrease in near-bottom water salinity and temperature at water depth greater than 25 m, which is predominantly related to wind- and tidally-driven turbulent mixing of the water column. This (the absence of convective mixing down to the seabed and subsequent dense water formation) has far reaching consequences on the today's understanding of energy and matter transport on the eastern Laptev Sea shelf.

Understanding how the stratification of shallow shelf water and the ice production and salt rejection in polynyas might change in a warming climate is one of the major challenges of current polar research. On the one hand, it is likely, that the stability of the halocline will be strengthened by an increase in Siberian river discharge (Bethke and others, 2006; Peterson and others, 2006). Rising Arctic surface temperatures (Chapman and Walsh, 2007) will probably weaken ice production and increase summer sea ice melt, further promoting the stability of the halocline. On the other hand, the observed positive trend in summer cyclonicity over the Eurasian Arctic (Simmonds and others, 2008; Simmonds and Keay, 2009) might destabilize the water column (change the water-column structure). Likewise, a decrease in ice production could be compensated by an increase in polynya activity during the freeze-up period and in early spring (Willmes and others, 2010a) caused by an increase in the frequency and strength of cyclones penetrating into the Eurasian Arctic (Zhang and others, 2004).

Clearly, we are far from being able to formulate sound predictions of how polynya formation

and water column stratification will respond to climatic change. Understanding and quantifying this response are key tasks for future shelf process studies. To draw inferences on the physical behavior of polynyas - under the premise that the climate in the Arctic is changing - a numerical approach is needed. Nevertheless, our results show that an alteration of mechanisms responsible for vertical mixing in the WNS polynya would require a strong increase in ice production and/or a significant weakening of the year-round density stratification.

5.7 Acknowledgments

This work was carried out as part of the German-Russian cooperation 'System Laptev Sea', funded by the BMBF under grant 03G0639A and the Alfred Wegener Institute. ENVISAT satellite data and AVHRR images were obtained through ESA Project EO-500 'Formation, transport and distribution of sediment-laden sea ice in the Arctic Shelf seas' and the U.S. National Oceanic and Administration (NOAA) Comprehesive Large Array data Stewardship System (CLASS), respectively. Thanks to the Arctic and Antarctic Research Institute (AARI) for the provision of the hydrographic dataset, the German Aerospace Center (DLR) for the provision of the TerraSAR-X imagery (grand COA0388) and the German Federal Ministry of Economics and Technology (BMWi) for their support. The authors also very much appreciate the comments and suggestions made by Sergey Kirillov from the AARI.

6

Summary and concluding remarks

The Laptev Sea is considered as one of the most significant sites of net ice production in the Arctic Ocean. Much of this ice is generated in extensive flaw polynyas extending almost 2000 km along the Laptev Sea shelf and landfast sea ice. When ice is formed in polynyas, salt is expelled, and added to the water body. If ice formation is strong enough, the downward precipitation of brine causes thermohaline convection and temporarily erodes the density stratification of the water column. However, the few existing studies on ice formation rates in polynyas show large differences in ice flux estimates. Consequently, little is known about the role of Laptev Sea polynyas for shelf water mass modification.

Understanding vertical mixing and convection processes in coastal polynyas is important, since they affect momentum, heat and biogeochemical air-sea fluxes (Morales Maqueda and others, 2004). According to Dmitrenko and others (2005), the hydrography in the eastern Laptev Sea and in the area of the Western New Siberian (WNS) polynya (Figure 1.2) is controlled by large summer run-off of the Lena river leading to the development of a strong vertical density gradient in the water column. Owing to the strong stratification and a lack of distinct polynya events (Winsor and Bjoerk, 2000), our hypothesis was that ice production alone in the WNS polynya is not high enough to erode the halocline and to form dense shelf bottom water.

Thus, the aim of this thesis is to further investigate the effect of ice production and salt rejection taking place during strong polynya opening events in the eastern Laptev Sea on the stratification of the water body beneath. The performance of different satellite-based methods and a model to examine polynya dynamics and subsequent fluxes is tested to find the most appropriate approach to prove the hypothesis.

Passive microwave satellites allow for a direct deduction of polynya area, and together with atmospheric data, a retrieval of thin ice thickness and ice production. With their global coverage

and their ability to penetrate cloud cover, passive microwave sensors can be used for long-term and large-scale monitoring of polynya dynamics and associated ice formation (Willmes and others, 2010a; Kern, 2009; Tamura and others, 2007). But accurate ice production estimates require stable methods to detect the area of open water as well as growth, thickness and evolution of thin ice.

We therefore examine different parameters and methods to observe polynya area (POLA, open water and thin ice area) and thin ice thickness (hi) by a combination of multi-sensor satellites. The cross-validation is made on the basis of a prominent WNS polynya event, observed during the TRANSDRIFT (TD) XIII expedition in late April, 2008. The POLA is derived from the Polynya Signature Simulation Method (PSSM, Renfrew and others, 2002; Arrigo and van Dijken, 2004; Kern, 2009) which provides a classification of thin ice and open water areas. The method uses microwave brightness temperature (TB) data from the SSM/I sensor and AMSR-E/Aqua and is based on the sensitivity of passive microwave polarization ratios to thin ice and open water. The thickness of the thin ice zone is also obtained from passive microwave polarization ratios. The accuracy of the used POLA and hi methods is assessed by thermal infrared Advanced Very High Resolution Radiometer (AVHRR) ice thickness estimates (hi_{TH}) and airborne electromagnetic (EM) ice thickness measurements (hi_{HEM}) obtained during the TD XIII expedition. As this study presents a cross-validation, no truth reference data are declared. Nevertheless, we consider hi_{TH} and hi_{HEM} as most accurate among the presented data, simply because they provide the highest spatial resolution and were successfully applied in previous studies (Yu and Lindsay, 2003; Drucker and others, 2003; Kern and others, 2007; Pfaffling and others, 2007). In addition, Environmental Satellite (ENVISAT) SAR images and aerial photographs are used for the cross-validation. The aerial photographs were taken simultaneously with the HEM flights by the newly developed HELicopter-borne Ice Observation System (HELIOS). Images are used to retrieve information about the spatial distribution of open water patches, compression such as rafting or ridging and the presence of snow on top of the ice. The performance of HELIOS was tested by means of accuracy analysis and case studies (Krumpen and others, 2010a).

As shown in our study, inaccuracies in the satellite-derived thin ice thickness arise from the influence of mixed water, thin and thick ice signals at the polynya edge when coarse resolution passive microwave data ($\geq 5\times 5$ km^2) are used. In particular, in long and narrow flaw polynyas, where the fraction of non-edge pixels is comparably small, the influence of microwave signals from the fast and pack ice becomes a major source of error in the thickness retrieval. Hence, with decreasing polynya width, the spatial resolution of the input data becomes increasingly important. The use of enhanced resolution data products indicates potential for a significant

improvement of thin ice monitoring. In the presented case study hi_{R89}, $hi_{R36(SIR)}$ and $hi_{QR(SIR)}$ reasonably depicted the across-polynya ice thickness increase as indicated by HEM measurements and thermal infrared AVHRR ice thickness estimates, while the accuracy of thin ice retrieval from 36 GHz, 37 GHz and 85 GHz TB channels is significantly reduced by their low spatial resolution.

We conclude that hi estimates need to account for regional particularities of polynya size and shape. Unfortunately, the retrieval of polynya area by means of PSSM is very sensitive to applied thresholds if used in narrow flaw polynyas and can easily be underestimated by as much as 50 %. Our results imply that previously suggested algorithms for the regional-scale detection of thin ice thickness from microwave data are not necessarily transferable to the Laptev Sea. Passive microwave data as well as parameterizations used in the applied methods have to be carefully assessed to avoid large errors due to regional peculiarities.

Alternatively, flux models can be used to simulate polynya evolution and associated ice fluxes. Flux models calculate the location of transition between open water and thin ice from the balance between the flux of frazil ice produced in the open water area and the wind-driven offshore divergence of consolidated new ice.

The performance of a two-dimensional flux model is tested through the simulation of an 11 day Anabar-Lena (AL) polynya event that took place in the southern Laptev Sea in late December, 2007. The model was developed by Morales Maqueda and Willmott (2000) and modified such that it computes associated ice and salt fluxes. Results are then compared to ice thickness and ice production estimates derived from high-resolution thermal infrared MODIS observations in conjunction with an atmospheric dataset. The thermal approach is limited to clear sky conditions, but yields good results for ice thicknesses below 0.5 m (Willmes and others, 2010b).

An initial comparison of thermal infrared MODIS imagery and SAR observations with model computations has shown that the flux model is capable of reproducing quite well the shape of the polynya and salient features of the landfast ice boundary using only a few simple conservation laws. If a realistic fast ice boundary and parameterization of the collection depth H is used and if the movement of the pack ice edge is prescribed correctly, results from this model are in agreement with satellite estimated ice thickness and production estimates.

MODIS based estimates and the flux model calculation yield an accumulated ice production of 1.3 m and 1.2 m per unit area in the area near the fast ice edge over a period of 11 days. In the thin ice area further offshore, ice formation rates are higher in the model, which results from lower ice thickness estimates. The mean accumulated ice production per unit area is 0.4

m, both for MODIS and model results. The largest local deviations in ice production estimates coincide with areas of high disparity between simulated and thermal infrared thickness.

Regional differences between satellite estimates and model results are predominantly related to the representation of physical processes in the model, such as the missing representation of the effect of ocean currents on frazil ice trajectories and dynamic thickening of thin ice, namely rafting.

We conclude that these simplified physical polynya models are valuable tools for studying polynya dynamics and estimating associated fluxes of single polynya events and provide a better alternative to passive microwave polynya monitoring techniques.

Thus, a flux model is used to examine the effect of ice formation on the structure of the water column in the area of the WNS polynya. Since we found that regional differences in ice production and ice thickness estimates are mostly due to the missing representation of dynamic thickening in flux models (Krumpen and others, 2010c), the model applied in Krumpen and others (2010b) is a more simple 1-dimensional approach that contains a parameterization for the effect of rafting in the thin ice zone.

With the model we then simulate an extremely strong opening event of the WNS polynya lasting for a period of 27 days, starting on February 10, 2004. The water body was pre-conditioned toward a weak stratification state by a cyclonic atmospheric circulation regime during summer 2003. The ability of the polynya to form dense shelf bottom water is judged by integrating the amount of salt rejection over the weakly stratified water column.

Prior to the simulation of the major polynya opening event observed in 2004, the model performance is tested by simulating the minor but rather well documented opening event observed during TD XIII in April, 2008 (Willmes and others, 2010b). The comparison of computed open water width with observations made by helicopter, high-resolution TerraSAR-X scenes and ENVISAT SAR images has shown that the flux model is capable of reproducing correctly the location of the transition between open water and thin ice. Moreover, the agreement between the simulated thin ice thickness and HEM and thermal infrared AVHRR ice thickness estimates is good. The model slightly underestimates the HEM and AVHRR estimates and consequently overestimates ice production. In total, an ice volume of 1.3 km^3 is formed and 0.14×10^{11} kg of salt rejected between April 27 and May 01, 2008. Assuming advection to be negligible and the absence of stratification, the salinity of the open water zone, which has a depth of 25 m, would increase by approximately 1.0 psu.

Applying the model to the simulation of the strong polynya event in 2004 the total amount results in an ice volume production of 26 km^3. A comparison of our calculations with seasonal ice production estimates made in the literature confirms the 2004 event as an exceptionally strong one. The total amount of salt rejected during the polynya event was estimated to be about 2.9 $\times 10^{11}$ kg, of which 1.5 $\times 10^{11}$ kg were rejected in the open water area as frazil ice was created.

The agreement between simulated evolution of the pack ice edge and satellite observations is again high. However, because no aerial observation exists for the 2004 event and the edge of the open water region is not easily identifiable in SAR scenes, a validation of the simulated open water width is difficult. Nevertheless, we have confidence in our simulation of the open water evolution, as it was proven to be rather accurate for the well documented 2008 event.

Adding the computed release of brines from freezing sea ice to the average winter density stratification and neglecting any horizontal advection of dense water, salt rejection would convectively erode the halocline down to a depth of 20 m. The destratification in our simulations is favored in a number of ways. All calculations were made on the basis of a weakly stratified water column, pre-conditioned for destratification by cyclonic summers and an exceptionally strong polynya event. Moreover, the model tends to overestimate ice production, since the atmospheric dataset used for the simulation of the 2004 event, does not incorporate the impact of the polynya on the atmospheric boundary layer. In addition, ocean currents, replenishing eroded water masses and helping to restore stratification, are neglected. Hence, the calculated mixed layer depths can be considered as an upper bound estimate of the destratification potential, which further supports our hypothesis that even during strong polynya events ice production is not high enough to erode the halocline and that the ability of the polynya to form dense shelf bottom water is extremely low. Our results provide indirect evidence that the mechanisms responsible for vertical mixing in the area around the WNS polynya are predominantly wind- and tidally driven, rather than convective. This has far-reaching consequences for both the vertical and lateral distribution of nutrients, sediments, pollutants and heat.

Moreover, the model simulations emphasize the importance of isolated extreme events for the net sea ice formation in the Laptev Sea. For example, during the strong event simulated in Krumpen and others (2010b) 26 km^3 of ice was produced. Putting our estimates in relation to the annual polynya ice production estimated by Winsor and Bjoerk (2000) and Willmes and others (2010a), approximately 50 % was produced during a single WNS polynya event. This is euqivalent to 3 % of the annual net sea ice production in the entire Laptev Sea (900 km^3, see Introduction). How often these extreme events occur is an issue that needs to be

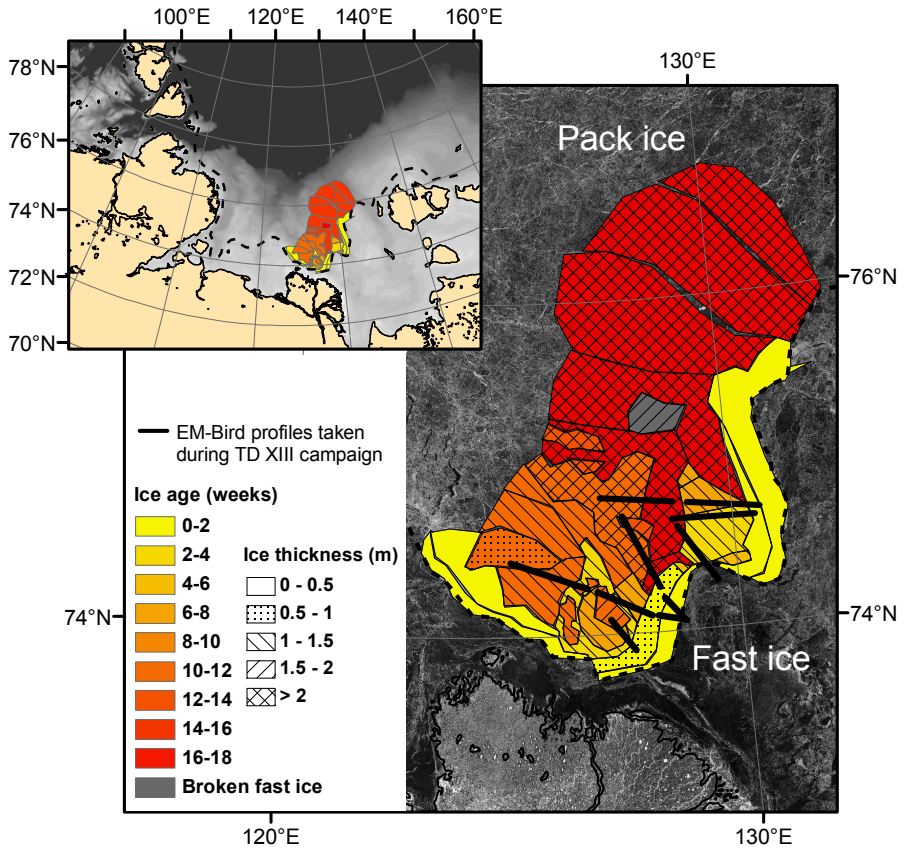

Figure 6.1: Thickness and age of ice produced in the WNS polynya in winter 2008. Based on ENVISAT SAR images, ice areas produced during polynya events prior April 25, 2008 were tracked and classified according to their age of formation (color code). Electromagnetic (EM) helicopter-borne ice thickness measurements made during the TRANSDRIFT (TD) XIII campaign at end of April, 2008 (black lines) were used to determine the mean ice thickness of individual ice zones (texture: dots and hatches). Together with the areal information, EM measurements can be used to quantify the ice volume that has been produced inside polynyas.

addressed in future studies.

In section (1.3, The Laptev Sea), it was shown that large discrepancies exist in the literature with respect to the contribution of polynyas to the annual net sea ice formation in the Laptev Sea. It was argued that existing discrepancies might be a consequence of the use of different sensor systems, models, observation periods and alternating definitions for the term 'active polynya'. In this thesis, we investigate exclusively ice formation rates in single polynya events. Hence, presented results cannot be used to quantify the contribution of polynyas to the annual ice production in the Laptev Sea. Nevertheless, we have shown that passive microwave satellites, if applied to narrow polynyas, underestimate ice production and polynya area (Willmes and others, 2010b). In particular polynyas with narrow open water zones, formed under moderate or low

wind forcing and extremely low temperatures, are not resolved by passive microwave satellites. Note that passive microwave data reveal no or only minor polynya activity for the events simulated in Krumpen and others (2010c) and Krumpen and others (2010b). Consequently, our results imply that the contribution of polynyas to the net sea ice formation in the Laptev Sea is indeed higher than passive microwave studies suggest. This finding is in agreement with polynya area estimates obtained manually from ENVISAT SAR imagery. According to SAR scenes acquired during winter 2008, an ice area of 51×10^3 km^2 (10 % of the entire Laptev Sea area) was produced in the WNS polynya between December and April (Fig. 6.1), which is this is twice as much as ice area estimates made by Winsor and Bjoerk (2000) and Willmes and others (2010b).

However, coupled ice-ocean models and newly launched satellites such as the Soil Moisture Ocean Salinity (SMOS) mission and CryoSat-2 capable of measuring the thickness of sea ice from space (see section 7, Future scope), need accurate annual polynya ice production estimates as a reference for satellite and model validation. Together with EM-Bird ice thickness measurements, polynya area estimates obtained from ENVISAT SAR images can be used to quantify accurately seasonal ice export and production rates. Figure (6.1) shows the ice areas that were formed in the WNS polynya between December and April, 2008. Ice thickness information obtained from the EM-Bird made during the TD XIII campaign at the end of April were used to assign a mean ice thickness to individual ice areas. The approach yields a total ice volume of 81 km^3 that originates from polynyas in the eastern Laptev Sea (9 % of the total net annual ice formation in the Laptev Sea).

7

Future scope

Polynyas are well recognized as strong ice producers and might gain special attention regarding ice volume changes in the Arctic (Morales Maqueda and others, 2004; Willmott and others, 2007). Understanding how the stratification of shallow shelf water and the ice production and salt rejection in polynyas might change in a warming climate is one of the major challenges of current polar research. On the one hand, it is likely, that the stability of the halocline will be strengthened by an increase in the Siberian river discharge (Bethke and others, 2006; Peterson and others, 2006). Rising Arctic surface temperatures (Chapman and Walsh, 2007) will probably weaken ice production and increase summer sea ice melt, further promoting the stability of the halocline. On the other hand, the observed positive trend in summer cyclonicity over the Eurasian Arctic (Simmonds and others, 2008; Simmonds and Keay, 2009) might destabilize the water column (change the water-column structure). Likewise, a decrease in ice production could be compensated by an increase in polynya activity during the freeze-up period and in early spring (Willmes and others, 2010a) caused by an increase in the frequency and strength of cyclones penetrating into the Eurasian Arctic (Zhang and others, 2004).

Clearly, we are far from being able to formulate sound predictions of how polynya formation and water column stratification will respond to climate change. Nevertheless, our results show that an alteration of mechanisms responsible for vertical mixing in the WNS polynya would require a strong increase in ice production and/or a significant weakening of the year-round density stratification.

Understanding and quantifying a response to climate change are key tasks for future shelf process studies. Unfortunately, the presented flux models can only be used to explicitly simulate single event. In order to draw inferences on the physical behavior of polynyas - under the premise that the climate in the Arctic is changing - a coupled climate model is needed.

The prescribed task will be investigated, together with the University Trier, by an atmospheric model (COnsortium for Small-scale Modeling, COSMO) coupled to the Finite Element Sea ice-Ocean Model (FESOM, Timmermann and others, 2009). For validation of model simulations, polnya flux models might provide a suitable reference dataset. The main reason for pursuing the polynya flux model approach concerns the parameterisation of dense water production within polynyas not resolved by coarse resolution coupled ocean-sea ice models. Furthermore, it is easier to identify the dominant physical processes operating throughout the evolution of the polynya area, since these simplified models have their strength in isolating the basic polynya processes.

A drawback of current sea ice-ocean coupled models is the missing or deficient representation of fast ice. However, correct representation of the fast ice edge is important since it controls the position, shape and dynamic of the polynya and hence, the area where water mass modification takes place. If the fast ice is neglected, the modelled polynya location is shifted towards the coastline. Following Adams and others (2010) and Rozman and others (2010), the implementation of a fast ice mask in FESOM and the North Atlantic/Arctic Ocean-Sea Ice Model (NAOSIM) results in more realistic polynya estimates. In this study, information on the seasonal variability and extent of the fast ice were extracted manually from high resolution satellite products on a monthly basis. Simulating polynya evolution on a longer time scale would require an automatic procedure to derive fast ice edges in the marginal seas of the Arctic Ocean. Whether sea ice drift and concentration products retrieved from passive microwave satellites together with information from high-resolution RADAR satellites can be used to obtain a realistic fast ice parameterization for the implementation in sea ice-ocean coupled models is another outstanding topic that needs to be addressed in future studies.

The presented comparison of different satellite-based methodologies to obtain information about polynya area and thickness evolution and associated salt fluxes gives an interesting new insight in the applicability and performance of these approaches. However, in the last two years, new satellites for polar application were developed. For example, the Soil Moisture and Ocean Salinity (SMOS) satellite, that was launched in November 2009, has the potential to estimate sea ice thickness from sea ice brightness temperature measured at 1.4 GHz (Heygster and others, 2009; Kaleschke and others, 2009). The MIRAS instrument on the SMOS satellite provides daily coverage of the complete polar seas with a resolution of about 35 km in nadir view. The resolution is of course too low to observe leads or polynyas, but could provide measurements and monitoring of extensive thin ice regions in Laptev Sea polynyas.

The accuracy of SMOS ice thickness estimates has not been quantified yet. In the framework of

the SMOS Sea Ice Retrieval Study (SMOSIce) the AWI sea ice physics group will therefore conduct EM ice thickness measurements in polynya areas of the Laptev Sea in March/April 2011 (TD XVII). Together with thickness information obtained from thermal infrared satellites and areal ice formation estimates made on the basis of SAR scenes (Figure 6.1), the data will be used for SMOS product validation. After the validation has been completed, the ability of SMOS derived ice thickness estimates for long-term monitoring and characterization of thin ice zones in polynyas will be assessed.

List of Figures

List of Tables

Bibliography

Aagaard, K. and E. C. Carmack, 1989. The role of sea ice and other fresh water in the arctic circulation, *Journal of Geophysical Research*, **94**(C10), 14485–14489.

Aagaard, K., L. K. Coachman and E. Carmack, 1981. On the halocline of the Arctic Ocean, *Deep Sea Research*, **28A**, 529–545.

Aagaard, K., J. H. Swift and E. C. Carmack, 1985. Thermohaline circulation in the Arctic Mediterranean seas, *Journal of Geophysical Research*, **90**, 4833–4846.

Adams, S., S. Willmes, T. Krumpen, J. Hoelemann and G. Heinemann, 2010. Thin ice thickness retrieval within the Laptev Sea Polynya from high-resolution ice surface temperatures.

Alam, A. and J. A. Curry, 1995. Lead-induced atmospheric circulations, *Journal of Geophysical Research*, **100**, 4643–4651.

Alexandrov, V., T. Martin, J. Kolatschek, H. Eicken and A. P. M. Kreyscher, Makshtas, 2000. Sea ice circulation in the Laptev Sea and ice export to the Arctic Ocean: Results from satellite remote sensing and numerical modeling, *Journal of Geophysical Research*, **105**(C7), 17143–17159.

Arrigo, K. R., 2005. Marine micro-organisms and global nutrient cycles, *Nature*, **437**(7057), 349.

Arrigo, K. R. and G. L. van Dijken, 2004. Phytoplankton dynamics within 37 Antarctic coastal polynya systems, *Journal of Geophysical Research*, **108**(C8), 3271.

Ashcroft, P. and F. Wentz, 2008. AMSR-E/Aqua L2A global swath spatially-resampled brightness temperatures, *Digital media V001*, National Snow and Ice Data Center, Boulder, Colorado, USA.

Babko, O., D. A. Rothrock and G. A. Maykut, 2002. Role of rafting in the mechanical redistribution of sea ice thickness, *Journal of Geophysical Research*, **107**(C8), 2701–2714.

Backhaus, J. A., H. Fohrmann, J. Kaempf and A. Rubina, 1997. Formation and export of water masses produced in Arctic shelf polynyas - process studies of oceanic convection, *Journal of Marine Science*, **54**, 366–382.

Barber, D. G. and R. A. Massom, 2007. The Role of Sea Ice in Arctic and Antarctic Polynyas. In: Polynyas: Windows to the world, Elsevier Oceanography Series, Amsterdam, Netherlands.

Barber, D. G., J. J. Yackel and J. M. Hanesiak, 2001. Sea Ice, RADARSAT-1 and Artic Climate Processes: A Review and Update, *Canadian Journal of Remote Sensing*, (16), 51–61.

Bareiss, J. and K. Goergen, 2005. Spatial and temporal variability of sea ice in the Laptev Sea: Analysis and review of satellite passiv-microwave data and model results, 1997 to 2002, *Global and Planetary Change*, **48**, 28–54.

Barnea, S., Z. Shragai, Z. Suliman and M. Yalon, D. ad Shechter, 2009. Mapping Remote Areas with a Portable High-Accuracy Photogrammetric System, Surveyors Key Role in Accelerated Development, FIG Working Week, Eilat, Israel.

Barrie, L., E. Falck, G. Dennis, T. Iversen, H. Loeng, R. Macdonald, S. Pfirman, T. Skotvold and E. Wartena, 1998. The Influence of Physical and Chemical Processes on Contaminant Transport into and within the Arctic, *Assessment report*, Arctic Monitoring and Assessment Programme (AMAP), Oslo, Norway.

Barry, R. G., M. C. Serreze, J. A. Maslanik and R. H. Preller, 1993. The Arctic Sea Ice-Climate System: Observations and modeling, *Reviews of Geophysics*, **31**(4), 397–422.

Bethke, I., T. Furevik and H. Drange, 2006. Towards a more saline North Atlantic and a fresher Arctic under global warming, *Geophysical Research Letters*, **33**.

Biggs, N. R. T., M. A. Morales Maqueda and A. J Willmott, 2000. Polynya flux model solutions incorporating a parameterisation for the collection thickness of consolidated new ice., *Journal of Fluid Mechanics*, **408**, 179–204.

Brandon, M., F. Cottier, T. Nilsen and G. Dieckmann, 2010. Sea Ice and Oceanography, Wiley-Blackwell, Oxford, UK, 2 ed.

Budikova, D., 2009. Role of Arctic sea ice in global atmospheric circulation: A review, *Global and Planetary Change*, **68**, 149–163.

Busche, T., I. Hajnsek, T. Krumpen, J. Rabenstein, L. Hoelemann, C. Haas and S. Willmes, 2009. Investigating Coastal Polynya Thin Sea Ice State in the Laptev Sea Using TerraSAR-X Dual-Pol Stripmap Data, IGARSS 2009 Conference Proceedings, IEEE.

Bushuyev, A. V., N. A. Volkov and Loschilov V. S., 1964. Physical-geographical Characteristics of Ice Cover of the Arctic Basin and Marginal Seas, AARI Archives.

Buzov, A. Y., 1991. The Northern Sea Route Project -Natural factors and their influence on transit sailing on the Northern sea Route - Part I, *Pilot studies report*, The Fridtjof Nansen Institute, Oslo, Norway.

Cavalieri, D. J. and S. Martin, 1994. The contribution of Alaskan, Siberian, and Canadian coastal polynyas to the cold halocline layer of the Artic Ocean, *Journal of Geophysical Research*, **99**(C9), 18343–18362.

Chapman, W. M. and J. E. Walsh, 2007. Simulations of Arctic Temperature and Pressure by Global Coupled Models, *Journal of Climate*, **20**.

Colony, R. and A. S. Thorndike, 1985. Sea ice motion as a drinkard's wal, *Journal of Geophysical Research*, **90**, 965–974.

Comiso, J. C., 2003. Large-scale characteristics and variability of global sea ice cover: Sea ice, An introduction to its physics, chemistry, biology and geology, vol. 1, Blackwell Publishing, New York, US.

Comiso, J. C., 2010. Variability and Trends of the Arctic Sea Ice Cover: Sea Ice, vol. 2, Wiley-Blackwell, New York, US.

Darby, M. S., A. J. Willmott and L. A. Mysak, 1994. A Nonlinear Steady-State Model of the North Water Polynya, Baffin Bay, *Journal of Physical Oceanography*, **24**(5), 1011–1020.

Darby, M. S., A. J. Willmott and T. A. Somerville, 1995. On the influence of coastline orientation on the steady state width of a latent heat polynya, *Journal of Geophysical Research*, **100**(C7), 13625–13634.

Dethleff, D., P. Loewe and E. Kline, 1998. The Laptev Sea flaw lead - Detailed investigation on ice formation and export during 1991/1992 winter season, *Cold Region Science and Technology*, **27**, 225–243.

Dmitrenko, I. A., V. A. Gribanov, D. L. Volkov, H. Kassens and H. Eicken, 1999. Impact of river discharge on the fast ice extension in the Russian Arctic shelf area, *Tech. Rep. 1*, Proceedings

of the 15th International Conference on Port and Ocean Engineering under Arctic Conditions (POAC99), Helsinki, 23-27 August.

Dmitrenko, I. A., S. A. Kirillov, T. Krumpen, J. A. Hölemann, H. Kassens, M. Makhotin, P. Abrahamsen, E. Bloshkina and C. Wegner, 2010a. Wind-driven diversion of summer river runoff preconditions the Laptev Sea coastal polynya hydrography: Evidence from summer-to-winter hydrographic records of 2007-2009, *Continental Shelf Research*, **in press**.

Dmitrenko, I. A., S. A. Kirillov, L. B. Tremblay, D. Bauch and S. Willmes, 2009. Sea-ice production over the Laptev Sea shelf inferred from historical summer-to-winter hydrographic observations of 1960s-1990s, *Geophysical Research Letters*, **36**.

Dmitrenko, I. A., K. N. Tyshko, S. A. Kirillov, H. Eicken, J. A. Hoelemann. and H. Kassens, 2005. Impact of flaw polynyas on the hydrography of the Laptev Sea, *Global and Planetary Change*, **48**, 9–27.

Dmitrenko, I. A., C. Wegner, H. Kassens, S. A. Kirillov, T. Krumpen, G. Heinemann, A. Helbig, D. Schroeder, J. A. Hoelemann, T. Klagge, K. P. Tyshko and T. Busche, 2010b. Observations of supercooling and frazil ice formation in the Laptev Sea coastal polynya, *Journal of Geophysical Research*, **115**(C05015).

Dokken, S. T., P. Winsor, T. Markus, J. Askne and G. Bjork, 2002. ERS SAR characterization of coastal polynyas in the Arctic and comparison with SSM/I and numerical model investigation, *Remote Sensing of Environment*, **80**, 321–335.

Drucker, R., S. Martin and R. Moritz, 2003. Observation of ice thickness and frazil ice in the St. Lawrence Island polynya from satellite imagery, upward looking sonar, and salinity/temperature moorings, *Journal of Geophysical Research*, **108**(C5), 1810–1817.

Druee, C. and G. Heinemann, 2004. High-resolution maps of the sea-ice concentration from MODIS satellite data., *Geophysical Research Letters*, **31**(L20403).

Early, D. S. and D. G. Long, 2001. Image Reconstruction and Enhanced Resolution Imaging from Irregular Samples, *IEEE Transactions on Geoscience and Remote Sensing*, **39**(2), 91–302.

Ebner, L., D. Schreoder and G. Heinemann, 2010. Impact of Laptev Sea flaw polynyas on the atmospheric boundary layer and ice production using idealized mesoscale simulations, *Polar Research*, **in press**.

Eicken, H., I. A. Dmitrenko, K. Tyshko, A. Darovskikh, W. Dierking, U. Blahak, J. Groves and H. Kassens, 2005. Zonation of the Laptev Sea landfast ice cover and its importance in a frozen estuary, *Global and Planetary Change*, **48**, 55–83.

Gloersen, P., W. J. Campbell, D. J. Cavalieri, J. Comiso and C. Parkinson, 1992. Arctic and Antarctic Sea-Ice, 1978-1987: Satellite Passive-Microwave Observations and Analysis, NASA Spec. Publ.

Haarpaintner, J., M. Haugan and J. Gascard, 2001. Interannual variability of the Storfjorden (Svalbard) ice cover and ice production observed by ERS-2 SAR, *Annals of Glaciology*, **33**(C7), 430–436.

Haas, C., J. Lobach, S. Hendricks, L. Rabenstein and A. Pfaffling, 2009. Helicopter-borne measurements of sea ice thickness, using a small and lightweight, digital EM system, *Journal of Applied Geophysics*, **67**(3), 234–241.

Haas, C., A. Pfaffling, S. Hendricks, L. Rabenstein, Etienne J. L. and I. Rigor, 2008. Reduced ice thickness in Arctic Transpolar Drift favors rapid ice retreat, *Geophysical Research Letters*, **35**(L17501).

Hall, R. T. and D. A. Rothrock, 1987. Photogrammetric Observations of the Lateral Melt of Sea Ice Floes, *Journal of Geophysical Research*, **92**, 7045–7048.

Heygster, G., S. Hendricks, L. Kaleschke, N. Maaß, P. Mills, D. Stammer, R. Tonboe and C. Haas, 2009. L-Band Radiometry for Sea-Ice Applications, *Final report for ESA*, SMOSIce Project.

Hoelemann, J. A., S. Kirillov, T. Klagge, A. Novikhin, H. Kassens and L. Timokhov, 2010. Near-bottom water warming in the Laptev Sea in response to atmospheric and sea ice conditions in 2007, *Polar Research*, **submitted**.

Ivanov, V. V. and P. N. Golovin, 2007. Observations and modeling of dense water cascading from the northwestern Laptev Sea shelf, *Journal of Geophysical Research*, **112**.

Johannessen, O. M., V. Yu, I. Alexandrov, Y. Frolov, S. Sandven, M. Miles, L. P. Bobylev, L. H. Pettersson, V. G. Smirnov and E. U. Mironov, 2005. Remote Sensing of Sea Ice in the Northern Sea Route: Studies and Applications, Springer Praxis Books.

Kaleschke, L., C. Lüpkes, T. Vihma, J. Haarpaintner, A. Bochert, J. Hartmann and G. Heygster, 2001. SSM/I Sea Ice Remote Sensing for Mesoscale Ocean-Atmosphere Interaction Analysis, *Canadian Journal of Remote Sensing*, **27**, 526–537.

Kaleschke, L., N. Maaß, C. Haas, S. Hendricks, G. Heygster and R. T Tonboe, 2009. A sea ice thickness retrieval model for 1.4 GHz radiometry and application to airborne measurements over low salinity sea ice, *The Cryosphere Discussion*, **3**, 995–1022.

Kanamitsu, M., W. Ebisuzaki, J. Woollen, S. K. Yang, J. J. Hnilo, M. Fiorino and G. L. Potter, 2002. NCEP-DOE AMIP-II Reanalysis (R-2), *Bulletin of the American Meteorological Society*, **83**(3), 1631–1643.

Kasser, M. and Y. Egels, 2002. Digiatl Photogrammetry, Taylor and Francis, London.

Kern, S., 2008. Polynya area in the Kara Sea, Arctic, obtained with microwave radiometry for 1979-2003, *Geoscience and Remote Sensing Letters, IEEE*, **5(2)**, 171–175.

Kern, S., 2009. Wintertime Antarctic coastal polynya area: 1992-2008, *Geophysical Research Letters*, **36**(L14501).

Kern, S., I. Harms, S. Bakan and Y. Chen, 2005. A Comprehensive View of Kara Sea Polynya Dynamics, Sea-Ice Compactness and Export from Model and Remote Sensing Data, *Geophysical Research Letters*, **32**(15), L15501.

Kern, S., G. Spreen, L. Kaleschke, S. De La Rosa and G. Heygster, 2007. Polynya Signature Simulation Method polynya area in comparison to AMSR-E 89 GHz sea-ice concentrations in the Ross Sea and off the Adélie Coast, Antarctica, for 2002-2005: first results, *Annals of Glaciology*, **46**(1), 409–418.

Key, J. R., J. B. Collins, C. Fowler and R. S. Stone, 1997. High-Latitude Surface Temperature Estimates from Thermal Satellite Data, *Remote Sensing of Environment*, **61**, 302–309.

Koeberle, C. and R. Gerdes, 2003. Mechanisms Determining the Variability of Arctic Sea Ice Conditions and Export, *Journal of Climate*, **16**(17), 2843–2858.

Kotchetov, S. V., V. K. Kulakov, L. A. Kurajov, Timokhov Y. and A. Vanda, 1994. Hydrometeorological regime of the Laptev Se, *Tech. rep.*, Federal Service of Russia for Hydrometeorology and Monitoring of the Environment, Arctic and Antarctic Research Institute, St. Petersburg, Russia.

Krumpen, T., C. Haas, S. Hendricks, J. Hoelemann, R. Gerdes and D. Kalmbach, 2010a. HELIOS, a nadir-looking sea ice monitoring camera, *Cold Region Science and Technology*, **submitted**.

Krumpen, T., J. A. Hoelemann, S. Willmes, M. A. Morales Maqueda, T. Busche, I. A. Dmitrenko, R. Gerdes, C. Haas, S. Hendricks, S. Kirillov, L. Rabenstein and D. Schroeder, 2010b. Sea ice

production and water mass modification in the eastern Laptev Sea, *Journal of Geophysical Research*, **submitted**.

Krumpen, T., S. Willmes, M. A. Morales Maqueda, R. Gerdes, C. Haas, J.. Hoelemann and D. Schroeder, 2010c. Verification of a polynya flux model by means of thermal infrared satellite observations, *Annals of Glaciology*, **submitted**.

Kvambekk, A. S. and T. Vinje, 1993. The ice transport through Fram Strait, paper presented at the Nansen Centennial Symposium, Bergen, Norway.

Kwok, R., J. C. Comiso and R. Martin, S. Drucker, 2007. Ross Sea polynyas: Response of ice concentration retrievals to large areas of thin ice, *Journal of Geophysical Research*, **112**(C12012).

Kwok, R., G. F. Cunningham, M. Wensnahan, I. Rigor, H. J. Zwally and D. Yi, 2009. Thinning and volume loss of the Arctic Ocean sea ice cover: 2003-2008., *Journal of Geophysical Research*, **114**(C07005).

Kwok, R. and D. A. Rothrock, 2009. Decline in Arctic sea ice thickness from submarine and ICESat records: 1958-2008, *Geophysical Research Letters*, **36**(L15501).

Laebe, T. and W. Foerster, 2004. Geometric Stability of Low-Cost Digital Consumer Cameras., International Archives of ISPRS, ISPRS Congress, Istanbul, vol. 35, 528–535.

Lebedev, V. L., 1968. Maximum size of a wind-generated lead during sea freezing, *Oceanology*, **8**, 313–318.

Leisti, H., Riska. K., I. Heiler, P. Eriksson and J. Haapala, 2009. A method for observing compression in sea ice fields using IceCam , *Cold Region Science and Technology*, **59**, 65–77.

Lenn, Y. D., P. J. Wiles, S. Torres-Valdes, E. P. Abrahamsen, R. P. Rippeth, J. H. Simpson, S. Bacon, S. W. Laxon, I. Polyakov, V. Ivanov and S. Kirillov, 2008. Vertical mixing at intermediate depths in the Arctic boundary current, *Geophysical Research Letters*, **36**(L05601).

Leppaeranta, M., 2005. The drift of sea ice, Springer, Praxis Publishing, Ltd, Chichester, UK.

Lillesand, T., R. Kiefer and J Chipman, 2004. Remote Sensing and image interpretation, John Wiley and Sons, New York.

Long, D. G. and B. R. Hicks, 2005. Standard BYU QuikSCAT/SeaWinds Land/Ice Image Products, *Technical Report MERS 05-04*, Microwave Earth Remote Sensing Laboratory, MERS.

Majewski, D., D. Liermann, P. Prohl, B. Ritter, M. Buchhold, T. Hanisch, G. Paul, W. Wergen and J. Baumgardner, 2002. The Operational Global Icosahedral Hexagonal Gridpoint Model GME: Description and High-Resolution Tests, *Monthly Weather Review*, **130**, 319–338.

Markus, T. and B. A. Burns, 1995. A method to estimate subpixel-scale coastal polynyas with satellite passive microwave data, *Journal of Geophysical Research*, **100**(C3), 4473–4488.

Martin, S., 2001. Encyclopedia of Ocean Sciences: Polynyas, Elsevier Science Ltd., New York, US.

Martin, S. and D. J. Cavalieri, 1989. Contribution of the Siberian shelf polynyas to the Arctic Ocean intermediate and deep water, *Journal of Geophysical Research*, **94**, 12725–12738.

Martin, S., R. Drucker and R. Kwok, 2007. The areas and ice production oft the western and central Ross Sea polynyas, 1992-2002, and their relation to the B-15 and C-19 iceberg events of 2000 and 2002, *Journal of Marine Systems*, **68**, 201–214.

Martin, S., R. Drucker, R. Kwok and B. Holt, 2004. Estimation of the thin ice thickness and heat flux for the Chukchi Sea Alaskan coast polynya from Special Sensor Microwave/Imager data, *Journal of Geophysical Research*, **109**(C10012).

Martin, S., R Drucker, R.and Kwok and B. Holt, 2005. Improvements in the estimates of ice thickness and production in the Chukchi Sea polynyas derived from AMSR-E, *Geophysical Research Letters*, **32**(L05505).

Martin, S. and P. Kauffman, 1981. A field and laboratory study of wave dumping by grease ice, *Journal of Glaciology*, **27**, 283–313.

Massom, R. A., P. T. Harris, K. J. Michael and M. J. Potter, 1998. The distribution and formative processes of latent-heat polynyas in East Antarctica, *Annals of Glaciology*, **27**, 420–426.

Maykut, G. A., 1986. The surface heat and mass balance, The geophysics of sea ice, Martinus Nijhoff Publ., Dordrecht.

McBean, G., G. Alekseev, D. Chen, E. Forland, J. Fyfe, P. Y. Groisman, R. King, H. Melling, R. Vose and P.H. Whitfield, 2005. Arctic climate: past and present. Arctic climate impact assessment, *Scientific report*, Cambridge University Press.

Meier, W. N., J. Stroeve and F. Fetterer, 2007. Whither Arctic sea ice? A clear signal of decline regionally, seasonally and extending beyond the satellite record, *Annals of Glaciology*, **46**.

Melling, H. and E. L. Lewis, 1982. Shelf drainage Beaufort Sea and their effect on the Arctic Ocean pycnocline, *Deep Sea Research*, **29**, 967–986.

Melling, H. and R.M. Moore, 1995. waters during freezing on the Beaufort Sea shelf: evidence from oxygen isotopes and dissolved nutrients, *Continental Shelf Research*, **15**(1), 89–113.

Melling, H., D. R. Topham and D. A. Riedel, 1993. Topography of the upper and lower surfaces of 10 hectares of deformed sea ice, *Cold Region Science and Technology*, **21**, 349–369.

Mikhail, E., J. Bethel and J. Mcglone, 2001. Introduction to modern photogrammetry, John Wiley & Sons, New York.

Morales Maqueda, M. A., A. J. Willmot and N. R. T. Biggs, 2004. Polynya dynamics: A review of observation and modeling, *Review of Geophysics*, **42**(RG1004).

Morales Maqueda, M. A. and A. J. Willmott, 2000. A two-dimensional time-dependend model of a wind-driven coastal polynya: Application to the St. Lawrence island polynya, *Journal of Physical Oceanography*, **30**(6), 1281–1304.

Naoki, K., J. Ukita, F. Nishio, M. Nakayama, J. C. Comiso and A. Gasiewski, 2008. Thin sea ice thickness as inferred from passive microwave and in situ observations, *Journal of Geophysical Research*, **113**(C02S16).

Ou, H. W., 1988. A time-dependent model of a coastal polynya, *Journal of Physical Oceanography*, **18**, 584–590.

Paine, D. P. and J. D. Kiser, 2003. Aerial Photography and Image Interpretation, Wiley-Blackwell, New York, US.

Pease, C. H., 1987. The size of wind-driven coastal polynyas, *Journal of Geophysical Research*, **92**(C7), 7049–7059.

Perovich, D. K. and S. Gerland, 2009. Developing and Implementing Protocols for Arctic Sea Ice Observations, *EOS*, **90**(19), 169–170.

Peterson, B. J., J. W. McClelland, R. Curry, R. M. Holmes, J. E. Walsh and K. Aagaard, 2006. Trajectory shifts in the Arctic and Subarctic freshwater cycle, *Science*, **313**, 1061–1066.

Petrich, C. and H. Eicken, 2010. Sea Ice: Growth, Structure and Properties of Sea Ice, Wiley-Blackwell, Oxford, UK, 2 ed.

Petrie, G., 2006. IGI's Airborne Systems - An Expanded Product Range!, *GeoInformativs*, **9**(7), 36–41.

Petrie, G. and A. S. Walker, 2007. Airborne Digital Imaging Technology: A New Overview, *The Photogrammetric Record*, **22**(119), 203–225.

Pfaffling, A., C. Haas and J. E. Reid, 2007. A direct helicopter EM sea ice thickness inversion, assessed with synthetic and field data, *Geophysics*, **72**, F127–F137.

Proshutinsky, A. Y. and M. A. Johnson, 1997. Two circulation regimes of the wind-driven Arctic Ocean, *Journal of Geophysical Research*, **102**(C6), 12493–12514.

Reimnitz, E., D. Dethleff and D. Nuernberg, 1994. Contrasts in Arctic shelf sea-ice regimes and some implications: Beaufort Sea and Laptev Sea, *Marine Geology*, **28**, 179–210.

Reimnitz, E., D. Dethleff and D. Nuernberg, 1995. Multiyear fast ice along the Taymyr Peninsula, Siberia, *Arctic*, **48**(4), 359–377.

Renfrew, I. A., J. C. King and T. Markus, 2002. Coastal polynyas in the southern Weddel Sea: Variability in the surface energy budget, *Journal of Geophysical Research*, **107**(C6), 1610–1622.

Riggs, G. A., D. H. Hall and V. V. Salomonson, 2003. MODIS Sea Ice Products User Guide, *Tech. rep.*, NASA/Goddard, 758 Space Flight Center; Hydrological Sciences Branch, http://www.modis-snow-ice.gsfc.nasa.gov/sugkc.html.

Rigor, I. G. and R. L. Colony, 1997. Sea-ice production and transport of pollutants in the Laptev Sea, 1997-1993, *Science of the Total Environment*, **202**, 89–110.

Rigor, I. G. and J. M. Wallace, 2004. Variations on the age of Arctic sa-ice ad summer sea-ice extent, *Geophysical Research Letters*, **31**(9).

Rippeth, T. P., 2008. Mixing in seasonally stratified shelf seas: a shifting paradigm, *Philosophical Transactions of the Royal Society*, **363**, 2837–2854.

Romanov, I. P., 1996. Atlas of Ice and Snow of the Arctic Basin and the Siberian Shelf Seas, Backbone Publishing Company, Fair Lawn, US.

Rozman, P., J. Hölemann, T. Krumpen, R. Gerdes, C. Köberle, T. Lavergne and S. Adams, 2010, submitted. Sea Ice Drift in tge Laptev Sea - Observations and Modeling Results, *Polar Research*.

Ryvlin, A. I., 1974. Method of forecasting flexural strength of an ice cover, *Problems of the Arctic and Antarctic (in Russian)*, **45**, 79–86.

Schauer, U., 1995. The release of brine-enriched shelf water from Storfjord into the Norwegian Sea, *Journal of Geophysical Research*, **100**, 16015–16028.

Schauer, U., R. D. Muench, B. Rudels and L. Timokhov, 1997. Impact of eastern Arctic shelf waters on the Nansen Basin intermediate layers, *Journal of Geophysical Research*, **102**(C2), 3371–3382.

Schlosser, P., D. Bauch, R. Fairbanks and G. Bönisch, 1994. Arctic riverrunoff: Mean residence time on the shelves and in the halocline, *Deep Sea Research*, **41**(7), 1053–1068.

Schroeder, D., G. Heinemann and S. Willmes, 2010. Implementation of a thermodynamic sea ice module in the NWP model COSMO and its impact on simulations for the Laptev Sea area in the Siberian Arctic, *Polar Research*, **in press**.

Scott, J., 2008. Sea Ice Decline Intensifies, *Report on sea ice state*, National Snow and Ice Data Center.

Serreze, M. C., M. M. Holland and J. Stroeve, 2007. Perspectives on the Arctic's shrinking sea-ice cover, *Science*, **315**, 1533–1536.

Serreze, M. C., J. A. Maslanik, J. A. Scambos, F. Fetterer, J. Stroeve, K. Knowles, C. Fowler, S. Drobot, R. G. Barry and T. M. Haran, 2009. A record minimum arctic sea ice extent and area in 2002, *Geophysical Research Letters*, **30**(3).

Sharma, P., 2003. Effect of meteorological condition on polynya formation and processes, (PhD thesis, University of Bremen.

Sherwood, C. R., 2000. Numerical model of frazil ice and suspended sediment concentrations and formation of sediment laden ice in the Kara Sea, *Journal of Geophysical Research*, **105**, 9411–9422.

Simmonds, I., C. Burke and K. Keay, 2008. Arctic climate change as manifest in cyclone behavior, *Journal of Climate*, **21**.

Simmonds, I. and K. Keay, 2009. Extraordinary September Arctic sea ice reductions and their relationships with storm behavior over 1979-2008, *Geophysical Research Letters*, **36**.

Skogseth, R., I. Fer and P. M. Haugan, 2005. Dense-Water Production and Overflow From an Arctic Coastal Polynya in Storfjorden, in The Nordic Seas: An Integrated Perspective, *Geophys. Monogr. Ser.*, **158**.

Skogseth, R., P. M. Haugan and J. Haarpaintner, 2004. Ice and brine production in Storfjorden from four winters of satellite and in situ observations and modeling, *Journal of Geophysical Research*, **109**(C7), 14001–14013.

Smedsrud, L. H., 2004. Formation of turbid ice during autumn freeze-up in the Kara Sea, *Polar Research*, **22**, 267–286.

Smith, S. D., R. D. Muench and C. H. Pease, 1990. Polynyas and leads: an overview of physical processes and environment, *Journal of Geophysical Research*, **95**(C6), 9461–9479.

Smith, W. H. F. and D. T. Sandwell, 1997. Global seafloor topography from satellite altimetry and ship depth soundings, *Science*, **277**, 1957–1962.

Spreen, G., L. Kaleschke and G. Heygster, 2008. Sea Ice Remote Sensing Using AMSR-E 89 GHz Channels, *Journal of Geophysical Research*, **113**(C02S03).

Steer, A, A. Worby and P. Heil, 2008. Observed changes in sea-ice floe size distribution during early summer in the western Weddell Sea, *Deep Sea Research*, **55**, 933–942.

Stroeve, J., A. Frei, J. McCreight and D. Ghatak, 2008. Arctic sea-ice variability revisited, *Annals of Glaciology*, **48**(1), 71–81.

Stroeve, J., M. M. Holland, W. Meier, T. Scambos and M. Serreze, 2007. Arctic sea ice decline: Faster than forecast. Geophysical Research Letters, *Geophysical Research Letters*, **34**(L09501).

Stroeve, J. C., M. C. Serreze, F. Fetterer, T. Arbetter, W. Meier, J. Maslanik and K. Knowles, 2005. Tracking the Arctic's shrinking ice cover: Another extreme September minimum in 2004, *Geophysical Research Letters*, **32**(4).

System Laptev Sea, 2008. Eurasische Schelfmeere im Umbruch - Ozeanische Fronten und Polynjasysteme in der Laptev-See, *Progress Report 03G0639*, IFM-GEOMAR, Kiel, Germany.

Tamura, T., K. I. Ohshima, T. Markus, D. J. Cavalieri, S. Nihashi and N. Hirasawa, 2007. Estimation of thin ice thickness and detection of fast ice from SSM/I data in the Antarctic Ocean, *Journal of Atmospheric and Oceanic Technology*, **24**(10), 1757–1772.

Tamura, T., K. I. Ohshima and S. Nihashi, 2008. Mapping of sea ice production for Antarctic coastal polynyas, *Geophysical Research Letters*, **35**(L07606).

Timmermann, R., S. Danilova, J. Schroeter, C. Boening, D. Sidorenkoa and K. Rollenhagen, 2009. Ocean circulation and sea ice distribution in a finite element global sea ice-ocean model, *Ocean Modelling*, **27**(3-4), 114–129.

Timokhov, L. A., 1994. Regional characteristics of the Laptev and the East Siberian seas: climate, topography, ice phases, thermohaline regime, circulation, *Berichte zur Polarforschung*, **114**.

Tucker, W. B. and J. W. Govon, 1981. Morphological investigations of first-year sea ice pressure ridge sails, *Cold Region Science and Technology*, **5**, 1–12.

Vinje, T., 1987. Morphology and dynamics of the Barents Sea ice field, *Poac 77*, University of Alaska, Fairbanks, US.

Vinje, T., 2001. Anomalies and trends of sea-ice extent and atmospheric circulation in the Nordic Seas during the period 1864-1998, *Journal of Climate*, **14**, 255–267.

Wadhams, P., 2000. Ice in the ocean, Gordon and Breach Science Publishers, London, UK.

Weissling, B., S. Ackley, P. Wagner and H. Xie, 2009. EISCAM - Digital image acquisition and processing for sea ice parameters from ships, *Cold Region Science and Technology*, **57**(1), 49–60.

Willmes, S., S. Adams, D. Schroeder and G. Heinemann, 2010a. Spatiotemporal variability of polynya dynamics and ice production in the Laptev Sea between the winters of 1979/80 and 2007/08, *Polar Research*, **in press**.

Willmes, S., T. Krumpen, S. Adams, L. Rabenstein, C. Haas, J. Hoelemann, S. Hendricks and Heinemann G., 2010b. Cross-Validation of polynya monitoring methods from multi-sensor satellite and airborne data: A case study from the Laptev Sea, *Canadian Journal of Remote Sensing*, **36**.

Willmott, A. J., D. M. Holland and M. A. Morales Maqueda, 2007. Polynya Modeling, Smith, W. and D. Barber, eds., Polynyas: Windows to the World, Elsevier, New York, US.

Willmott, A. J., M. A. Morales Maqueda and M. S. Darby, 1997. A Model for the Influence of Wind and Oceanic Currents on the Size of a Steady-State Latent Heat Coastal Polynya, *Journal of Physical Oceanograhpy*, **27**(10), 2256–2275.

Winsor, P. and G. Bjoerk, 2000. Polynya activity in the Artic Ocean from 1958 to 1997, *Journal of Geophysical Research*, **105**(C4), 8789–8803.

Worby, A. P., M. O. Jeffries, W. F. Weeks, K. Morris and R. Jana, 1996. The thickness distribution of sea ice and snow cover during late winter in the Bellingshausen and Amundsen Seas, Antarctica, *Journal of Geophysical Research*, **101**(C12), 28441–28455.

Yen, Y. C., K. C. Cheng and S. Fukusako, 1991. Review of intrinsic thermodynamic properties of snow, ice, sea ice and frost, *3dr International Symposium on Cold Regions Hear Transfer*, **University of Alaska, Fairbanks**, 187–218.

Yu, Y. and R.W. Lindsay, 2003. Comparison of thin ice thickness distributions derived from RADARSAT Geophysical Processor System and advanced very high resolution radiometer data sets, *Journal of Geophysical Research*, **108**(C12), 1701–1711.

Zakharov, V. F., 1966. The role of flaw leads off the edge of fast ice in the hydrological and ice regime of the Laptev Sea, *Oceanology*, **6**, 815–821.

Zakharov, V. F., 1976. Cooling of the arctic and ice cover of the Arctic seas, *Trudy Trans.*, **337**, 96.

Zakharov, V. F., 1997. Sea ice in the climate system. Arctic Climate System Study, *Wmo/td-no. 782*, World Meteorological Organization, World Climate Research Programme, Geneva, Switzerland.

Zhang, X., J. Walsh, U. Bhatt and M. Ikeda, 2004. Climatology and Interannual Variability of Arctic Cyclone Activity: 1948-2002, *Journal of Climate*, **17**, 2300–2317.

Zhang, X. and J. E. Walsh, 2006. Towards a seasonally ice-covered Arctic Ocea: Scenarios from the IPCC AR4 simulations, *Journal of Climate*, **19**, 1730–1747.

Zhao, Y. and A. K. Liu, 2007. Arctic Sea-Ice Motion and Its Relation to Pressure Field, *Journal of Oceanography*, **63**, 505–515.

8

Other co-authorships

Busche, T., Hajnsek, I., Krumpen, T., Rabenstein, L. Hölemann, J. A., Haas, C. and Willmes, S., 2009, Investigating Coastal Polynya Thin Sea Ice State in the Laptev Sea Using TerraSAR-X Dual-Pol Stripmap Data, *IGARSS 2009 Conference Proceedings*, Italy.

Dmitrenko, I. A., Kirillov, S. A., Krumpen, T., Makhotin, M., Abrahamsen, E. P., Willmes, S., Bloshkina, E., Hölemann, J. A., Kassens, H. and Wegner, C., 2010. Wind-driven diversion of summer river runoff preconditions the Laptev Sea coastal polynya hydrography: Evidence from summer-to-winter hydrographic records of 2007-2009, *Continental Shelf Research*, in press.

Dmitrenko, I. A., Wegner, C., Kassens, H., Kirillov, S. A., Krumpen, T., Heinemann, G., Helbig, A., Schröder, D., Hölemann, J. A., Klagge, T., Tyshko, K. P. and Busche, T., 2010, Observations of supercooling and frazil ice formation in the Laptev Sea coastal polynya, *Journal of Geophysical Research*, **115**(C05015).

Dmitrenko, I. A., Kirillov, S. A., Tremblay, L. B., Bauch, D., Hölemann, J. A., Krumpen, T., Kassens, H., Wegner, C. Heinemann, G. and D. Schröder, 2010. The Arctic Ocean Atlantic water layer impacts the Siberian shelf hydrography, *Journal of Geophysical Research*, in press.

Rozman, P., Hölemann, J. A., Krumpen, T., Gerdes, R., Köberle, C., Lavergne, T. and Adams, S., 2010, Validating Satellite Derived and Modeled Sea Ice Drift in the Laptev Sea with In-Situ Measurements of Winter 2007/8, submitted to *Polar Research*.

9

Acknowledgments

I wish to express my sincere gratitude to my supervisor Prof. Rüdiger Gerdes, head of the sea ice physics department, who accepted my PhD proposal at the Jacobs University and agreed to be the first referee of this thesis. I am grateful for his support throughout the work, kind supervision and scientific freedom.

This thesis was initiated by its promoter Jens Hölemann. He is a project leader in the Russian-German Research Cooperation 'System Laptev Sea' and introduced me into this fascinating topic. I thank for welcoming me and making me part of the 'System Laptev Sea' project. Without his negotiations and efforts, the EM measurements made for the first time on Russian territory would not have been possible.

Prof. Christian Haas is very much acknowledged for his enthusiastic support and numerous helpful and productive hints. He left the AWI for a professorship at the University of Alberta in Canada and was constantly supporting me from abroad. It was him, who convinced me to give up my job in Switzerland and to start my PhD at the AWI; a decision I never regretted!

Furthermore, I am grateful to Prof. Laurenz Thomson who accepted to be the second referee of my thesis.

Special thanks to my friends and colleagues Stefan Hendricks, Lasse Rabenstein and Polona Rozman for their moral and scientific support and excellent work atmosphere. Lasse, Stefan and me temporarily managed the sea-ice physics division from 2007 to 2008. Furthermore, I am grateful to Sascha Willmes from the University of Trier and Thomas Busche from the German Aerospace Center. Both substantially contributed through discussion and comments to the presented results.

Thanks to all my former and present colleagues. In particular I would like to thank Joao Mar-

cello Absy, Marcel Nicolaus, Wolfgang Dierking, Hartmut Hellmer, Dirk Kalmbach, Andreas Herber, Lilien Schubert, Marc Taylor, Bettina Schmitt, Malte Thoma, Sandra Schwegemann, and many others for encouraging me and making me comfortable at the AWI.

Torben Klagge, Igor Dmitrenko, Heidi Kassens, Sergey Kirillov, David Schröder, Susanne Adams, Carolin Wegner and many other colleagues from the 'System Laptev Sea' project are acknowledged for scientific and logistic support, helping hands during expeditions, and an excellent time in field.

This thesis was funded by the Federal Ministry for Education and Research and the AWI.

Finally, I want to express my deepest gratitude to my family and friends for their moral and loving support.

10

Statement of source

Declaration

I declare that this thesis is my own work and has not been submitted in any form for another degree or diploma at any university or other institution of tertiary education. Information derived from published or unpublished work of others has been acknowledged in the text.

Date and Signature